

The Telychian (early Silurian) oxygenation event in northern Europe: A geochemical and magnetic perspective

Mark W. Hounslow¹, Kenneth T. Ratcliffe², Samuel E. Harris³, Jerzy Nawrocki⁴, Krystian Wójcik⁵, Paul Montgomery⁶, Nigel H. Woodcock⁷

1. Lancaster Environment Centre, Lancaster University, Lancaster, UK. LA1 4YW and Earth, Ocean and Ecological Sciences, Univ. of Liverpool, Jane Herdman Building, Liverpool, L69 3GP (mark.w.hounslow@gmail.com, *correspondent*)
2. Chemostrat Ltd, Buttington, Welshpool, UK (kenratcliffe@chemostrat.com).
3. School of Archaeological and Forensic Sciences, University of Bradford, Bradford, BD7 1DP, UK (samh128@hotmail.com).
4. Faculty of Earth Sciences and Spatial Management, Maria Curie-Skłodowska University in Lublin, Al. Kraśnicka 2cf, 20-718 Lublin, Poland (jnaw@pgi.gov.pl)
5. Państwowy Instytut Geologiczny - Państwowy Instytut Badawczy ul. Rakowiecka 4, 00-975 Warszawa, Poland (kwoj@pgi.gov.pl)
6. Chevron upstream, Aberdeen, UK (pmontgomery@chevron.com).
7. Department of Earth Sciences, University of Cambridge, Cambridge, CB2 3EQ, UK (nhw1@cam.ac.uk).

Abstract

Widespread marine red beds in the European Telychian (lower-Silurian) are one expression of an interval of unusually widespread oxic conditions in low palaeolatitude Silurian seas. This work examines in detail the geochemical and magnetic susceptibility record of cores from southern Poland, which also express the Telychian oxygenation event in grey-mudstones. The geochemical data provide an evaluation of redox conditions, palaeoweathering, sediment provenance, primary palaeoproductivity and upwelling. Sediment provenance is evaluated against possible sources on the East European Craton. The data suggest that the magnetic susceptibility is carried by both paramagnetic Fe-silicates and Fe-oxides. Magnetic data are supplemented by magnetic hysteresis and isothermal remanent magnetisations, and mineralogical data on selected samples. In Poland the oxygenation event is clearly expressed in larger Fe₂O₃ and magnetic susceptibility, caused by enhanced palaeoweathering, changes in sediment provenance and a redox influence on the preservation of Fe-oxides. A much briefer oxygenation event is detected in the upper Rhuddanian. Palaeoproductivity fluxes indicate that the Telychian oxygenation event was caused by a reduction in primary oceanic palaeoproductivity, possibly linked to a reduction in nutrient delivery to the margin of East European Craton, inferred to be caused by increased aridity. The increased aridity stimulated enhanced delivery of Fe-enriched aeolian dust from soils, generating a magnetic susceptibility and Fe₂O₃ expression of the Telychian oxygenation event.

Keywords: marine red beds, redox, palaeoproductivity, palaeoweathering, magnetic susceptibility, provenance, East European Craton.

1. Introduction

In Europe a distinctive feature of the upper Llandovery (Telychian) are intervals of marine red and purple mudstones (Rickards 1973; Ziegler and McKerrow 1975; Kiipli et al. 2000a). Similarly aged red mudstones are also developed in the Telychian of South China (and the Tarim and Qilian basins) and eastern North America (Rong et al. 2012; 2019; Liu et al. 2016; Sullivan and Brett 2013). Typically, in China the red mudstones are interbedded with a variety of other non-red mudstone, shales and sometimes sandstones, rather than continuous red mudstones. In Europe, the Llandovery marine red beds are distributed on all the three major plate margins, although they are absent from the Polish terranes and their adjacent East European Craton (EEC) margin (Fig. 1; Table 1). The European marine red beds are typically associated with outer or deep shelf environments and sometimes deep oceanic environments (Rust 1965; Ziegler and McKerrow 1975; Benton and Gray 1981; Bassett et al. 2002). In places where their relative depth relationship with more proximal sediments can be clearly defined (such as in the Baltic Basin), they are transitional to non-red mudstones in both shallower and deeper water settings (Kiipli et al. 2004; 2012). In the Welsh borders the Purple Shales Formation- a unit of red to purple mudstones- is also a deeper water shelf deposit, with shallowing conditions eastwards, although no coastline deposits are known (Benton and Gray 1981; Bassett et al. 1992).

In contrast, Telychian red mudstones and siltstones (and interbedded fine-grained sandstones) in South China, have been interpreted as shallow marine to coastal (sabkha?) deposits due to the presence of rare fishes, brachiopods, ostracods, trilobites and corals (with conodonts and graptolites in adjacent strata) and the presence of mudcracks, waves ripples and rare cross-bedded sandstones (Rong et al. 2012; Zhang et al. 2014b). However, the review of the Yangtze Platform red beds by Zhang et al. (2018) indicated that these red beds are instead restricted to deeper-water units in the middle Telychian, like in Europe.

Ziegler and McKerrow (1975) interpreted the Telychian marine red mudstones as connected with increased terrestrial sediment flux, associated with reworking of coastal systems during transgressive intervals and higher sea-levels. In contrast, Loydell (1998) suggested that the red beds were most common during intervals of Telychian regression, preferentially delivering terrestrial 'red bed' material. Both of these hypotheses implicate enhanced delivery of terrestrial sources as source of the reddening. Exactly how the 'terrestrial' material may be recognised beyond being red, is not elaborated, but plausible scenarios could involve changes in sediment provenance, delivery of more weathered material (e.g. from oxic soils), or changes in the mechanisms of delivery (relatively more or less riverine input). These models may be applicable to some parts of the South China Telychian successions, where inshore to offshore changes seem regionally well-defined, implying a connected system of terrestrial delivery (Rong et al. 2012; 2019; Zhang et al. 2018). The coastal-terrestrial-delivery hypothesis seems less applicable to European Telychian successions, since transitional offshore to onshore successions are not well defined, other than in the Baltic Basin. In addition, land areas on East Avalonia with major terrestrial clastic inputs appear restricted to the south-west, sourced from Pretannia during the Telychian (Bassett et al. 1992; Hillier 2002). The low palaeolatitude locations of these land

areas during the Llandovery, indicates that aeolian dust may have been a potential alternative pathway for terrestrial sediment delivery.

The alternative hypothesis of Kiipli et al. (2009) interpreted the Baltic Basin red beds as a result of increased current vigour and water-mass ventilation on the continental shelves, allowing greater oxygenation of bottom waters. A third hypothesis has been suggested in which greater oxygen content of marine waters is connected with productivity decline (Zhang et al. 2018), as the key factor controlling the Yangtze Platform marine red beds. This is similar to one of the key conditions suggested by Hu et al. (2012) for the formation of marine red beds namely, low productivity (low organic matter burial), oxic and nutrient poor environments.

Data are sparse to assess critically which of these hypotheses may be applicable to the European Telychian red beds. However, the similar age range of the upper Llandovery red beds both in Europe and China hints at some common causal connection, so we loosely refer to this as the ‘Telychian oxygenation event’, as having some parallels with the ‘Hirnantian oxygenation event’ (Zhou et al. 2012; Pohl et al. 2017), associated with the increased oxygenation of marine systems during the Hirnantian glaciation. This is not to infer that the Telychian oxygenation event is associated with cooling, since a number of factors could contribute to formation of marine red beds (Hu et al. 2012; Bábek et al. 2018).

Our goals are firstly, to demonstrate that the Telychian oxygenation event is also expressed in non-red mudstones, in cores from the Polish margin; secondly, to evaluate the nature of sediment provenance changes and source weathering as clues to changes in the characteristics of terrestrial sediment delivery; thirdly, to evaluate the hypotheses that productivity decline and water-mass ventilation may be driving the oxygenation event; fourthly, to evaluate the regional timing of red-bed formation and explore if there is a relationship to eustatic highstands.

We analyse data from the Zwierzyniec-1, Grabowiec-6 and Tłuszcz IG-1 cores (Fig. 1), involving several datasets: Firstly, magnetic susceptibility (MS) in sediments is fundamentally related to the quantity and types of Fe-bearing mineral-magnetic phases, which can be sensitive to both redox conditions (Riquier et al. 2010) and sediment provenance (Hounslow and Morton 2004; Liu et al. 2010). We unravel the mineralogical and environmental controls on the MS signal using additional magnetic and geochemical datasets in the cores (Sections 4 and 8). Secondly, we use a geochemical dataset to critically examine the redox state in the Zwierzyniec-1 core, which has a near-complete recovery of the Telychian (Section 5). Thirdly, we evaluate the weathering and provenance characteristics of the supplied sediment at the Zwierzyniec-1 site (Sections 6 and 7). Lastly, we provide palaeoproductivity flux estimates and upwelling indices for the Hirnantian to lower Homerian interval in Zwierzyniec-1 (Section 9). These together provide a better collective assessment of some of the proposed key controls on the Telychian oxygenation event in Europe, discussed in Section 10.

2. Background

2.1 Magnetic susceptibility (MS) of Silurian sediments

Magnetic susceptibility changes have been shown to reflect gross sequence stratigraphic and cyclostratigraphic changes in the Palaeozoic, with most work focussing on carbonate-rich successions (Da Silva et al. 2013, 2015). Typically in Palaeozoic successions, strong controls on changes in MS are lithogenic inputs and particle sorting/size.

Magnetic susceptibility is commonly negatively correlated to calcite or dolomite content (Ellwood et al. 2000; Da Silva et al. 2009; Śliwiński et al. 2012; Zenkner and Kozłowski 2017), like in modern deep-sea settings, due to the dilution effect of diamagnetic calcium-carbonate on the MS signal (Hounslow and Maher 1999; Larrasoña et al. 2008). This is because the total volume susceptibility of sediment, $K_{\text{tot}} = K_{\text{dia}} + K_{\text{para}} + K_{\text{ferro}}$, where the subscripts dia, para and ferro indicate the volumetric-based contribution from diamagnetic minerals (e.g. calcite, quartz etc.), paramagnetic minerals (e.g. Fe- and Mn bearing silicates and carbonates), and ferromagnetic minerals (e.g. magnetite). Consequently if contents of calcite or quartz change through successions, K_{tot} can strongly reflect the ‘diamagnetic dilution’ of the paramagnetic or ferromagnetic signal derived from the lithogenic component (Rochette 1987).

In the non-carbonate fraction of sediments, the MS signal often resides in the silt and clay-sized fractions, with larger K_{para} or K_{ferro} for these fractions (Da Silva et al. 2009; Koptíková et al. 2010). Consequently, in clastic-dominated successions the MS signal can also be related to gamma activity (Løvlie and Van Veen 1995; Kozłowski, and Sobień 2012).

Telychian MS data from carbonate-ironstone-clastic successions in eastern North American indicate that highs in MS are related to sediment-starved horizons in shallow, oxic environments, due to higher concentrations of iron-bearing silicates, Fe-carbonates, goethite and haematite (Sullivan and Brett 2013). These sediment-starved horizons are associated with transgression, but when traced into deeper water these horizons are magnetically indistinguishable from the surrounding shaley units, indicating some mineralogical and redox-control on the minerals carrying the MS. The extent to which this MS behaviour and the co-occurrence with peaks in oxic-sedimentary units are specific to the Llandovery is not clear. In contrast, the MS study of English (1999) from northern England was focused on graptolitic bearing deeper water mudstones (Aeronian-Telychian in age), demonstrating that MS variations were linked to chlorite content. The MS was not dependent on the redox-state, which varied between more dysaerobic graptolitic laminated mudstones and aerobic grey mudstones, but instead showed a stratigraphic variation related to sediment age.

To unravel the sedimentological controls on the MS signal, typically requires a range of associated mineralogical and geochemical data, an approach which is used here, and applied to investigate the Telychian oxygenation event, which is also expressed in MS.

2.2 Geology and stratigraphy

The data from the Polish cores are from the more basinal part of the Silurian facies belts in Poland, which can be traced from the Peri-Baltic Depression in the North into the Podolia region of the Ukraine (Teller 1997). Tłuszcz IG-1 well (N52°30'09.82" E

21°40'06.49", 99 m elevation) is from the more basinal parts of the Podlasie Depression (Fig. 1), a southern sedimentological continuation of the Peri-Baltic depression, but is now separated from it by the Mazurska High, formed in the Varican Orogeny (Jarochowska and Munnecke 2015; Podhalańska 2019). The Grabowiec-6 (N 50°57'5.19", E 23°25'56.80; 209 m elevation) and Zwierzyniec-1 (N 50°44'14.01", E 23°07' 24.57" 230 m elevation) cores are from the Lublin Slope, and Biłgoraj-Narol Zone respectively (adjacent to the Teisseyre-Tornquist Zone (TTZ); Poprawa 2019), more distal parts of the same facies belts seen to the north and east (Fig. 1).

The Tłuszcz IG-1 core consists of 25 m of Llandovery overlain by 129 m of Wenlock, well dated by graptolites (Fig. 2d), in predominantly mudstones with thin calcareous mudstone beds (Aren 1967 1972; Dadlez et al. 1974; Lis and Bohacs 2012; Podhalańska 2019). The Zwierzyniec-1 and Grabowiec-6 wells contain core from 35 m and 7 m of the Llandovery respectively (Fig. 2b,c), with overlying 12 m and 60 m of the Wenlock respectively (Sullivan et al. 2018). The lowermost Silurian in Grabowiec-6 is upper Telychian (a regional hiatus feature in the Lublin Basin due to eastwards onlap; Porêbski et al. 2013; Podhalańska 2019; Fig. 2c), whereas the earliest Rhuddanian is present in wells Tłuszcz IG-1 and Zwierzyniec-1 (Podhalańska 2019; Sullivan et al. 2018). In Grabowiec-6 the upper Llandovery strata rest disconformably on Hirnantian carbonates (Sullivan et al. 2018; Hounslow et al. 2021a). In the Zwierzyniec-1 core, the Aeronian is either condensed or reduced in thickness due to a fault (Fig. 2b). Grabowiec-6 and Zwierzyniec-1 cores have a chronology based on graptolites and organic carbon isotope stratigraphy, whereas Tłuszcz IG-1 has a detailed graptolite biostratigraphy (Dadlez et al. 1974), details of which are listed in the Supplementary information (SI). The Lublin Basin and slope have a similar Silurian stratigraphy and development to the Łysogóry region of the Holy Cross Mountains (Kozłowski 2008; Kozłowski and Munnecke 2010).

The Silurian in all three cores is dominated by mudstones with cm-scale calcareous mudstone beds, with more organic-rich laminated mudstones in the Rhuddanian (Sullivan et al. 2018). The Llandovery and Wenlock of the Tłuszcz IG-1 and Grabowiec-6 cores consists of grey mudstones and calcareous mudstones, with darker coloured, occasionally laminated mudstones dominating in the lower Llandovery in Tłuszcz IG-1 and lower Sheinwoodian in Grabowiec-6. The most common sedimentary structure in the Silurian mudstones on the Polish margin is a weak lamination, along with rare current and wave ripples, graded beds, micro scours, gutter casts and rarer hummocky cross-stratification, indicating weak periodic traction currents and wave activity probably from episodic storms (Lis and Bohacs 2012; Porêbski et al. 2013). Similar subtle mud-hosted structures occur in the Llandovery successions in the northern Holy Cross Mts (Trela et al. 2016). Pyritic clots, early carbonate concretions, carbonate 'whiting' events and rare trace fossils are also present (Porêbski et al. 2013; Zenkner and Kozłowski 2017). The Silurian in Zwierzyniec-1 has lower carbonate contents than both Tłuszcz IG-1 and Grabowiec-6.

3. Methods and materials

3.1 Magnetic measurements

Surface volumetric magnetic susceptibility (K_{surf}) measured at 10 cm spacing, was measured on the three cores (Grabowiec-6, Zwierzyniec-1 and Tłuszcz IG-1), using a Bartington Instruments Ltd, MS3 magnetic susceptibility meter and an MS2K surface probe, correcting for instrumental drift every 1 m of core. K_{surf} for Grabowiec-6, Zwierzyniec-1 was measured on a sectioned flat surface, whereas that for Tłuszcz IG-1 was on 10 cm diameter round-core surface or bedding surfaces.

In the Grabowiec-6, Zwierzyniec-1 and Tłuszcz IG-1 cores anhysteretic remanence (ARM) and backfield isothermal remanent magnetisation (IRM), were measured using the procedures in Walden (1999) on selected intervals in the Hirnantian, Telychian, Sheinwoodian and Gorstian to investigate the ferrimagnetic mineralogy. The IRM and ARM were measured using a Molspin spinner magnetometer. From Grabowiec-6, a sub-sample from the same sample set was investigated for magnetic mineralogy using a Princeton Micromag vibrating sample magnetometer (VSM) with fields up to 0.9 T. The high field susceptibility χ_{dp} (due to diamagnetic and paramagnetic minerals) was isolated by fitting a linear segment to the high field curve (80% of field, on average using >0.71 T part) and magnetic parameters σ_{hys} and $B_{\text{th}}/B_{\text{cr}}$ of the hysteresis curves isolated with RockMagAnalyzer v.1. software (Leonhardt 2006). σ_{hys} and $B_{\text{th}}/B_{\text{cr}}$ can provide estimates of the ferrimagnetic domain state (Fabian 2003; Roberts et al. 2019). The total susceptibility (χ_{tot}) was evaluated from the low field slopes (<30 mT) (Von Dobeneck 1996), from which the ferrimagnetic susceptibility $\chi_{\text{ferri}} = \chi_{\text{tot}} - \chi_{\text{dp}}$. A second proxy for paramagnetic+diamagnetic content ($M_{\text{dp}}/M_{\text{tot}}$) was estimated from the total induced magnetisation (M_{tot}) and that part due to the paramagnetic+diamagnetic slope (M_{dp}) at 0.71 T field.

The diamagnetic contribution to MS is estimated using the calcite content and χ for calcite of $-4.46 \times 10^{-9} \text{ m}^3/\text{kg}$ (Schmidt et al. 2006), from which the paramagnetic susceptibility (χ_{para}) and magnetisation (M_{para}) can be determined from χ_{dp} and M_{dp} in hysteresis measurements. Since MS is often primarily carried by the detrital fraction in mudrocks it is helpful to express MS in carbonate-free terms (Robinson et al. 2000), otherwise MS changes can reflect diamagnetic carbonate content (i.e. diamagnetic dilution), if there are significant variations in carbonate. K_{surf} was expressed as the calcite free MS (K_{scf}) where $K_{\text{scf}} = [(K_{\text{surf}} - (P \times K_{\text{cal}})] / (1.0 - P)$, where P = proportion of calcite (0-1.0), $K_{\text{cal}} = -1.21 \times 10^{-5}$ SI with calcite density = 2710 kg/m^3 (this is a diamagnetic correction and a correction for the calcite content).

3.2 Geochemistry, X-ray diffraction (XRD) and redox

Using the ICP OES-MS data of Sullivan et al. (2018), we investigated in more detail the relationships between the redox geochemistry and magnetic data in Zwierzyniec-1 (Fig. 2b). Fe oxides are particularly sensitive to redox conditions, and under normal marine depositional conditions the stability order to sulphidic diagenesis is ilmenite > haematite > magnetite > Fe-oxyhydroxides, often leading to large losses in Fe-oxide content during burial

(Canfield et al. 1992; Hounslow and Maher 1999; Poulton et al. 2004; Nowacyk 2011; Roberts 2015; Scheidt et al. 2017). Losses may be grain-size selective, and if losses are large may leave residual inclusion-hosted population in silicate grains isolated from the pore space (Hounslow and Morton 2004).

Selected sets of samples from Grabowiec-6 and Zwierzyniec-1 were also subjected to quantitative XRD analysis (using random whole-rock mounts). This determined key mineral components, based on the methods of Chung (1974) and Srodon et al. (2001) and was performed at the Chevron-HGTC, Mineral Analysis Laboratory. These were at corresponding levels to the ICP OES-MS data. We derived a transfer function to determine calcite content, non-carbonate content and quartz content, which was calibrated with the XRD-derived mineralogy data (SI Figs. S3, S4). To map the K_{surf} values to ICP OES-MS sample depths the 10 cm-spaced K_{surf} were linearly interpolated at the ICP OES-MS and XRD sampling points. This allowed us to examine the relationships between chemistry and magnetic properties in the non-carbonate fraction (the ‘calcite or carbonate-free’ fraction; Robinson et al. 2000). Samples at the position of the ICP OES-MS samples were also measured for mass specific susceptibility, χ and expressed as the carbonate free susceptibility, χ_{cf} like K_{scf} .

Enrichment factors are used with normalisation to Al, and the post-Archean average Australian shale (PAAS; McLennan 1989; Rollinson 1993), principally using the redox-related values in Tribovillard et al. (2006). To attach redox thresholds to the stratigraphic intervals, we used the approach of Algeo and Li (2020) by looking for compound co-variation in metal enrichment factors, C_{org}/P and DOP_T (degree of pyritisation using total S and Fe) against MO_{EF} and U_{EF} (see Algeo and Li 2020 for practical details). We use the redox terminology of Tyson and Pearson (1991).

Portable XRF measurements were also performed on limited parts of Grabowiec-6 and Zwierzyniec-1 using the methodology of Nyhuis et al. (2016). This used a Niton XL3t GOLDD+ XRF analyzer at 6 to 50 KV, 200 μA max, Ag anode, obtaining around 30 elements from Mg up to U. Like the ICP OES-MS data the 10 cm-spaced K_{surf} were linearly interpolated to the portable XRF sampling depths to enable exploration of relationships between geochemistry and K_{surf} at a higher stratigraphic-resolution than the ICP OES-MS data.

Principal component analysis (PCA) was used with the χ_{cf} and ICP OES-MS data from Zwierzyniec-1, to explore the likely controls on the MS. To pre-select a set of elemental data for PCA, which *jointly* best express the relationship to χ_{cf} , we used stepwise, forward-backward multiple linear regressions (MLR) using Akaike information criteria (AIC) for variable entry and removal using the *olsrr* package in R (Heinz et al. 2018; Hebbali 2018). The major oxides were log-ratioed to the average oxide content (symbolised as CaO^L , MnO^L etc) to limit the 100%-closure problem (Rollinson 1993). The variable selection using MLR (61 variables in total) also included the molar normalised major element concentrations (symbolised as e.g. K_2O^N etc) which are used in weathering indices (e.g. Ohta and Arai 2007; Table 2). Estimated quartz and calcite+dolomite contents from the XRD to geochemistry

transfer functions (SI Fig. S4) were also used in PCA. PCA used 'princomp' in R (R Core Team 2020).

3.3 Provenance and source weathering evaluation

We assess the weathering of the source material using the chemical index of alteration (CIA) of Nesbitt and Young (1982), the weathering index of Parker (WIP; Price and Velbel 2003) and the silica-titania index (STI) of Jayawardena and Izawa (1994) (Table 2). We use $WIP_R = 100 - WIP$, and $STI_R = 100 - STI$, for convenience, so like CIA, STI_R and WIP_R increase for greater degrees of weathering. CIA reflects the conversion of feldspar to clays by the loss of Ca, Na and K (Table 2), so the proportion of alumina to alkalis increases in weathered products (Nesbitt and Young 1996; Price and Velbel 2003). WIP expresses the proportions of mobile alkali and alkaline earth metals (Table 2), and is most appropriate for studying weathering in heterogeneous rocks, but may not be so appropriate for highly weathered sources (e.g. ferricretes, bauxites etc). The Si-Ti weathering index was developed by Jayawardena and Izawa (1994) as a proxy for the degree of chemical weathering in tropical climates on high grade metamorphic rocks. It primarily monitors changes in the silica to titania ratio, as silica is lost in tropical soils, at weathering intensities beyond that which mobile alkalis are severely depleted.

To evaluate the impact of possible provenance differences on the magnetic and geochemical signals in Zwierzyniec-1, ratios of relatively immobile elements Zr, Nb, Ti, Sc, Ga, Cr, and Th were explored (Floyd and Winchester 1978; Winchester and Floyd 1976 1977; Nesbitt and Markovics 1997). Yttrium and the REE were not used, since these have been shown to be moderately mobile during source weathering and diagenesis (Milodowski and Zalasiewicz 1991; Fralick and Kronberg 1997; Hill et al. 2000; Panahi et al. 2000). A pre-selected set of ratios which likely record provenance information, and are the least noisy (in a stratigraphic sense), were chosen by inspection and using the stratal consistency function of Hounslow and Morton (2004). In an effort to interpret inferred geochemically-based provenance changes in Zwierzyniec-1, we compared the trace element ratios to a bulk-rock database from the basement complexes of the East European Craton (EEC). This database covers Archean to Ediacaran igneous and metamorphic rock data, with divisions into west Sarmatia, east Sarmatia and southern Svecofennian basement (i.e. six sub-sets). This database comprises 836 igneous, 59 meta-igneous and 122 metasediment records and is detailed in the SI.

Division into provenance groups used cluster analysis, principally the fuzzy cluster methods in R and the fclust package, using the FKM.gkb.noise function which performs the Gustafson, Kessel and Babuska algorithm for non-spherical clusters (using standardized datasets) with an additional noise class (Ferraro et al. 2019). We also explored conventional K-means (KMeans function) and hierarchical clustering (hclust function) for comparison in R.

3.4 Palaeoproductivity and age model for Zwierzyniec-1

Palaeoproductivity flux estimates were generated for Zwierzyniec-1 using the conceptual framework proposed by Schoepfer et al. (2015), based around modern marine

systems, using flux estimates of C_{org} and P. Phosphorus concentrations were estimated as excess (P_{XS}), based on an approach removing detrital P (Shen et al. 2015; SI Fig. S16). Trace metal proxies for upwelling and restricted oceanic anoxic settings have also been proposed by Sweere et al. (2016), from which we use the $Mn_{EF} \times CO_{EF}$ proxy. The alternative using Cd is not possible with the data available.

Palaeoproductivity fluxes require an age model and accumulation rates, which were based around the biostratigraphic age tie points in Sullivan et al. (2018), linked to ages of biozone bases from Melchin et al. (2012) and Cooper et al. (2012). This is supplemented by the ages for the Hirnantian isotope excursion (HICE) and early Sheinwoodian carbon isotope excursion (ESCIE) inflexion points from Cramer et al. (2012) and Gorjan et al. (2012) linked to the biostratigraphy. The age model is constructed using the Bayesian-based approach of Haslett and Parnell (2008) and Parnell et al. (2008) as implemented in the Bchron function in R. Accumulation rates (in cm/kyr) were determined from the gradient of the age model using both a simple linear (3 point estimate), and using adaptive localised regression (Loader 1999) as implemented in LOCFIT in R. Final accumulation rates were determined with adaptive regression, since the Bchron age-model simulations generate noise in the age-depth gradient, which is best removed with the LOCFIT adaptive regression. Details of these procedures are in the SI section 5.

4 Magnetic susceptibility changes in the cores

The MS data from the Polish cores displays three distinctive MS signatures (Fig. 2). Firstly, the Rhuddanian shows a broad low in MS values, with values which are not seen again in the cores until the middle Sheinwoodian, in stage slice Sh2 to Sh3 (Fig. 2a,b). This low in MS is similar in magnitude to that seen in the Rhuddanian at the Bardo Stawy section from the Holy Cross Mts (Hounslow et al. 2021b; Fig. 2a). There is some variation in MS in the middle-upper Rhuddanian that may also be reflected in the data from Bardo Stawy, with a weak high in the Rh3 interval in both Bardo Stawy and Zwierzyniec-1.

Secondly, a broad high in MS occurs in the lower-middle Telychian (here termed Phase –I), clearly seen at Zwierzyniec-1 and Tłuszcz IG-1 (the MS data from Tłuszcz IG-1 is more noisy due to poorer core-surface quality). Only the uppermost part of this Phase-I peak is seen at Grabowiec-6, due to the absence of most of the Llandovery (Fig. 2c). The start of the Phase-I rise occurs in the lower part of the Te1 stage slice, and ends in stage slice Te3, and is best dated at Tłuszcz IG-1 (Fig. 2d). At both Zwierzyniec-1 and Tłuszcz IG-1 there is a similar structure in MS variation, that tentatively suggests the Phase-I peak may be composed of three separate sub-peaks in K_{surf} labelled a, b and c (Fig. 2).

Thirdly, above Phase-I is a progressive decline in K_{surf} (referred to as Phase-II) through the main part of the early Sheinwoodian carbon isotope excursion (ESCIE), to a low in K_{surf} in stage slice Sh2 to Sh3, which is shown in all three cores. The end of Phase-II is associated with the initial decline in $\delta^{13}C_{org}$ of the ESCIE (Fig. 2b,c). In Zwierzyniec-1 there is a likely hiatus (at an oxidized mudstone) at 2951.25 m, where the uppermost Telychian (*Cy. insectus*- *Cy. centrifugas* biozones) is probably missing (Sullivan et al. 2018). An equivalent hiatus is not apparent in Grabowiec-6 or Tłuszcz IG-1.

4.1. Unravelling the magnetic mineral contribution to the MS

Within the Sheinwoodian –Homerian interval in Grabowiec-6, the lowest K_{surf} values represent limestone and carbonate-rich beds (marked as L in Fig. 2c), likely due to the carbonate dilution effect. This kind of lithological control is more marked higher in the core (SI Figs. S1, S2). In addition, linking K_{surf} with the XRD determined mineralogy, shows a broad division into a calcite-poor ($< \sim 20\%$ calcite) and calcite-rich group, with the calcite rich-group showing a dilution relationship with diamagnetic calcite (Fig. 3a). This diamagnetic dilution is clearer on the dataset, when using the portable XRF data to determine calcite content (Fig. 3b; see SI for transfer function details). However, the relationship between calcite content and K_{surf} differs between samples with calcite content in excess of $\sim 23\%$ and those with $< 23\%$ calcite (Figs. 3b), indicating a larger MS in the non-carbonate fraction of the calcite-rich group. The calcite-rich-group is better represented by samples younger than the middle Sheinwoodian and also those from the Ordovician, whereas the Rhuddanian to Phase-II intervals are nearly all calcite-poor mudstones.

Niezabitowska et al. (2019a,b) have measured χ_{para} as 3 to 17 times larger than χ_{ferro} in Wenlock mudstones from Pomerania, and Kozłowski and Sobień (2012) have inferred major paramagnetic contributions in Ludfordian mudstones from the Mielnik IG-1 core (90 km ESE from Thuszcz IG-1; Fig. 1). The inferred mineralogical source of this paramagnetic contribution in these mudstones is Fe-rich chlorite, which range up to 13% of the rock volume (Niezabitowska et al. 2019a), although Fe-rich illite may also be magnetically important in clay fractions (Rochette 1987; Potter et al. 2004). The VSM data from the Grabowiec-6 samples indicate that the paramagnetic contribution to susceptibility ($100 \cdot \chi_{\text{para}}/\chi_{\text{tot}}$) ranges from 20% to 97% (χ_{para} 0.25 to 32 larger than χ_{ferro}) over the Phase-I to Phase-II interval (Figs. 4a). The alternative paramagnetic content proxy using induced magnetisation of $M_{\text{para}}/M_{\text{tot}}$ (at 0.71 T) suggests less of a range and moderate paramagnetic contents (inset in Fig. 4a). The larger spread of $\chi_{\text{para}}/\chi_{\text{tot}}$ values may relate to inadequately estimated low field susceptibility, since the initial (untreated state; Von Dobeneck 1996; Leonhardt 2006) part of the hysteresis loop was not measured. Alternatively, the scatter may be due to poorly corrected drift in the high-field part of the hysteresis loops.

When the K_{surf} is expressed on a calcite-free basis, K_{scf} of the calcite-rich group have a weak positive relationship with chlorite content (Fig. 3c), indicating a possible linkage between chlorite content and magnetic mineral abundance (i.e. MS), like found by English (1999). In contrast, K_{scf} in the calcite-poor samples is not related to chlorite content or illite-smectite content (Figs. 3d), and MS is independent from the two-fold division of the Grabowiec-6 mudstones into quartz-poor claystones (70-90% illite-smectite) and mudstones with 30-40% illite smectite (these divisions are related to the cm-scale lamination). This suggests that an increased content of chlorite (or Fe-rich illite) is unlikely to be responsible for the MS peak in Phase-I. However, the sample set from the Phase-I peak in Grabowiec-6 is only within the youngest part of the peak, and it is possible that the limited stratigraphic range of samples may have introduced sampling bias.

Part of the reason for the differences between the calcite-poor and rich lithologies, is that many (but not all) limestones have larger ferrimagnetic mineral abundance (shown by larger SIRM; Fig. 5a). This is similar to the Phase-I and Phase-II samples from Zwierzyniec-I and Thuszcz IG-1 (Fig. 5a). The limestones also have larger MS when expressed on a carbonate-free basis (Figs. 3c,d). In the Grabowiec-6 samples there is no evidence for pyrrhotite or greigite (Hounslow et al. 2021b). This also appears to be the case for Silurian shales in Northern Poland (Niezabitowska et al. 2019b).

Mean IRM acquisition above 0.3 T ($\%IRM_{0.3-1T}$) is similar for the Rhuddanian, Phase-I and Phase-II sample ($5.4 \pm 1.8\%$, $4.2 \pm 2.1\%$, $5.9 \pm 2.7\%$ respectively) indicating magnetic dominance by magnetite, with smaller magnetic contributions from haematite (Hounslow et al. 2021b). Niezabitowska et al. (2019b) suggest a similar ferromagnetic mineralogy in Wenlock Mudstones from N. Poland. Limestones have larger values $-IRM_{0.1T}/SIRM_{1T}$, indicating also more haematite content (Fig. 5b). The magnetite-haematite mixing relationships of Frank and Nowaczyk (2008) with 2 μm and $<5 \mu\text{m}$ magnetite and haematite suggest 5.5% and 3.6% of the (remanence carrying) ferromagnetic mass is magnetite (using the S-ratio: $-IRM_{0.1T}/SIRM$) for the Rhuddanian-Phase-I and Phase-II-Sheinwoodian respectively, and 0.7% for the Ordovician samples (Fig. 5b). Using the less extensive mixing experiments of Bloemendal et al. (1992), but with 0.025 μm and 0.36 μm magnetite and haematite respectively, suggests 15%, 13% and 6% magnetite for the same age intervals using the S-ratio (for the S-ratio: $-IRM_{0.3T}/SIRM$). As is typical for mixed ferromagnetic mineralogies (Frank and Nowaczyk 2008), these data indicate magnetic dominance by magnetite (or maghaemite), but in this case ferromagnetic mass-dominance by haematite.

Samples have similar $\% \chi_{FD}$ with $2.8 \pm 1.8\%$ in Ordovician limestones and $2.3 \pm 0.5\%$ in Llandovery mudstones, but the Ordovician samples have larger χ_{ARM} ($5.8 \pm 0.4 \times 10^{-8} \text{ m}^3/\text{kg}$ compared to $3.9 \pm 0.4 \times 10^{-8} \text{ m}^3/\text{kg}$ see SI Fig. S2c) indicating similar low contents of superparamagnetic magnetite, but probably more ultra-fine magnetite mineral content in the limestones compared to the mudstones (using comparison to synthetics of Peters and Dekkers 2003).

Hysteresis parameters σ_{hys} and B_{rh}/B_{cr} of Fabian (2003) indicating domain state (Roberts et al. 2019), suggest largely multidomain behaviour with possibly some single domain (SD) behaviour (shown as lower B_{rh}/B_{cr} ; Fabian 2003), and possibly some superparamagnetic ferrimagnets (shown by larger σ_{hys}) (Fig. 4b). Those with lower paramagnetic content have more pot-bellied shaped hysteresis curves (mostly $\sigma_{hys} > 0.6$), an effect which is not related to haematite content changes (see SI Fig 2d), but is likely related to slightly differing grain size populations of ferrimagnets (Tauxe et al. 1996; Tauxe et al. 2002). The domain state diagrams of Tauxe et al. (2002) and Lascau et al. (2010) in Figures 4c and 4d, also suggests MD behaviour dominates. Compared to trends seen in the ocean floor basalt compositions (TM60 and low Ti-magnetite trends in Fig. 4c), the data suggests that our samples largely contain low Ti-magnetites. The Lascau plot (Fig. 4d) suggests that there is a probable mixing trend with some SD magnetite especially for the Hirnantian samples. In Fig. 4c the shift of most of the data away from the low-Ti magnetite trend to larger B_c values

suggests that these grains are in part stressed, which increases the uniaxial magnetic anisotropy constant, and so B_c (Tauxe et al. 2002). This may be a result of them being inclusions in silicate hosts (e.g. quartz, feldspar etc; Hounslow and Maher 1999), since the shift to larger B_c seems to be more important in those with larger paramagnetic contents (Fig. 4c). In addition, SIRM and $\chi_{ARM}/SIRM$ values are rather similar to inclusions in clastic silicates sourced from low and intermediate grade basement (non-gneiss regions) from Western Europe (Figs. 4d, 5a; Hounslow and Morton 2004).

The portable-XRF data from Zwierzyniec-1 show that in the Phase-I interval, the peak in K_{scf} is expressed by larger carbonate-free Fe_2O_3 and TiO_2 contents (Fig. 5c,d), and larger TiO_2/Cr ratios (i.e. relatively lower Cr contents in the Phase-I interval). The Phase-I interval is also principally sulphur-poor and low in pyrite, with average pyrite abundances, based on XRD of 0.38%, 3.7%, 2.5% in Phase-I, Phase-II and younger than Phase-II respectively (see SI Fig. S4s). A small group of Fe_2O_3 -rich and sulphur-rich samples (i.e. pyrite rich), have lower K_{scf} (Fig. 5c). This indicates that the relationship between Fe_2O_3 and MS is not driven by magnetic sulphide concentrations, confirming the rock magnetic data. Pyrite has an effective MS close to zero and is less important than diamagnetic minerals in terms of contribution to MS (Rochette 1987). The total TiO_2 content in shales can be an expression of the clay, and Al_2O_3 content (and sorting), since TiO_2 minerals are often concentrated in the finer fractions (Garcia et al. 1994). As well as hosted in Ti-magnetite, TiO_2 in sediments can be hosted within variety of other weakly magnetic minerals such ilmenite, titanite, micas and sphene (Morad 1988; Nesbitt and Young 1996; Pe-Piper et al. 2005). A plausible model for the variation of K_{scf} with TiO_2 (Fig. 5d), is that the lower susceptibility range may be largely hosted by paramagnetic minerals, and the higher susceptibility (at higher TiO_2), may have a larger magnetite and haematite contribution (with only a little additional Ti; shown as ferromagnetic line in Fig. 5d). Mn can also contribute to paramagnetic susceptibility (Rochette 1987, 1988), and shows a weaker but similar paramagnetic-like relationship at low K_{scf} values (dashed line in Fig. 5e).

To summarise, these data indicate that the magnetic mineral contribution to the MS is a mixture of: 1) diamagnetic dilution from calcite (Fig. 3b; and also other diamagnetics such as quartz, feldspar). 2) Paramagnetic contributions that vary but appear to be lowest in limestones, up to around 80% in the mudstones (Fig. 4a). The mineralogical source of this paramagnetism is uncertain, but likely Fe-rich clays (associated with TiO_2 ; Fig. 5c,d) and chlorite(?) may be important, possibly assisted by magnetic contributions from Mn (Fig. 5e). 3) The ferrimagnetic mineral abundance is enhanced in the Phase-I peak in K_{surf} (Fig. 2), with this enhancement largest in the Tłuszcz IG-1 core (i.e. Fig. 5a). 4) The ferrimagnetic mineralogy is a combination of magnetically dominant, multidomain, low Ti-magnetite (Fig. 4c), with indications of a smaller proportion of single domain magnetite especially in the limestones (Fig. 4d). Small differences in the coercivity of the multidomain grains (or sub-populations of sizes) appear to be mostly related to the %paramagnetic content rather than any stratigraphic changes, and may be a reflection of differing magnetite inclusion populations. 5) A magnetically smaller content of haematite is present, which has a larger

mass contribution (ca. 90- 95% of total Fe-oxide content) compared to the magnetite (Fig. 5b).

5. Palaeoredox conditions in Zwiernyniec-1

Mo and U contents are particularly prone to sediment uptake during early diagenesis (Algeo and Tribovillard 2009; Zhou et al. 2015). When expressed as enrichment factors Mo_{EF} , U_{EF} (using normalisation to PAAS; Tribovillard et al. 2006), they indicate suboxic waters for the Phase-I interval, changing to more sulphidic conditions in the younger parts of Phase-II and into the Homerian (Fig. 6a). This co-variation trend in Mo-U is typically seen in present day unrestricted oceans, and has also been detected by Gambacorta et al. (2019) from a similar age interval in the Baltic Basin (Fig. 6a).

We define redox thresholds using the approach of Algeo and Li (2020), which indicates that C_{org}/P gives the clearest ‘T2/T3’ redox thresholds followed by DOP_T , and Zn_{EF} (Fig. 6b,c). Other redox-sensitive elements gave less clear results (SI Fig. S5, S6), perhaps due to a greater detrital contribution. Biplots of C_{org}/P and Zn_{EF} against DOP_T using any of these thresholds clearly subdivide the largely suboxic Phase-I samples, from the others in the euxinic (sulphidic) fields (Fig. 6b, c). Redox thresholds for Mo_{EF} and U_{EF} were indistinguishable in our data, as observed by the test cases of Algeo and Li (2020). The Phase-I interval also has lower (XRD) pyrite contents (SI Fig. S4c) and total organic carbon (TOC) ~50% smaller than younger intervals. The low pyrite content in Phase-I samples (on average 0.38%, compared to 2.9% in younger strata) presumably relates either to late-stage sulphidic diagenesis, or fluctuating but generally low oxygen levels (cf. Algeo and Li 2020), accounting for the grey colour of the Phase-I suboxic mudstones. The relative order of degree of anoxia expressed by Zn_{EF} , Mo_{EF} and U_{EF} , is similar for all four stratigraphic intervals (Figs. 6a,c; 7c,f), but inverted for the C_{org}/P indicator in the stratigraphic intervals in the euxinic field (compare Figs. 6b,c). The difference for the C_{org}/P redox proxy probably relates to secondary effects such as feedback mechanisms with atmospheric pCO_2 (Algeo and Ingall 2007), or differing detrital phosphate contents (Fig. 7h) or nutrient delivery and water depth (Schoepfer et al. 2015).

Bennett and Canfield (2020) have suggested alternative palaeoredox-state boundaries based on data from modern ocean cores (Fig. 6d). The V/Al proxy seems to be reasonably consistent with the approach of Algeo and Li (2020), but the Mo/Al and U/Al proxies need substantial offset ‘adjustments’ to be compatible (arrows in Fig. 6d). A possible explanation of this is different Mo and U contents in Silurian seawater, which may have been ~25% and ~40% lower (respectively), than modern seawater, due to long-duration changes in the anoxia of Paleozoic seawater (Algeo 2004; Meyer et al. 2008; Stockey et al. 2020). A V/Al value less than $\sim 23 \mu g g^{-1}$ (equivalent to $V_{EF} = 1.38$; Fig. 6d) appears to indicate weak vanadium accumulation in oxic environments (or sites below the oxygen minimum zone, OMZ), due to the absence of capturing sulphide near the sediment surface (Bennett and Canfield 2020). Using the $V_{EF} = 1.38$ and $V_{EF} = 2.77$ thresholds applied to Zwiernyniec-1, in combination with the other redox proxies (Fig. 7d), allows a subdivision of stratigraphic intervals into three oceanic states. Firstly, fully-oxic oceanic waters, which include most of the Hirnantian,

Phase-I, and a ~3 m interval in Rh3 age. These are shown as the blue intervals in the oceanic-state column in Fig. 7h. Secondly, oxic waters below the OMZ, which include principally the middle Rhuddanian and the later-part of Phase-II. These are the purple intervals in oceanic state in Fig. 7h. Thirdly, waters that were either euxinic or within the OMZ (uncoloured intervals in Fig. 7h).

In the Phase-I interval, suboxic conditions have a lower boundary which may preserve a number of palaeoredox-like boundaries due to non-steady state diagenesis (Thomson et al. 1998a, 1999; Kasten et al. 2003). At 2968.0- 2968.42 m are highs in Ce_{EF} , Pb_{EF} , Co_{EF} , Ba and sum of the rare earth elements (ΣREE ; Fig. 7f,g). This is followed below with spikes in Ni_{EF} , Zn_{EF} , U_{EF} , Mo_{EF} , V_{EF} and Tl/Th at 2968.8-2969.5 m, and secondary highs in U_{EF} , Mo_{EF} , Ce_{EF} , V_{EF} and Tl/Th at 2970.49m (Fig. 7c,d,e,f). The interval 2969.1 - 2969.8 m is a calcite veined, slightly brecciated interval, interpreted as a fault zone. The interval between 2968.8m- 2971.0 m has particularly high TOC at >4% with 10.3% TOC at 2969.15 m. Our interpretation is that the upper part of this interval (above 2969.1 m) preserves palaeoredox fronts like those known from a number of modern - Quaternary sediments (Thomson et al. 1998b). The maximum Ba content of 1030 ppm (TOC = 0.29%) is immediately above the TOC-rich interval at 2968.42 m, and likely preserves a 'burndown' event (Thomson et al. 1999) from the overlying suboxic interval. Burn-down events occur during non-steady diagenesis, so that oxic fronts migrate downwards, rather than upwards as in progressive diagenetic burial and pore fluid evolution (Kasten et al. 2003).

The position of palaeoredox fronts are not always stable to later diagenesis, but Tl/Th fronts, which occur on the reduced-side of the oxic front appear to be the most stable (like V_{EF}) to later change (Thomson et al. 1999). Hence, the palaeo-oxic front is inferred to be around 2968.8 m (marked in Fig. 7g) probably at or above where cm-sized pyrite nodules are developed at 2968.7-2968.8m (although pyrite concentrations are not necessarily indicative of palaeoredox fronts; Thomson et al. 1998b).

Near the upper boundary of the Phase-I interval are also a number of peaks in redox sensitive elements with highs of U_{EF} , V_{EF} and Tl/Th at 2950.46m, followed below at 2953 - 2953.4 m by spikes of Mo_{EF} , Co_{EF} , Ni_{EF} , V_{EF} (secondary peak), Zn_{EF} and Pb_{EF} (Figs. 7c,d,e). Considering that sampling has probably not captured the detail of these palaeoredox peaks, which are normally only ~10 cm wide (Thomson et al. 1998a), the upper palaeoredox boundary is estimated at ~ 2951 m (marked in Fig. 7g), just below the upper Tl/Th and V_{EF} peaks (Fig. 7d,e), probably near the hiatus at 2951.25 m.

A second set of palaeoredox fronts also likely occurs in the upper Rhuddanian, but sampling has not captured the detail of the peaks, but may be best represented by the rapid declines in Tl/Th (Fig. 7e, fronts labelled on Fig. 7g), as typically demarcated in suboxic intervals in Quaternary sediments (Thomson et al. 1998a). A sharp downwards change to paler-grey mudstone is present at 2971.8 m, but the lower change to larger Tl/Th values between 2974.4 - 2975.0 m is not marked by a change to darker mudstone. This upper Rhuddanian suboxic interval also has an associated small increase in K_{surf} (Fig. 7a).

The Σ REE is strongly related to the Al_2O_3 content (and Sc content), indicating, as commonly observed elsewhere (Cullers et al. 1987; Condie 1993), that the REE content is related to clay content, and is diluted by carbonate content (as in the Hirnantian Fig. 7g) and quartz content (Fig. 7b). Σ REE is particularly enhanced through the upper Rhuddanian to middle-part of the Phase-II interval (Fig. 7g). The patterns of REE element concentrations are strongly influenced by uptake into diagenetic phosphate, associated particularly with the sub-oxic intervals, and complementary depletion of phosphate (and so REE) by anoxia in the lower-middle Rhuddanian (Fig. 7g,i). Since phosphate in sediments is often dominated by diagenetic capture (Algeo and Li 2020) the REE data are not utilised here (further details are in SI Fig. S7).

6. Weathering-related changes in sediment sources in Zwierzyniec-1

The larger chemical index of alteration (CIA, Table 2) for the Rhuddanian and Phase-I intervals indicates this interval contains more weathered feldspars than younger intervals (Fig. 8a). Likewise, the CIA versus WIP_R indices clearly demarcate the more weathered sources in the Rhuddanian and Phase-I intervals of Zwierzyniec-1 (dashed line separator in Fig. 8a). Lower values of these indices in Phase-II and younger intervals (Fig. 9c) indicate their similarity to a range of Precambrian igneous rocks (Fig. 8a). In contrast, the STI_R index, shows the separation (at ca. $\text{STI}_R > 18$) of most of the Phase-I and II samples from younger and older intervals (Figs. 8b, 9b). This STI_R index may be most applicable to potential Paleoproterozoic and Archean sources from the East European Craton, with intense ‘tropical weathering’ in the low latitude Silurian (Table 2). The overall consistency of these indices suggests that the Phase-I interval received the most weathered source material, probably little affected by source rock compositional changes (Ohta and Arai 2007).

The average Th/U ratio (particularly when $\text{Th/U} > \sim 3.8$) has also been used as a weathering proxy for sediment derived from modern intensely weathered regions, such as the Congo Basin where the average $\text{Th/U} = 5.9 \pm 1.9$ (1σ). Here, it also reflects oxidative loss of U through source weathering (Dupré et al. 1996; Taylor and McLennan 1985; McLennan and Taylor 1991; Zhang et al. 2014a). The average Th/U ratio for Phase-I samples is 5.2 ± 1.9 (1σ), which may like STI_R reflect intense weathering of the Phase-I sediment sources. However, during anoxic diagenesis uranium will also be impacted by diagenetic uptake (Tribovillard et al. 2006).

The strong association between K_{surf} and Fe_2O_3 content (Figs. 5c, 9a, d) and its connection to enhanced weathering may be related to increased Fe-delivery from oxic (non gleyed) palaeosols. This is likely connected to enhanced Fe-oxide content (and enhanced MS) and increased Fe-content (Retallack et al. 2003; Torrent et al. 2006), since Fe is often a resistate element in oxic palaeosols (Maynard 1992; Zhang et al. 2007). However, Fe-retention does depend on a variety of soil-related and later events as well as parent rock sources (Driese et al. 1992; Preetz et al. 2017).

7. Provenance of sediments in Zwierzyniec-1

Provenance evaluation selected Zr/Sc, Ga/Sc, Sc/Cr, TiO₂/Nb and Zr/Nb ratio's as the best provenance indicators (Table 3). Ratios of Th/Sc, Zr/Th, and Zr/TiO₂ were excluded due to rather noisier behaviour and having a similar response to Zr/Sc. Cluster analysis indicates that the Zwierzyniec-1 succession can be divided into two major provenance zones (PZ1 and PZ2) largely based on the Sc/Cr ratio (Fig. 10e, g). Fuzzy cluster analysis selected 6 'resistate clusters' (Fig. 10f) as the optimum for this dataset (using the fuzzy silhouette validity index; Ferraro et al. 2019). This was consistent with interpretation of the hierarchical cluster analysis. Provenance subzones were interpreted primarily using the fuzzy cluster membership probability (circles in Fig. 10f, larger circles indicate more association with the respective cluster), combined with the closest hard-cluster partition, plus evaluation of clusters from the K-mean and hierarchical cluster analysis. The pairs of subzones R₁, R₂; M₁, M₂ and W₁, W₂ are rather similar to each other within each pair, since dominance of the B, 1C and 2C+3C resistate clusters define these three subdivisions respectively (Fig. 10f,g; Table 3). The boundaries between provenance subzones are to some extent transitional due to the noise in the ratio data, with the sharpest-defined boundaries for the A and R₂ subzones. Subzone statistics are shown in Table 3.

Zircon ages from the Cambrian on the margin of the East European Craton (EEC) indicate a wide age-range of sediment sources from Archean to Ediacaran, with likely source peaks in the Ediacaran (~0.6 Ga) and early Mesoproterozoic to late Paleoproterozoic (~1.5-1.9 Ga) (Valverde-Vaquero et al. 2000; Paszkowski et al. 2019; Habryn et al. 2020). Since zircons are primarily sourced from felsic igneous rocks, basic igneous sources will be underrepresented in zircon populations (Puetz and Condie 2020). Proterozoic and Archean zircons are sourced from the various basement components of the EEC or its Mesoproterozoic to Neoproterozoic sedimentary cover (Paszkowski et al. 2019). On the flank of the EEC, Ediacaran age zircons are likely sourced from the Volyn volcanic complex (Paszkowski et al. 2019; Poprawa et al. 2020), although similar aged zircons in the Holy Cross Mts and Brunovistula terranes to the SW have been associated with either exotic Neoproterozoic volcanic arc sources, or the basement to these blocks (Żelaźniewicz et al. 2020; Habryn et al. 2020). Zircon ages in Ordovician to Silurian units in Poland are little studied, but may have had similar sources to the Cambrian sediments (Nawrocki et al. 2007), which in the HCM was supplied from the NE (Jaworowski and Sikorska 2006).

The provenance ratios in Zwierzyniec-1, were compared to the trace element ratios in the bulk-rock database from the basement complexes of the EEC (see Section 3.3). The details of this comparison are in SI section 4, but there are five key conclusions from this.

Firstly, element ratios used in the provenance zonation show a much lower degree of variability than the EEC source rocks, indicating both a large degree of homogenisation of source rock composition (typical for shales; McLennan and Taylor 1991), and by inference the rather small provenance differences shown by the provenance zones (PZ1 to PZ2) and subzones (H to W₂; Fig. 10g). This suggests that localised source inputs were unimportant.

Secondly, element ratios cannot unravel the complex mix of likely spatial variations and compositional differences in igneous and metamorphic source-rocks, but do provide clues to the origins of the likely major provenance differences.

Thirdly, the division into zones PZ1 and PZ2 is probably the result of a small switch between magnesian (larger in PZ1) to ferroan (larger in PZ2) igneous rock sources (petrogenetic divisions of Frost et al. 2001; Frost and Frost 2008) with the magnesian-differentiation route (e.g. cordilleran type granitoids; Frost et al. 2001) enriched in Cr (Figs. 9e, 10e). The more Fe-enrichment differentiation route (ferroan, A-type granitoids) may explain the enrichment in Fe₂O₃ seen in the M₁ and M₂ subzones (Fig. 9d). A less likely possibility is that provenance zone PZ1 is enriched in Archean metamorphic sources (and PZ2 with Paleoproterozoic sources), which seems unlikely considering the often limited supply of Archean zircons in the EEC Mesoproterozoic-Neoproterozoic sedimentary cover (Paszkowski et al. 2019). A comparable Cr-enriched interval to that in Zwierzyniec-1 (Fig. 9e), is also seen in the Aizpute-41 core (Latvia) in the Upper Ordovician to mid-part of the *cypus* Biozone. Its upper boundary is expressed as a decline in Cr content at the first red-mudstone; Loydell et al. 2003; Kiipli et al. 2009). It is also seen in the Upper Ordovician from Scania (Schovsbo 2003). The switch between PZ1 to the PZ2 zone is probably a major change in provenance at the regional level.

Fourthly, step changes in Zr/Nb and TiO₂/Nb ratios at the boundary between the W₁ / W₂ subzones (Fig. 10c; SI Fig. S10) suggests either more East Sarmatian sources and/or more basic (less silicic) igneous or meta-igneous sources in the W₂ subzone.

Finally, the switch in Zr/Sc ratio (Fig. 10b) near the boundary between the M₁-M₂ subzones may be an upwards change to rather more silicic igneous rock sources, or an increased contribution from W Sarmatian metasediments.

8. Diagenetic, weathering and provenance controls on magnetic susceptibility

Using the ICP OES-MS data of Sullivan et al. (2018) from Zwierzyniec-1, the largest Spearman correlation coefficients against carbonate-free susceptibility (χ_{cf}) ranked in order for the first 15, are: STI_R ($R_s = 0.66$), Al₂O₃^N, Th, TiO₂^L, La, Ta, Zr, Hf, Ga, Nd, Ce, Fe₂O₃^L, Pr, Nb, Sc ($R_s = 0.54$). This excluded the faulted-interval (Fig. 9) and the Ordovician (details of R_s values are in SI Table S5). Al₂O₃ and Ga are associated with clays. TiO₂, Ta, Nb and Sc are associated with Ti-bearing minerals such as ilmenite, rutile and titanite, and Th, Zr, Hf and Ce with heavy minerals such as zircon, monazite and allanite (Condie 1993; Pe-Piper et al. 2008; Laveuf and Cornu 2009; Randive et al. 2014). La, Ce, Pr and Nd are the light rare earths (LREE), and rare earths tend to be associated with the clay fraction (Condie 1993), and in the data here, have strong associations with TiO₂, Ta and Sc (SI Table S5). In comparison to the silt-fraction, the clay-fraction can be enhanced in LREE (Cullers et al. 1987). Ti and Sc (amongst others; Tischendorf et al. 2001) could also act as potential substitutions in mica. Thorium and Nb are highly immobile to weathering (Kurtz et al. 2000), so with STI_R having the largest R_s , suggests χ_{cf} may be associated here with resistate components. Although these

individual relationships to χ_{cf} may help explain some of the connected mineralogical controls on the magnetic variation, their contribution to a joint expression of the changes in MS is explored below.

Controls on χ_{cf} and geochemistry were additionally investigated using, principal component analysis (PCA) on the Silurian interval in Zwierzyniec-1 (up to 2900 m; Fig. 2b). Eleven variables were selected for the PCA, using multiple linear regression (with a final adjusted R^2 of 0.87; Fig. 11a). The 11 selected variables are shown in the bottom part of Fig. 11b, along with the two elements/indices with the largest cross-correlation (R_s) to the chosen element/index, illustrating their co-associations. The variables entered in the MLR, but excluded in the final model are also shown in Fig. 11a (in grey), as possibly informative of co-related controls on χ_{cf} variation. The four first selected are Fe_2O_3 , weathering indices WIP_R and STI_R and K_2O^N (Figs. 9b, 11a). Those 11 variables (plus χ_{cf} .) chosen for the PCA are displayed in loading plots in Figs. 11b, c, d.

The positive loadings on principal component 1 (PC1) include a wide range of magnetic, weathering (STI_R), heavy-mineral and clay related factors and the negative loadings are redox-related factors and CaO^L (top panel in Fig. 11b, x-axis on Fig. 11c). Positive loadings on PC2 include $Fe_2O_3^L$, MnO^L , STI_R and CaO^L , and large negative loadings are Cr and WIP_R (top panel Fig. 11b, y-axis on Fig. 11c). Zn is correlated with U, V and MnO^L negatively related to Mo (Figs. 11b,c, 7c,f), so negative PC1 and PC2 loadings relate to the reducing end of the oxic \rightarrow reducing relationships in Fig. 6a, shown as the '+reducing' large arrow in Fig. 11c.

Positive PC1 and negative PC2 loadings relate to increased alkali loss and feldspar loss which is evidently linked to increased Cr, Sc and CIA (Sc, CIA have largest R_s with Cr; bottom panel, Fig. 11b). Cr_{EF} is larger in the Rhuddanian and Hirnantian, as is WIP_R , so Cr contents (and PC2 values; Figs. 9c, 11c) effectively sub-divide the core units into older (pre-Telychian) and younger intervals (Fig. 9e). Cr is not simply controlled by redox conditions (Tribovillard et al. 2006) and its association here with Sc (and also TiO_2 , Ta with $R_s > 0.7$), and magnetic resistate Cr-bearing phases (Hounslow 1996), suggests the Cr_{EF} changes are primarily a heavy-mineral signal (large arrow in Fig. 11c). CaO^L opposes this heavy-mineral trend (larger PC2, smaller PC1; Fig. 11c). CaO^L is related to the dual (plagioclase feldspar+ calcite) contributions with negative loadings on PC1 (Fig. 11c), representing the carbonate dilution of the clastic signal (WIP_R is negatively related to carbonate (calcite+dolomite) content; bottom panel, Fig. 11b). In the PC1-PC2 plot the Phase-I samples are spread-out between the outliers with high χ_{cf} and STI_R (high PC1, PC2; Fig. 11c), and those indicating heavy minerals (higher Cr, Cu, Fig. 11c, and related Sc, Th, Lu, Yb, Fig. 11b) at large PC1 and moderate PC2 (Fig. 11c). Although Cu is commonly mobilised during diagenesis and associated with pyrite (Tribovillard et al. 2006), its opposite PCA response with S (and an R_s of -0.32 against S), indicates that it is here mainly associated with the clay fraction (at $R_s > 0.6$, co-associates Lu, Yb; bottom panel, Fig. 11b and Cr, K_2O^N , Fig. 11c). This is shown particularly by Cu_{EF} and K_2O^N having a similar stratigraphic response (Fig. 9b, g). Cu with

this kind of behaviour is known in some modern hemipelagic deposits, where it is associated with Fe-smectites (Pedersen et al. 1986).

Principal component 3 (PC3) has large positive loadings for χ_{cf} , $Fe_2O_3^L$ and STI_R and large negative loadings for Cu, K_2O^N and Zn (y-axis, Fig. 11d). This indicates that the positive PC3 loadings represent magnetic plus increased intense weathering. The spread and overlap of all except the Phase-I sample sets from negative PC1, +PC3 loadings towards -PC3, +PC1 (Fig. 11d) probably represent a grain size/sorting relationship with concentration of Cu (and REE) and heavy minerals in the clay fraction (elevated $Al_2O_3^N$, K_2O^N) as commonly observed (Cullers et al. 1987; Condie 1993; Xie et al. 2014). In contrast, Phase-I samples are spread out towards high positive PC3 loadings, and middling PC3 loadings. Large PC3 loadings are also shown by WIP_R indicating linked magnetic+weathering behaviour. The middling PC3 loadings for some Phase-I samples are the heavy mineral+clay (i.e. Cr, MnO^L , K_2O^N , Al_2O_3) response shown by the other stratigraphic sets (Fig. 11d).

Enrichment (EF) factors for Fe and Mn suppress the grain size (clay content) control (Van der Weijden 2002), and so may in effect 'remove' any paramagnetic contribution hosted in clays, leaving a non-clay related signal. Fe_{EF} shows enrichment over most of Phase-I with some evidence of expression of the Phase-I MS sub-peaks a,b,c (Fig. 9a,d). These sub-peaks may be also expressed in Mn_{EF} (Fig. 9f), perhaps an expression of Mn-rich magnetites which are more resistant to diagenetic dissolution than Ti-magnetites (Hounslow 1996; Nowacyk 2011). Nb and Sn have the two largest positive R_s values (>0.49) with MnO^L , supporting the suggestion that Mn is associated with resistate minerals.

There is also a second interval of Fe_2O_3 enrichment (larger Fe_{EF} ; dotted boundaries in Fig. 9d) in the upper part of Phase-II, which coincides with the interval deposited below an OMZ (oceanic state; Fig. 7h). Here spikes in Fe_{EF} in Phase-II are attributed to localised pyritic levels (richer in S) and possibly ankerite. The Fe_{EF} spike in the youngest part of Phase-I is also shown in the more-closely spaced portable-XRF values of %Fe (Fig. 9a). Mn_{EF} shows some similarity to Fe_{EF} over Phase-I, but enrichments extend into the Rhuddanian and Phase-II (Fig. 9f). Using a wider stratigraphic range MnO is associated with CaO and carbonate phases (Sullivan et al. 2018) and is also much enriched in the Hirnantian carbonates (Fig. 9f). However, in the Silurian MnO appears to be related to larger STI_R and K_2O^N (Fig. 9b, f).

To summarise these correlation and PCA relationships, suggest that the MS signal to a large extent is a reflection of source weathering, superimposed on a diagenetic loss due to degree of anoxia. The locus of the MS signal is perhaps, as expected, related to the heavy mineral fraction, and its association with resistate elements suggests these may be magnetic phases resistant to weathering and anoxia-related Fe-dissolution.

9. Palaeoproductivity and upwelling indices in Zwierzyniec-1

Changes in palaeoproductivity have been hypothesized by Zhang et al. (2018) as a key control on the Yangtze Platform marine red beds, in which they use the cooler to warmer climatic modes of Jeppsson (1990), driving alternating downwelling (producing red beds) and

upwelling (promoting productivity) oceanic circulations. This hypothesis is tested using the geochemical data from Zwierzyniec-1.

The $Mn_{EF} \times CO_{EF}$ proxy for upwelling and restricted oceanic anoxic settings proposed by Sweere et al. (2016), indicates that only the lower Rhuddanian and part of the lower Homerian were in an upwelling state, and only part of the middle Sheinwoodian were consistently in a restricted circulation state (Fig. 12d).

The palaeoproductivity flux estimates show a lower interval (Hirnantian - middle Telychian) in which the C_{org} and P_{xs} estimates are out of phase, and above this a younger interval in which they are in-phase (Figs. 12b,c). Schoepfer et al. (2015) have interpreted such relationships as a redox-dominant and productivity-dominant control on geochemical productivity proxies (Fig. 12f). With the redox dominant scenario, P_{xs} will be larger under oxidizing conditions (i.e. Hirnantian to middle Telychian; Fig. 12c), since P is more efficiently trapped in oxygen rich porewaters, via critical interactions with Fe-oxide/oxyhydroxides (Tribovillard et al. 2006). The magnetic data suggests that the Hirnantian and Phase-I intervals are enriched in Fe-oxides (Fig. 5a). Under euxinic conditions (like those seen in most of the Rhuddanian) P can be recycled into the water column, where it may promote productivity, producing a feedback, promoting larger C_{org} (Tribovillard et al. 2006). Hence, in Zwierzyniec-1, C_{org} may provide a more direct indication of oceanic palaeoproductivity (Schoepfer et al. 2015), the situation inferred here. Primary palaeoproductivity estimates (using C_{org} flux equations in Schoepfer et al. 2015) shows relatively-similar average values throughout the Hirnantian - Telychian (Fig. 12b), but changes to increasing primary palaeoproductivity in the upper Telychian to lower Homerian. The lowest primary palaeoproductivity was during the Hirnantian and lower part of Phase-I (Fig. 12b).

10. Discussion

10.1 Timing of marine red mudstones and oxygenation events

In northern European sections, the marine red beds are not synchronous, but rather occupy an interval, largely in the late Telychian, that also includes non-red beds probably deposited under suboxic conditions (Fig. 13). In the non red beds, the originally deposited Fe-oxide content (or diagenetically produced Fe-oxides; Turner 1979; Kiipli et al. 2000a) was likely depleted during later diagenesis (Zhang et al. 2014b), as is fairly typical for initially oxic diagenesis (Weibel and Friis 2004; Zhang et al. 2014b). The poor synchronicity of red beds indicates either a range of local redox-related factors controlled the fully-oxic (i.e. red) nature of these sediments, or the stratigraphic ages of red bed units are not understood well-enough. In the Llandoverly, the earliest evidence of oxic/suboxic conditions is on the EEC margin, where suboxic conditions briefly appear in the Rh3 stage slice in Zwierzyniec-1 and red-mudstones in the Aizpute-41 core (~Rh3 age; Kiipli et al. 2009, 2012), and also in the Ventspils-D3 core and Gotland subsurface (Table 1).

In Zwierzyniec-1 the base of the main sub-oxic interval (at 2968 m) is in the upper *leptotheca* or lower *convolutus* biozones (mid Ae2 slice), but the MS increase appears in the mid-part of the *turriculatus* Biozone (uppermost Te1), dated in the Tłuszcz core. This lower

stratigraphic level in Zwierzyniec-1, may be a reflection of oxic burn-down (see Thomson et al. 1998a 1999) from the overlying sub-oxic interval into the condensed Aeronian in the core. In the Aizpute-41 core the occurrence of Telychian red beds starts in the base of the Te1 stage slice, *guerichi* Biozone (Loydell et al. 2003; Young et al. 2020).

At Buttington Quarry, on the eastern edge of the Welsh Basin red beds start near the base of the Te2 stage slice (Hounslow et al. 2021b). The beginning of red beds during uppermost Te1 to lowermost Te2 stage slice is typical for the Welsh borders in Britain (Table 1; Fig. 13). Other areas on Avalonia show the first development of red beds later in the Te2 Stage slice (Fig. 13). This later timing is rather typical of areas situated on Laurentia, and the deeper oceanic settings in southern Scotland (Fig. 13; Table 1).

On Baltica the red beds end by the lower to mid-parts of the Te3 stage slice (Fig. 13), like lower Te3 in the Banwy River section in Wales (Loydell and Cave 1996) and in the upper Te3 stage slice at Buttington Quarry (Hounslow et al. 2021b). Elsewhere, the last occurrence of red beds are not precisely dated, since older studies (Table 1) have used the *crenulata* Biozone definition of Rickards (1976), rather than the finer-scale *M. crenulata*-*C. insectus* subdivisions of Zalasiewicz et al. (2009) and Loydell (2012). At Backside Beck (in the Howgill Fells), the last red mudstones may be around the Te4/Te5 slice boundary (based on magnetostratigraphic correlations; Hounslow et al. 2021b), similar to the Dolgau Mudstones in east Wales (Wilson et al. 2016). In the Zwierzyniec-1 core, the last suboxic level (at 2951 m) is in the lower part of the *lapworthi* Biozone (Te4).

In a geographically wider context ‘oxygenation’ events are seen in other European Telychian green or grey mudstones. In the Northern Holy Cross Mountains, Telychian (Te2-Te3) grey mudstones are suboxic, based on trace element ratios and absence of pyrite framboids with a possible lower level of suboxia around the Ae2/Ae3 boundary (Trela et al. 2016; Smolarek et al. 2017). In the Baltic Basin in northern Poland, suboxia in Telychian green-grey mudstones was inferred by Gambacorta et al. (2019) using TOC and trace element ratios. Like in Zwierzyniec-1, these events we associate with the Telychian ‘oxygenation’ event which contributed to red bed formation in other European basins. In contrast, the Röstånga-1 core (Fig. 1) from the deep foreland basin of SW Sweden does not show the Telychian oxygenation event in Fe-speciation and trace element ratio data (Young et al. 2020).

The hypotheses of Ziegler and McKerrow (1975) and Loydell (1998) for the origin of Telychian marine red beds are linked to the delivery of more terrestrial oxidized clastics, tied to sea level change, either during transgression or regression. Recently proposed Llandovery global sea-level curves possess some similarity in highstand timing, but also a lack of detailed coherence (Johnson 2010; Davies et al. 2016; Fig. 13a). Highstands around the late Rhuddannian are consistent between Johnson (2010) and Davies et al. (2016), but not Haq and Schutter (2008). A eustatic highstand around the Ae2-Ae3 boundary of Davies et al. (2016) and Johnson (2010) are not represented in red-mudstones, but may be in suboxic mudstones in the Holy Cross Mts in Poland (Trela et al. 2016; Smolarek et al. 2017). All three compilations give a eustatic highstand within or near the base of the Te1 stage slice,

similar to the red mudstones in the Aizpute-41 core (Fig. 13). Inference of consistent late Telychian (Te3-Te4) highstands is less clear, although some infer this interval had some of the highest sea-levels of the Llandovery (Loydell 1998; Johnson 2010). Nevertheless, it is clear that where detailed section data is available, red-mudstones are non-synchronous with each other, which precludes a direct connection with sea-level change, but does not exclude the possibility that it may have a secondary influence at a longer temporal-scale than the duration of individual red beds. Therefore, it seems unlikely either eustatic-driven transgression or regression had a direct control on red bed formation.

10.2 Environmental controls on sediment supply and magnetic susceptibility

The peak in K_{surf} during Phase-I is related to an increase in Fe_2O_3 , expressed in both detrital (Ti-bearing) Fe-bearing silicates and magnetite+haematite (Fig. 5a, c, d). In the Phase-I interval in Zwierzyniec-1, the greater preservation of magnetite+haematite is due to the suboxic diagenesis in this interval (based on the redox geochemistry). In contrast, in the younger Phase-II interval, the loss of the Fe-oxides has been greater (see section 4.1; Fig. 5a) due to the more euxinic conditions, so any Fe-captured into pyrite is effectively invisible to MS changes (see SI Fig S4 for pyrite data). This and the provenance change (M_1 to M_2) in the upper part of Phase-I is probably responsible for the decline in K_{surf} in the upper part of Phase-I, since the total Fe_2O_3 content is rather similar (Fig. 9a). If the Fe_{EF} is representative of the original Fe-oxide content (Fe not in the clay content as expressed in Al_2O_3), then a second pulse in Fe-oxide content occurs in the younger part of Phase-II, which is invisible to MS since there the Fe is lost to pyrite (Fig. 9d). In the Aizpute-41 core, Fe_2O_3 contents are also elevated (>7%, 949 - 969 m) in the Te1 to middle Te3 interval (Kiipli et al. 2009), suggesting that this Fe_2O_3 increase (and possible MS peak?) may also be expressed on the EEC margin in the Baltic Basin. It is difficult to separate the Fe contributions from weathering-related Fe_2O_3 delivery, from that related to the provenance switch to the M_1+M_2 subzones. This is because the M_1+M_2 subzonal interval has potentially more Fe from ferroan A-type granitoids. However, both the alkali-based CIA index and the Al-Si-Ti based STI_R index are enhanced in the Phase-I samples suggesting that this weathering signal is not an expression of the provenance change shown in the trace element ratios. Our interpretation is that this expression of dual changes is either: 1) that the Phase-I interval has more oxic palaeosol-derived material, or 2) the source material has an enhanced weathering rate (i.e. a larger resistate Fe_2O_3 content). The former interpretation is more compatible with this being linked also to a provenance switch also (i.e. more material from A-type granitoids), since increased delivery from palaeosols could be partly a change in spatial delivery patterns.

Outside of the Telychian, the K_{surf} changes are rather more subtle, and likely reflect source differences modulated by redox conditions. These may be modulated by carbonate (or quartz) dilution effects, like in the Wenlock (Zenkner and Kozłowski 2017). Generally low MS is seen in the lower to middle Rhuddanian in Polish sections and cores (Fig. 2a,b) and is related to a low in Fe_2O_3 and likely low in delivery of Fe-silicates (i.e. paramagnetic phases) to the EEC margin (low Fe_{EF} in Fig. 9d), which may dominate the MS in this interval (Fig. 5a, b,c).

The delivery mechanisms of clastics from the uplands of the EEC to its passive margin basins are not well defined. In Poland and Ukraine, the Llandovery to the east and NE suggests that the EEC uplands were fringed by claystones and marls (Poprawa 2019). Only in the Oslo area of Norway (Baarli 1990b, Worsley et al. 2011) are clastic coastal-sources known. Even in the Lower Cambrian, the EEC flanks seems to have been exceptionally flat and tectonically quiescent (Nielsen and Schovsbo 2011). Silurian carbonate coastal fringe facies may be best represented in Podolia (Ukraine), by Wenlock and Ludlow successions (Teller 1997; Skomski et al. 2008; Jarochowska et al. 2016). Possible emergent sediment sources from the Late Ordovician on the flank of the EEC in the Lublin-Podlasie Basin were largely carbonates (Poprawa 2019), so were not an effective source of silicate mud. However to the SE in the Volyn-Podillya-Moldova Basin, a major Hirnantian-Llandovery hiatus (Poprawa et al. 2018) may have sourced material from erosion of the underlying Ediacaran-Cambrian-Katian clastics. Slope-parallel traction currents were evidently active as a sediment dispersal mechanism (Niezabitowska et al. 2019a), which may have been storm or tide induced, and may have provided effective cross-shelf dispersal mechanisms (Schieber 2016).

An aeolian origin may have been a major source for some of the silt, as has been inferred for dolomitic silt in middle Ludfordian strata in the Baltic Basin (Kozłowski 2015). Dolomite and calcite silt is similar in size to detrital quartz and feldspar in the mud-prone Silurian (Milliken et al. 2018), suggestive also of a possible aeolian contribution. The EEC (and Laurentia) was in a suitable southern position (~5 - 40°S; Torsvik and Cocks 2013) for possible maximum dust sources, if the Paleozoic ice-house modelling for the Permian (Soreghan et al. 2015; Marshall et al. 2016) could be applied to the ice-house world of the Llandovery. Far-travelled Silurian clastics from southern Laurentia have also been proposed to have an aeolian origin (Theilung et al. 2017). Aeolian-generated dust provides a simple means to deliver well-mixed (Taylor and McLennan 1985) sediment sources, derived from terrestrial materials and soils from the EEC into the Polish passive margin. The supplied dust composition would respond to differences in weathering intensity, or changes in soil contributions from the EEC uplands.

In contrast, on the eastern fringe of the Welsh Basin (e.g. Banwy River, Buttington Quarry; Fig. 1) there is clearer evidence of clastic sources in the Llandovery. The northern margin of Pretannia and Midland Craton supplied coarser clastics to the Welsh Basin, with fluvial supply restricted to the narrow margins of the uplands (Cherns et al. 2006). Locations in the Welsh borders with little sediment supply produced nearshore environments directly at the margin, with storms being important components of shelf dispersal (Bridges 1975), consistent with general arguments by Schieber (2016) about mud dispersal mechanisms over larger distances. In northern England the lower Telychian deposits were largely hemipelagic in origin (Rickards 1964; English 1999), consistent with this site being distant from southerly clastic sources and facing the Iapetus Ocean to the north (Bassett et al. 1992). Here, the MS changes reflect changing illite-chlorite contents (English 1999) which may be responding to grain-size changes (via Fe-silicate supply?). There is no data to assess if the Avalonian Telychian is also enhanced in Fe₂O₃ like the Polish margin successions. Changes in MS in the Telychian between Buttington Quarry and Backside Beck have a more complex origin, but

nevertheless share some degree of similarity (Hounslow et al. 2021b). At Backside Beck organic carbonate isotopes from the red-bed interval (Fig. 13) suggest a possible larger terrestrial organic matter contribution (Hounslow et al. 2021b), consistent either with a relative lack of marine organic matter, or enhanced delivery of terrestrial sources.

10.3 Palaeoproductivity and ventilation

Present day oceans have primary productivity between 7- 80 g C cm⁻² kyr⁻¹ (Berger et al 1989; Longhurst et al. 1995; Chavaz et al. 2010), and the primary productivity estimates derived for Zwierzyniec-1 fall within the lower to mid-part of this range (Fig. 12b). Modern continental shelves have an average primary productivity of 39 g C cm⁻² kyr⁻¹ (coastal province of Longhurst et al. 1995), with somewhat lower average values (~19 - 23 g C cm⁻² kyr⁻¹) in regions that are not upwelling, but larger values in upwelling regions, particularly at the present day, on the eastern sides of oceanic basins. Broadly there are three, rate controls on primary productivity, a) nutrient supply, which is largely governed by delivery from land, b) the rate of nutrient remineralisation, and c) the rate of delivery of deep water to the photic zone, which is partly latitude and upwelling dependent (Berger et al. 1989; Chavaz et al. 2010). The Silurian Polish margin palaeoceanography is comparable to modern continental margin situation, so may have not been nutrient-limited like some modern open oceans, distant from clastic inputs. The larger Fe-contents of the Telychian interval also indicates, that the low palaeoproductivity in this interval was not Fe-limited, but perhaps may have been limited by other elements such a molybdenum or phosphate (Berger et al. 1989; Algeo 2004; Pohl et al. 2017).

The Mn_{EF}×Co_{EF} upwelling–restricted proxy of Sweere et al. (2016), indicates that only some of the lower Homerian, and the earliest Rhuddanian, were intervals of upwelling (Fig. 12d). The general circulation modelling of Pohl et al. (2017) shows that the western EEC margin was a region of low to moderate primary productivity in the earliest Silurian, consistent with the C_{org}-based palaeoproductivity estimates here, and the lack of upwelling at this margin. Between the Rhuddanian to Wenlock the Polish margin moved from ~35°S to ~15°S (Torsvik and Cocks 2013; Domeier 2016), with additional anticlockwise rotation of the EEC. This probably moved the Polish margin into a region of lower primary productivity by the Wenlock (Pohl et al. 2017), which is the inverse of productivity changes seen in Zwierzyniec-1 (Fig. 12b,c). This suggests, that the observed palaeoproductivity changes are not related to modifications in palaeogeography. The model of Kiipli et al. (2009) for the origin of marine red beds implicated increased surface current vigor and re-oxygenation of shelf bottom waters, driven by changes in wind regime. Increased water-column mixing may have had the converse effect of promoting palaeoproductivity, by bringing deeper nutrient – rich waters back into the photic zone, coupled, with an increase in upwelling by the larger wind-stress involved. The scenario of Kiipli et al. (2009) does not match what is seen in Zwierzyniec-1.

The Hirnantian oxygenation event is a widespread phenomenon (Melchin et al. 2013) and seems well explained by Hirnantian cooling, linked to increased dissolved oxygen in colder low latitude waters, increased overturning of oceans and so major sea water oxygenation (Zhou et al. 2015; Pohl et al. 2017). The same mechanism does not work for the

Telychian oxygenation event, since this was a warm interval in low palaeolatitudes (Trotter et al. 2016; Fig. 12e), implying that the balance of CO₂ between the ocean and atmosphere was tipped towards more CO₂ in the atmosphere. However, warm intervals could promote nutrient delivery to the continental margins and so could also enhance primary productivity (Beaulieu et al. 2012; Pohl et al. 2017), counter to what is seen on the Polish margin. Low palaeoproductivity in the Telychian on the Polish margin, suggests either that nutrient delivery rates to this margin were low, and/or nutrient remineralisation was limited, to produce a starved ocean in the sense of Berger et al. (1989). These factors may be most simply explained by low fluvial input (low nutrient input), coupled with a terrestrially more arid interval during the Telychian on the EEC. Greater aridity is supported by an increased Fe-delivery (with larger MS) to the EEC margin, probably through an increased deflation of soils, hence the increase in weathering indices in the Phase-I interval (Fig. 8). The mechanism by which these sediment sources were likely delivered to the EEC margin was an increased aeolian input. If aeolian-sourced dust was similar to modern low latitude deserts such as the Sahara, the supply of dust may have been decoupled from high latitude glacials, but responded inversely to monsoon intensity and riverine outflow (Skonieczny et al. 2019). From the Telychian of core A/B in northern Poland (Fig. 1) Gambacorta et al. (2018) have proposed a similar Milankovitch-scale, monsoon-like control on high-frequency variations in degree of anoxia, inferred to be a response to nutrient supply.

Conclusions

- 1) Marine red beds in the European Llandovery are largely concentrated in the Telychian between in the Te1 stage slice to around the Te4/Te5 boundary. Where well-dated, there is no detailed synchronicity between red beds occurrence, probably due to local redox-controls on their stratigraphic distribution.
- 2) Based on geochemical and magnetic data from Polish cores, the Telychian oxygenation event can also be detected on the Polish margin of the EEC. This is seen as an enhanced Fe₂O₃ content and expressed in an increased MS, which shows subdivision into three MS peaks. The MS increases are linked to enhanced weathering of sediment sources, and changes in sediment provenance.
- 3) The increase in MS in the Telychian in Poland is due to both paramagnetic Fe-silicates, enhanced by greater preservation of low Ti magnetite and haematite in the suboxic interval. Based on relationship to geochemistry these detrital oxides are associated with heavy minerals and resistate elements.
- 4) A similar oxygenated interval is seen in the Re3 stage slice in Polish and Latvian-Estonian cores, but is only weakly expressed in an enhanced MS, likely due to a differing clastic provenance. A similar oxygenation event may occur around the Ae2/Ae3 slice boundary which needs further study.
- 5) Geochemical palaeoproductivity indices suggest the Telychian oxygenation event is associated with a reduction in primary palaeoproductivity, interpreted as a response to greater aridity on the EEC, linked to reduced nutrient input to the Polish margin, but enhanced aeolian inputs from Fe-enriched soils.

- 6) The timing of eustatic highstands, with respect to the beginning of oxygenated intervals and red beds in the Llandovery may have only a secondary, longer-term control on the oxygenation and red bed events.

Acknowledgements

Marion Grundy, James Griffiths, Luke Morgan for fieldwork help in collecting and processing some of the portable XRF. Adrian Muxworthy for hysteresis measurements. Additional magnetic measurements and sample processing by Victoria Lucas, David Mindham, Vassil Karloukovski and Alice Gent. Sebastian Baranowski (Ministerstwo Środowiska) for access to the Tłuszcz IG-1 core material. This work was funded by Chevron. David Loydell and Thomas Algeo provided constructive comments.

References

- Aldridge, R.J., Siveter, D. J., Lane, P.D., Palmer, D., Woodcock, N.H. 2000. British Silurian Stratigraphy. Geological Conservation Review Series, No. 19, Joint Nature Conservation Committee, Peterborough, 542 pp.
- Aldridge, R.J., Bassett, M.G., Clarkson, E.N.K., Downie, C., Holland, C.H., Lane, P.D., Rickards, R.B., Scrutton, C.T., Taylor, C., 2002. Telychian rocks in the British Isles. In: Holland, C.H., Bassett, M.G. (Eds.), Telychian Rocks of the British Isles and China (Silurian, Llandovery Series): An Experiment to Test Precision in Stratigraphy. National Museums & Galleries of Wales, Cardiff, Geological Series, 21, 43–72.
- Algeo, T. J., 2004. Can marine anoxic events draw down the trace element inventory of seawater?. *Geology*, 32, 1057-1060.
- Algeo, T. J., Ingall, E., 2007. Sedimentary Corg: P ratios, paleocean ventilation, and Phanerozoic atmospheric pO₂. *Palaeogeography, Palaeoclimatology, Palaeoecology*, 256, 130-155.
- Algeo, T. J., Tribovillard, N., 2009. Environmental analysis of paleoceanographic systems based on molybdenum–uranium covariation. *Chemical Geology* 268, 211-225.
- Algeo, T. J., Li, C. 2020. Redox classification and calibration of redox thresholds in sedimentary systems. *Geochimica et Cosmochimica Acta* 287, 8-26.
- Areń, B. 1967. Paleozoik obniżenia podlaskiego. *Geological Quarterly* 11, 529-546.
- Areń, B., 1972. Rozwój paleozoiku w obniżeniu podlaskim. *Geological Quarterly* 16, 19-36.
- Baarli, B. G. 1990a. Depositional environments in the Telychian Stage (Silurian) of the central Oslo region, Norway. *Geological Journal* 25, 65-79.
- Baarli, B. G., 1990b. Peripheral bulge of a foreland basin in the Oslo Region during the Early Silurian. *Palaeogeography, Palaeoclimatology, Palaeoecology* 78, 149-161.
- Bábek, O., Faměra, M., Hladil, J., Kapusta, J., Weinerová, H., Šimíček, D., Slavík, L. and Ďurišová, J., 2018. Origin of red pelagic carbonates as an interplay of global climate and local basin factors: Insight from the Lower Devonian of the Prague Basin, Czech Republic. *Sedimentary Geology*, 364, 71-88.

- Barron, H. F., 1998. The geology of the central Pentland Hills: 1: 10000 sheets NT16SE (Scald Law) and 1: 10560 sheets NT15NW (Baddinsgill) and part of NT15NE (Carlops): part of 1: 50000 sheets 32W (Livingston), 32E (Edinburgh) and 24W (Biggar). British Geological Survey, Technical Report WA/98/41.
- Bassett, M. G., Bluck, B. J., Cave, R., Holland, C. H., Lawson, J. D., 1992. Silurian. In: J. C. W. Cope, J. K. Ingham and P. F. Rawson (eds.). Atlas of Palaeogeography and Lithofacies. Geological Society, London, Memoirs 13, pp. 17-56.
- Bassett, M.G. Chen, X., Rong, H-Y., Geng-Liang, Y., Rickards, R.B. Scrutton C.T., Holland, C.H. 2002. Marine red sediments. In: Holland, C. H., Bassett, M. G. (Eds.). Telychian Rocks of the British Isles and China (Silurian, Llandovery Series: An Experiment to Test Precision in Stratigraphy). National Museum of Wales Geological Series, 21, pp. 150-156.
- Beaulieu, E., Godd ris, Y., Donnadieu, Y., Labat, D., Roelandt, C., 2012. High sensitivity of the continental-weathering carbon dioxide sink to future climate change, Nat. Clim. Change 2, 346–349.
- Bennett, W. W., Canfield, D. E., 2020. Redox-sensitive trace metals as paleoredox proxies: A review and analysis of data from modern sediments. Earth-Science Reviews 204, doi.org/10.1016/j.earscirev.2020.103175
- Benton, M. J., Gray, D. I., 1981. Lower Silurian distal shelf storm-induced turbidites in the Welsh Borders: sediments, tool marks and trace fossils. Journal of the Geological Society 138, 675-694.
- Berger, W.H., Smetacek, V.S., Wefer, G., 1989. Ocean productivity and paleoproductivity - an overview. In: Berger, W.H., Smetacek, G. (eds.) Productivity of the ocean: present and past, pp. 1-34. John Wiley & Sons, New York.
- Bloemendal, J., King, J. W., Hall, F. R., Doh, S. J., 1992. Rock magnetism of Late Neogene and Pleistocene deep-sea sediments: Relationship to sediment source, diagenetic processes, and sediment lithology. Journal of Geophysical Research: Solid Earth 97, 4361-4375.
- Brenchley, P. J., Carden, G. A., Hints, L., Kaljo, D., Marshall, J. D., Martma, T., Medla, Y., N lvak, J., 2003. High-resolution stable isotope stratigraphy of Upper Ordovician sequences: Constraints on the timing of bioevents and environmental changes associated with mass extinction and glaciation. Geological Society of America Bulletin 115, 89-104.
- Bridges, P. H., 1975. The transgression of a hard substrate shelf: the Llandovery (Lower Silurian) of the Welsh Borderland. Journal of Sedimentary Research 45, 79-94.
- Bull, E.E., Loydell, D.K. 1995. Uppermost Telychian graptolites from the North Esk Inlier, Pentland Hills, near Edinburgh. Scottish Journal of Geology, 31, 163-170.

- Calner, M., Ahlberg, P., Lehnert, O., Erlström, M., 2013 (eds). The Lower Palaeozoic of southern Sweden and the Oslo Region, Norway. Field Guide for the 3rd Annual Meeting of IGCP project 591, p. 96.
- Canfield, D.E., Raiswell, R., Bottrell, S.H., 1992. The reactivity of sedimentary iron minerals toward sulfide. *American Journal Sci.* 292, 659–683.
- Cave, R., Dixon, R. J. 1993. The Ordovician and Silurian of the Welshpool area. In Woodcock N. H., Bassett, M. G. *Geological excursions in Powys*, pp. 51–84. Cardiff, Wales: National Museum of Wales Press.
- Chavez, F. P., Messié, M., Pennington, J. T., 2010. Marine primary production in relation to climate variability and change. *Annual Review of Marine Science* 3, 227-260.
- Cherns, L., Cocks, L. R. M., Davies, J. R., Hillier, R. D., Waters, R. A., Williams, M., 2006. Silurian: the influence of extensional tectonics and sea-level changes on sedimentation in the Welsh Basin and on the Midland Platform. In: Brenchley, P.J. Rawson, P.F. (Eds). *The Geology of England and Wales*, 2nd edition, Geological Society, pp. 75-102.
- Chung, F.H., 1974. Quantitative Interpretation of X-ray Diffraction Patterns of Mixtures. I. Matrix-Flushing Method for Quantitative Multicomponent Analysis. *J. Appl. Cryst.* 7, 519-525.
- Cocks, L.R.M., Rickards, R.B., 1968. Five boreholes in Shropshire and the relationships of shelly and graptolitic facies in the Lower Silurian. *Quarterly Journal of the Geological Society*, 124, 213-238.
- Condie, K.C., 1993. Chemical composition and evolution of the upper continental crust: contrasting results from surface samples and shales. *Chemical Geology* 104, 1-37.
- Cooper, R. A., Sadler, P. M., Hammer, O., Gradstein, F. M., 2012. The Ordovician Period. In: Gradstein, F.M., Ogg, J.G., Schmitz, M.D., Ogg, G.M. *The Geologic Time Scale*, pp. 489-523, Elsevier.
- Cramer, B.D., Loydell, D.K., Samtleben, C., Munnecke, A., Kaljo, D., Männik, P., Martma, T., Jeppsson, L., Kleffner, M.A., Barrick, J.E., Johnson, C.A., 2010. Testing the limits of Paleozoic chronostratigraphic correlation via high-resolution (< 500 ky) integrated conodont, graptolite, and carbon isotope ($\delta^{13}\text{C}_{\text{carb}}$) biochemostratigraphy across the Llandovery–Wenlock (Silurian) boundary: Is a unified Phanerozoic time scale achievable? *GSA Bulletin* 122, 1700-1716.
- Cramer, B.D., Brett, C.E., Melchin, M.J., Männik, P., Kleffner, M.A., McLaughlin, P.I., Loydell, D.K., Munnecke, A., Jeppsson, L., Corradini, C., Brunton, F.R., 2011. Revised correlation of Silurian Provincial Series of North America with global and regional chronostratigraphic units and $\delta^{13}\text{C}_{\text{carb}}$ chemostratigraphy. *Lethaia* 44, 185–202.

- Cramer, B.D., Condon, D.J., Söderlund, U., Marshall, C., Worton, G.J., Thomas, A.T., Calner, M., Ray, D.C., Perrier, V., Boomer, I., Patchett, P.J., 2012. U-Pb (zircon) age constraints on the timing and duration of Wenlock (Silurian) paleocommunity collapse and recovery during the “Big Crisis”. *GSA Bulletin* 124, 1841-1857.
- Cullers, R.L., Barrett, T., Carlson, R., Robinson, B., 1987. Rare-earth element and mineralogic changes in Holocene soil and stream sediment: a case study in the Wet Mountains, Colorado, USA. *Chemical Geology* 63, 275-297.
- Dadlez, R., Areń, B., Marek, S. (Eds.). 1974. Tłuszcz IG-1. Profile głębokich otworów wiertniczych Instytutu Geologicznego, 13.
- Da Silva, A.C., Mabilie, C., Boulvain, F., 2009. Influence of sedimentary setting on the use of magnetic susceptibility: examples from the Devonian of Belgium. *Sedimentology*, 56, 1292-1306.
- Da Silva, A. C., De Vleeschouwer, D., Boulvain, F., Claeys, P., Fagel, N., Humblet, M., Mabilie, C., Michel, J., Sardar Abadi, M., Pas, D., Dekkers, M. J., 2013. Magnetic susceptibility as a high-resolution correlation tool and as a climatic proxy in Paleozoic rocks—Merits and pitfalls: Examples from the Devonian in Belgium. *Marine and Petroleum Geology* 46, 173-189.
- Da Silva, A. C., Whalen, M. T., Hladil, J., Chadimova, L., Chen, D., Spassov, S., Boulvain, F., Devleeschouwer, X., 2015. Magnetic Susceptibility Application: A Window onto Ancient Environments and Climatic Variations: Foreword. In: Da Silva, A. C., Whalen, M. T., Hladil, J., Chadimova, L., Chen, D., Spassov, S., Boulvain, F., Devleeschouwer, X. (Eds). *Magnetic Susceptibility Application: A Window onto Ancient Environments and Climatic Variations*. Geological Society, London, Special Publications 414, 1-13.
- Davies, J.R., Waters, R.A., Molyneux, S.G., Williams, M., Zalasiewicz, J.A., Vandembroucke, T.R., 2016. Gauging the impact of glacioeustasy on a mid-latitude Early Silurian basin margin, mid Wales, UK. *Earth-Science Reviews* 156, 82-107.
- Domeier, M., 2016. A plate tectonic scenario for the Iapetus and Rheic oceans. *Gondwana Research* 36, 275-295.
- Doyle, E.N., Harper, D.A.T., Parkes, M.A., 1990. The Tonalee fauna: a deep-water shelly assemblage from the Llandovery rocks of the west of Ireland. *Irish Journal of Earth Sciences* 10, 129-143.
- Driese, S. G., Mora, C. I., Cotter, E., Foreman, J. L., 1992. Paleopedology and stable isotope chemistry of Late Silurian vertic Paleosols, Bloomsburg Formation, central Pennsylvania. *Journal of Sedimentary Research* 62, 825-841.
- Dupré, B., Gaillardet, J., Rousseau, D., Allègre, C.J., 1996. Major and trace elements of river-borne material: the Congo Basin. *Geochimica et Cosmochimica Acta* 60, 1301-1321.

- Ellwood, B. B., Crick, R. E., Benoist, S. L., Young, S. A., 2000. Magnetosusceptibility event and cyclostratigraphy method applied to marine rocks: detrital input versus carbonate productivity. *Geology* 28, 1135–1138.
- English, L.T.P. 1999. The use of magnetic susceptibility and trace element geochemistry for the correlation of fine-grained siliciclastic sequences: a Late Llandovery example from northwest England. *Geological Magazine* 136, 423–436.
- Fabian, K., 2003. Some additional parameters to estimate domain state from isothermal magnetization measurements. *Earth and Planetary Science Letters* 213, 337-345.
- Fearnside, W. G., Elles, G. L., Smith, B., 1906. The Lower Palaeozoic rocks of Pomeroy. *Proceedings of the Royal Irish Academy. Section B: Biological, Geological, and Chemical Science* 26, 97-128.
- Fedo, C.M., Nesbitt, W. H., Young, G.M., 1995. Unraveling the effects of potassium metasomatism in sedimentary rocks and paleosols, with implications for paleoweathering conditions and provenance. *Geology*, 23, 921-924.
- Ferraro, M.B., Giordani, P., Serafini, A., 2019. fclust: An R Package for Fuzzy Clustering. *The R Journal*, 11, 1-18. <https://journal.r-project.org/archive/2019/RJ-2019-017/RJ-2019-017.pdf>
- Floyd, J. D., Williams, M., 2002. A revised correlation of Silurian rocks in the Girvan district, SW Scotland. *Earth and Environmental Science Transactions of the Royal Society of Edinburgh* 93, 383-392.
- Floyd, P.A., Winchester, J.A., 1978. Identification and discrimination of altered and metamorphosed volcanic rocks using immobile elements. *Chemical Geology* 21, 291-306.
- Fralick, P.W., Kronberg, B.I., 1997. Geochemical discrimination of clastic sedimentary rock sources. *Sedimentary Geology* 113, 111-124.
- Frank, U., Nowaczyk, N.R., 2008. Mineral magnetic properties of artificial samples systematically mixed from haematite and magnetite. *Geophysical Journal International* 175, 449-461.
- Frost, B.R., Frost, C.D., 2008. A geochemical classification for feldspathic igneous rocks. *Journal of Petrology* 49, 1955-1969.
- Frost, B.R., Barnes, C.G., Collins, W.J., Arculus, R.J., Ellis, D.J., Frost, C.D., 2001. A geochemical classification for granitic rocks. *Journal of Petrology* 42, 2033-2048.
- Gabriel, K.R., Odoroff, C.L., 1990. Biplots in biomedical research. *Statistics in Medicine* 9, 469-485.
- Gambacorta, G., Menichetti, E., Trincianti, E., Torricelli, S., 2019. The Silurian climatic transition recorded in the epicontinental Baltica Sea. *Palaeogeography, Palaeoclimatology, Palaeoecology* 517, 16-29.

- Gambacorta, G., Menichetti, E., Trincianti, E., Torricelli, S., 2018. Orbital control on cyclical primary productivity and benthic anoxia: Astronomical tuning of the Telychian Stage (early Silurian). *Palaeogeography, Palaeoclimatology, Palaeoecology*, 495, 152-162.
- Garcia, D., Fonteilles, M., Moutte, J., 1994. Sedimentary fractionations between Al, Ti, and Zr and the genesis of strongly peraluminous granites. *The Journal of Geology* 102, 411-422.
- Gorjan, P., Kaiho, K., Fike, D.A., Xu, C., 2012. Carbon-and sulfur-isotope geochemistry of the Hirnantian (Late Ordovician) Wangjiawan (Riverside) section, South China: Global correlation and environmental event interpretation. *Palaeogeography, Palaeoclimatology, Palaeoecology* 337, 14-22.
- Grahn, Y., 1995. Lower Silurian chitinozoa and biostratigraphy of subsurface Gotland. *GFF* 117, 57–65.
- Habryn, R., Krzemińska, E., Krzemiński, L., Markowiak, M., Zieliński, G., 2020. Detrital zircon age data from the conglomerates in the Upper Silesian and Małopolska blocks, and their implications for the pre-Variscan tectonic evolution (S Poland). *Geological Quarterly* 64, 321-341.
- Haslett, J., Parnell, A., 2008. A simple monotone process with application to radiocarbon-dated depth chronologies. *Journal of the Royal Statistical Society: Series C (Applied Statistics)* 57, 399-418.
- Haq, B.U., Schutter, S.R., 2008. A chronology of Paleozoic sea-level changes. *Science*, 322, 64-68.
- Hebbali, A., 2018. *olsrr: Tools for Building OLS Regression Models*. R package version 0.5. <https://CRAN.R-project.org/package=olsrr>.
- Heinze, G., Wallisch, C., Dunkler, D., 2018. Variable selection—a review and recommendations for the practicing statistician. *Biometrical Journal* 60, 431-449.
- Hill, I.G., Worden, R.H., Meighan, I.G., 2000. Yttrium: the immobility-mobility transition during basaltic weathering. *Geology* 28, 923-926.
- Hillier, R. D., 2002. Depositional environment and sequence architecture of the Silurian Coralliferous Group, Southern Pembrokeshire, UK. *Geological Journal* 37, 247-268.
- Hounslow, M.W., 1996. Ferrimagnetic Cr and Mn spinels in sediments: residual magnetic minerals after diagenetic dissolution. *Geophysical research letters* 23, 2823-2826.
- Hounslow, M. W., Maher, B. A., 1999. Source of the climate signal recorded by magnetic susceptibility variations in Indian Ocean sediments. *Journal of Geophysical Research: Solid Earth* 104, 5047-5061.
- Hounslow, M.W., Morton, A.C., 2004. Evaluation of sediment provenance using magnetic mineral inclusions in clastic silicates: comparison with heavy mineral analysis. *Sedimentary Geology* 171, 13-36.

- Hounslow, M.W., Harris, S., Wojcik, K., Nawrocki, J., Ratcliffe, K.T., Woodcock, N.H., Channell, J.E.T., Montgomery, P., 2021a. Geomagnetic polarity during the Middle and Upper Ordovician. *Palaeogeography, Palaeoclimatology, Palaeoecology*. doi.org/10.1016/j.palaeo.2021.110225.
- Hounslow, M.W. Harris, S., Wójcik, K. Nawrocki, J., Woodcock, N.H., Channell, J.E.T., Ratcliffe, K., Montgomery, P. 2021b. Geomagnetic polarity during the early Silurian. The first magnetostratigraphy of the Llandovery. *Palaeogeography, Palaeoclimatology, Palaeoecology*. doi.org/10.1016/j.palaeo.2021.110245.
- Hu, X., Scott, R.W., Cai, Y., Wang, C., Melinte-Dobrinescu, M.C., 2012. Cretaceous oceanic red beds (CORBs): Different time scales and models of origin. *Earth-Science Reviews* 115, 217-248.
- Jarochowska, E., Munnecke, A., 2015. Late Wenlock carbon isotope excursions and associated conodont fauna in the Podlasie Depression, eastern Poland: a not-so-big crisis? *Geol. Journal* 51, 683–703.
- Jaworowski, K, Sikorska M, 2006. Łysogóry Unit (Central Poland) versus East European Craton—application of sedimentological data from Cambrian siliciclastic association. *Geol. Quarterly* 50, 77–88.
- Jarochowska, E., Munnecke, A., Frisch, K., Ray, D.C., Castagner, A., 2016. Faunal and facies changes through the mid Homerian (late Wenlock, Silurian) positive carbon isotope excursion in Podolia, western Ukraine. *Lethaia* 49,170-198.
- Jayawardena, U. De. S., Izawa, E., 1994. A new chemical index of weathering for metamorphic silicate rocks in tropical regions: a study from Sri Lanka. *Engineering Geology* 36, 303-310.
- Jeppsson, L., 1990. An oceanic model for lithological and faunal changes tested on the Silurian record. *Journal of the Geological Society* 147, 663-674.
- Johnson, M. E., 2010. Tracking Silurian eustasy: Alignment of empirical evidence or pursuit of deductive reasoning? *Palaeogeography, Palaeoclimatology, Palaeoecology* 296, 276-284.
- Kasten, S., Zabel, M., Heuer, V., Hensen, C., 2003. Processes and signals of nonsteady-state diagenesis in deep-sea sediments and their pore waters. In: Wefer G (Ed.), *The South Atlantic in the Late Quaternary* Springer, Berlin, Heidelberg, pp. 431-459
- Kemp, A. E., 1986. Tectonostratigraphy of the Southern Belt of the Southern Uplands. *Scottish Journal of Geology* 22, 241-256.
- Kiipli, E., 2004. Redox changes in the deep shelf of East Baltic Basin in Aeronian and early Telychian (Early Silurian). *Proc. Estonian Acad. Sci. Geol.* 53, 94-124.
- Kiipli E, Kallaste T, Kiipli T., 2000a. Hematite and goethite in Telychian marine red beds of the East Baltica. *GFF* 122, 281–286.

- Kiipli, E., Kiipli, T., Kallaste, T., 2000b. Early diagenetic chalcopyrite occurrences in Telychian marine red beds of West Estonia and West Latvia. *Proceedings of the Estonian Academy of Sciences, Geology* 49, 294-307.
- Kiipli, E., Kiipli, T., Kallaste, T., 2004. Bioproductivity rise in the East Baltic epicontinental sea in the Aeronian (Early Silurian). *Palaeogeography, Palaeoclimatology, Palaeoecology* 205, 255-272.
- Kiipli, E., Kiipli, T., Kallaste, T., 2009. Reconstruction of currents in the Mid-Ordovician–Early Silurian central Baltic Basin using geochemical and mineralogical indicators. *Geology* 37, 271-274.
- Kiipli, T., Radzievičius, S., Kallaste, T., Kiipli, E., Siir, S., Soesoo, A., Voolma, M., 2012. The Geniai Tuff in the southern East Baltic area – a new correlation tool near the Aeronian/Telychian stage boundary, Llandovery, Silurian. *Bulletin of Geosciences* 87, 695–704.
- Koptíková, L., Bábek, O., Hladil, J., Kalvoda, J., Slavík, L., 2010. Stratigraphic significance and resolution of spectral reflectance logs in Lower Devonian carbonates of the Barrandian area, Czech Republic; a correlation with magnetic susceptibility and gamma-ray logs. *Sedimentary Geology* 225, 83-98.
- Kozłowski, W. 2008. Lithostratigraphy and regional significance of the Nowa Słupia Group (Upper Silurian) of the Łysogóry Region (Holy Cross Mountains, Central Poland). *Acta Geologica Polonica* 58, 43-74.
- Kozłowski W., Munnecke, A. 2010. Stable carbon isotope development and sea-level changes during the Late Ludlow (Silurian) of the Łysogóry region (Rzepin section, Holy Cross Mountains, Poland). *Facies* 56, 615–633
- Kozłowski, W., Sobień, K., 2012. Mid-Ludfordian coeval carbon isotope, natural gamma ray and magnetic susceptibility excursions in the Mielnik IG-1 borehole (Eastern Poland)—Dustiness as a possible link between global climate and the Silurian carbon isotope record. *Palaeogeography, Palaeoclimatology, Palaeoecology* 339, 74-97.
- Kozłowski, W., 2015. Eolian dust influx and massive whittings during the Kozłowski/Lau Event: carbonate hypersaturation as a possible driver of the mid-Ludfordian Carbon Isotope Excursion. *Bulletin of Geosciences* 90, 807–840.
- Kurtz, A. C., Derry, L. A., Chadwick, O. A., Alfano, M. J., 2000. Refractory element mobility in volcanic soils. *Geology* 28, 683-686.
- Larrasoaña, J. C., Roberts, A. P., Rohling, E. J., 2008. Magnetic susceptibility of eastern Mediterranean marine sediments as a proxy for Saharan dust supply? *Marine Geology* 254, 224-229.

- Lascu, I., Banerjee, S.K., Berquó, T.S., 2010. Quantifying the concentration of ferrimagnetic particles in sediments using rock magnetic methods. *Geochemistry, Geophysics, Geosystems*, 11, doi.org/10.1029/2010GC003182
- Laveuf, C., Cornu, S., 2009. A review on the potentiality of rare earth elements to trace pedogenetic processes. *Geoderma* 154, 1-12.
- Leonhardt, R., 2006. Analyzing rock magnetic measurements: The RockMagAnalyzer 1.0 software. *Computers & Geosciences* 32,1420-1431.
- Lis, P., Bohacs, K.M. 2012. Parasequences in mudstone strata: Core Warehouse Workshop. In: Polish Geological Institute, *Geoshale: Recent Advances in Geology of Fine-Grained Sediments*, 14–16 May 2012. Warsaw, Poland, pp. 237-251. www.geoshale.com.
- Liu, J., Chen, Z., Chen, M., Yan, W., Xiang, R., Tang, X., 2010. Magnetic susceptibility variations and provenance of surface sediments in the South China Sea. *Sedimentary Geology* 230, 77-85.
- Liu, J., Wang, Y., Zhang, X., Rong, J., 2016. Early Telychian (Silurian) marine siliciclastic red beds in the Eastern Yangtze Platform, South China: distribution pattern and controlling factors. *Canadian Journal of Earth Sciences* 53, 712-718.
- Loader, C., 1999. *Local regression and likelihood*, Springer, New York.
- Longhurst, A., Sathyendranath, S., Platt, T., Caverhill, C., 1995. An estimate of global primary production in the ocean from satellite radiometer data. *Journal of plankton Research* 17, 1245-1271.
- Løvlie, R., Van Veen, P., 1995. Magnetic susceptibility of a 180 m sediment core: reliability of incremental sampling and evidence for a relationship between susceptibility and gamma activity. In: Turner, P., Turner, A. (Eds), *Palaeomagnetic Applications in Hydrocarbon Exploration and Production*. Geological Society, London, Special Publications, 98, 259-266.
- Loydell, D.K., 1998. Early Silurian sea-level changes. *Geological Magazine*, 135, 447-471.
- Loydell, D.K. 2012. Graptolite biozone correlation charts. *Geological Magazine* 149, 124–132.
- Loydell, D.K., Cave, R., 1996. The Llandovery-Wenlock boundary and related stratigraphy in eastern mid-Wales with special reference to the Banwy River section. *Newsletters on Stratigraphy* 34, 39-64.
- Loydell, D.K., Männik, P., Nestor, V., 2003. Integrated biostratigraphy of the lower Silurian of the Aizpute-41 core, Latvia. *Geological Magazine* 140, 205-229.

- Maes, G., Rickards, R. B., Rombouts, L., Vandeveld, N. 1979. Silurian formations between Neuville-sous-Huy and Ombret: their correlation, age and structure. *Annales de la Société Géologique de Belgique* 101, 31–36.
- Marshall, C., Large, D.J., Heavens, N.G., 2016. Coal-derived rates of atmospheric dust deposition during the Permian. *Gondwana Research* 31, 20-29.
- Maynard, J.B., 1992. Chemistry of modern soils as a guide to interpreting Precambrian paleosols. *The Journal of Geology* 100, 279-289.
- McAdams, N.E., Cramer, B.D., Bancroft, A.M., Melchin, M.J., Devera, J.A., Day, J.E., 2019. Integrated $\delta^{13}\text{C}_{\text{carb}}$, conodont, and graptolite biochemostratigraphy of the Silurian from the Illinois Basin and stratigraphic revision of the Bainbridge Group. *GSA Bulletin*, 131, 335-352.
- McLennan, S.M., 1989. Rare earth elements in sedimentary rocks: influence of provenance and sedimentary processes. In: Lipin, B.R., McKay, G.A. (Eds) *Geochemistry and Mineralogy of Rare Earth Elements, Reviews in Mineralogy* 21, 169-200, doi.org/10.1515/9781501509032-010.
- McLennan, S.M., Taylor, S.R., 1991. Sedimentary rocks and crustal evolution: tectonic setting and secular trends. *The Journal of Geology* 99, 1-21.
- Melchin, M.J., Sadler, P.M., Cramer, B.D., 2012. The Silurian Period, In: Gradstein, F.M., Ogg, J.G., Schmitz, M.D., Ogg, G.M. *The geologic time scale*, Elsevier, pp. 525–558.
- Melchin, M.J., Mitchell, C.E., Holmden, C., Štorch, P., 2013. Environmental changes in the Late Ordovician–Early Silurian: Review and new insights from black shales and nitrogen isotopes. *GSA Bulletin* 125, 1635-1670.
- Meyer, K.M., Kump, L.R., Ridgwell, A., 2008. Biogeochemical controls on photic-zone euxinia during the end-Permian mass extinction. *Geology* 36, 747-750.
- Morad, S., 1988. Diagenesis of titaniferous minerals in Jurassic sandstones from the Norwegian Sea. *Sedimentary Geology*, 57, 17-40.
- Milliken, K.L., McCarty, D.K., Derkowski, A., 2018. Grain assemblages and diagenesis in the tarl-dominated Lower Silurian mudrock succession of the western margin of the east European Craton in Poland and Lithuania. *Sedimentary Geology* 374, 115-133.
- Milodowski, A.E., Zalasiewicz, J.A., 1991. Redistribution of rare earth elements during diagenesis of turbidite/hemipelagite mudrock sequences of Llandovery age from central Wales. In: Morton, A. C., Todd, S. P., Haughton, P. D. W. (Eds), *Developments in Sedimentary Provenance Studies. Geological Society Special Publication* 57, 101-124.
- Mullins, G.L., Loydell, D.K., 2002. Integrated lower Silurian chitinozoan and graptolite biostratigraphy of Buttington Brick Pit, Wales. *Geological Magazine* 139, 89-96.

- Munnecke, A., Männik, P., 2009. New biostratigraphic and chemostratigraphic data from the Chicotte Formation (Llandoverý, Anticosti Island, Laurentia) compared with the Viki core (Estonia, Baltica). *Estonian Journal of Earth Sciences* 58, 159-169.
- Nawrocki, J., Dunlap, J., Pecskey, Z., Krzemiński, L., Żylińska, A., Fanning, M., Kozłowski, W., Salwa, S., Szczepanik, Z., Trela, W., 2007. Late Neoproterozoic to Early Palaeozoic palaeogeography of the Holy Cross Mountains (Central Europe): an integrated approach. *Journal of the Geological Society* 164, 405-423.
- Nesbitt, H.W., Markovics, G., 1997. Weathering of granodioritic crust, long-term storage of elements in weathering profiles, and petrogenesis of siliciclastic sediments. *Geochimica et Cosmochimica Acta* 61, 1653-1670.
- Nesbitt, H., Young, G.M., 1982. Early Proterozoic climates and plate motions inferred from major element chemistry of lutites. *Nature*, 299, 715-717.
- Nesbitt, H.W., Young, G.M., 1996. Petrogenesis of sediments in the absence of chemical weathering: effects of abrasion and sorting on bulk composition and mineralogy. *Sedimentology* 43, 341-358.
- Nielsen, A.T., Schovsbo, N.H., 2011: The Lower Cambrian of Scandinavia: depositional environment, sequence stratigraphy and palaeogeography. *Earth-Science Reviews* 107, 207–310.
- Niezabitowska, D.K., Szaniawski, R., Roszkowska-Remin, J., Gąsiński, A., 2019a. Magnetic Anisotropy in Silurian Gas-Bearing Shale Rocks From the Pomerania Region (Northern Poland). *Journal of Geophysical Research: Solid Earth* 124, 5-25.
- Niezabitowska, D.K., Szaniawski, R., Jackson, M., 2019b. Magnetic mineral assemblage as a potential indicator of depositional environment in gas-bearing Silurian shales from Northern Poland. *Geophysical Journal International*, 218, 1442-1455.
- Nowaczyk, N.R., 2011. Dissolution of titanomagnetite and sulphidization in sediments from Lake Kinneret, Israel. *Geophysical Journal International* 187, 34-44.
- Nyhuis, C. J., Riley, D., Kalasinska, A., 2016. Thin section petrography and chemostratigraphy: Integrated evaluation of an upper Mississippian mudstone dominated succession from the southern Netherlands. *Netherlands Journal of Geosciences* 95, 3-22.
- Ohta, T., Arai, H., 2007. Statistical empirical index of chemical weathering in igneous rocks: A new tool for evaluating the degree of weathering. *Chemical Geology* 240, 280-297.
- Panahi, A., Young, G.M., Rainbird, R.H., 2000. Behavior of major and trace elements (including REE) during Paleoproterozoic pedogenesis and diagenetic alteration of an Archean granite near Ville Marie, Quebec, Canada. *Geochimica et Cosmochimica Acta* 64, 2199-2220.

- Parkes, M.A., Palmer, D.C., 1994. The stratigraphy and palaeontology of the Lower Palaeozoic Kildare Inlier, County Kildare. *Irish Journal of Earth Sciences* 13, 65-81.
- Parker, A., 1970. An index of weathering for silicate rocks. *Geological Magazine*, 107, 501-504.
- Parnell, A.C., Haslett, J., Allen, J.R., Buck, C.E., Huntley, B., 2008. A flexible approach to assessing synchronicity of past events using Bayesian reconstructions of sedimentation history. *Quaternary Science Reviews* 27, 1872-1885.
- Paszkowski, M., Budzyń, B., Mazur, S., Sláma, J., Shumlyansky, L., Środoń, J., Dhuime, B., Kędzior, A., Liivamägi, S., Piszczowska, A., 2019. Detrital zircon U-Pb and Hf constraints on provenance and timing of deposition of the Mesoproterozoic to Cambrian sedimentary cover of the East European Craton, Belarus. *Precambrian Research* 331, doi.org/10.1016/j.precamres.2019.105352.
- Pedersen, T.F., Vogel, J.S., Southon, J.R., 1986. Copper and manganese in hemipelagic sediments: diagenetic contrasts. *Geochim. Cosmochim. Acta* 50, 2019–2031.
- Pe-Piper, G., Piper, D. J., Dolansky, L., 2005. Alteration of ilmenite in the Cretaceous sandstones of Nova Scotia, southeastern Canada. *Clays and Clay Minerals* 53, 490-510.
- Pe-Piper, G., Triantafyllidis, S., Piper, D.J., 2008. Geochemical identification of clastic sediment provenance from known sources of similar geology: the Cretaceous Scotian Basin, Canada. *Journal of Sedimentary Research* 78, 595-607.
- Peters, C., Dekkers, M.J., 2003. Selected room temperature magnetic parameters as a function of mineralogy, concentration and grain size. *Physics and Chemistry of the Earth, Parts A/B/C* 28, 659-667.
- Podhalańska, T., 2019. Graptolite biostratigraphy and dating of the Ordovician–Silurian shale succession of the SW slope of the East European Craton. *Annales Societatis Geologorum Poloniae* 89, 429-452.
- Pohl, A., Donnadieu, Y., Le Hir, G., Ferreira, D., 2017. The climatic significance of Late Ordovician-Early Silurian black shales. *Paleoceanography* 32, 397-423.
- Poprawa, P., 2019. Geological setting and Ediacaran–Palaeozoic evolution of the western slope of the East European Craton and adjacent regions. *Annales Societatis Geologorum Poloniae* 89, 347-380.
- Poprawa, P., Radkovets, N., Rauball, J., 2018. Ediacaran–Paleozoic subsidence history of the Volyn-Podillya-Moldova basin (Western and SW Ukraine, Moldova, NE Romania). *Geological Quarterly* 62, 459–486.
- Poprawa, P., Krzemińska, E., Paczeńska, J., Amstrong, R., 2020. Geochronology of the Volyn volcanic complex at the western slope of the East European Craton—relevance to the

- Neoproterozoic rifting and the break-up of Rodinia/Pannotia. *Precambrian Research* 346, doi.org/10.1016/j.precamres.2020.105817.
- Porębski, S. J., Prugar, W., Zacharski, J., 2013. Silurian shales of the East European Platform in Poland- some exploration problems. *Przegląd Geologiczny* 61, 630-638.
- Potter, D. K., Corbett, P. W., Barclay, S. A., Haszeldine, R. S., 2004. Quantification of illite content in sedimentary rocks using magnetic susceptibility—A rapid complement or alternative to X-ray diffraction. *Journal of Sedimentary Research* 74, 730-735.
- Poulton, S.W., Krom, M.D., Raiswell, R., 2004. A revised scheme for the reactivity of iron (oxyhydroxide) minerals towards dissolved sulfide. *Geochimica et Cosmochimica Acta* 68, 3703-3715.
- Preetz, H., Igel, J., Hannam, J.A., Stadler, S., 2017. Relationship between magnetic properties and reddening of tropical soils as indicators of weathering. *Geoderma* 303, 143-149.
- Price, J.R., Velbel, M.A., 2003. Chemical weathering indices applied to weathering profiles developed on heterogeneous felsic metamorphic parent rocks. *Chemical Geology* 202, 397-416.
- Puetz, S.J., Condie, K.C., 2020. Applying Popperian falsifiability to geodynamic hypotheses: empirical testing of the episodic crustal/zircon production hypothesis and selective preservation hypothesis. *International Geology Review*. doi.org/10.1080/00206814.2020.1818143.
- R Core Team, 2020. R: A language and environment for statistical computing. R Foundation for Statistical Computing, Vienna, Austria. <https://www.R-project.org/>.
- Radzevičius, S., 2013. Silurian graptolite biozones of Lithuania: present and perspectives. *Geologija*, 55, 41-49.
- Randive, K., Kumar, J. V., Bhondwe, A., Lanjewar, S., 2014. Understanding the behaviour of rare earth elements in minerals and rocks. *Gondwana Geological Magazine* 29, 173-181.
- Retallack, G.J., Sheldon, N.D., Cogoini, M., Elmore, R.D., 2003. Magnetic susceptibility of early Paleozoic and Precambrian paleosols. *Palaeogeography, Palaeoclimatology Palaeoecology* 198, 373-380.
- Rickards, R.B., 1964. The graptolitic mudstone and associated facies in the Silurian strata of the Howgill Fells. *Geological Magazine* 101, 435–451.
- Rickards, R.B., 1973. On some highest Llandovery red beds and graptolite assemblages in Britain and Eire. *Geological Magazine* 110, 70–72.
- Rickards, R.B., 1976. The sequence of Silurian graptolite zones in the British Isles. *Geological Journal* 11,153-188.

- Rickards, R. B., Burns, V., Archer, J., 1973. The Silurian sequence at Balbriggan, Co. Dublin. *Proceedings of the Royal Irish Academy. Section B: Biological, Geological, and Chemical Science* 73, 303-316.
- Rickards, R.B., Woodcock, N.H., 2005. Stratigraphical revision of the Windermere Supergroup (Late Ordovician - Silurian) in the southern Howgill Fells, NW England. *Proceedings of the Yorkshire Geological Society* 55, 263–285.
- Riquier, L., Averbuch, O., Devleeschouwer, X., Tribovillard, N., 2010. Diagenetic versus detrital origin of the magnetic susceptibility variations in some carbonate Frasnian–Famennian boundary sections from Northern Africa and Western Europe: implications for paleoenvironmental reconstructions. *International Journal of Earth Sciences* 99, 57-73.
- Roberts, A.P., 2015. Magnetic mineral diagenesis. *Earth-Science Reviews* 151, 1-47.
- Roberts, A.P., Hu, P., Harrison, R.J., Heslop, D., Muxworthy, A.R., Oda, H., Sato, T., Tauxe, L., Zhao, X., 2019. Domain state diagnosis in rock magnetism: Evaluation of potential alternatives to the Day diagram. *Journal of Geophysical Research: Solid Earth* 124, 5286-5314.
- Robinson, S. G., Sahota, J. T., Oldfield, F., 2000. Early diagenesis in North Atlantic abyssal plain sediments characterized by rock-magnetic and geochemical indices. *Marine Geology* 163, 77-107.
- Rochette, P., 1987. Magnetic susceptibility of the rock matrix related to magnetic fabric studies. *Journal of Structural Geology* 9, 1015-1020.
- Rochette, P., 1988. Inverse magnetic fabric in carbonate-bearing rocks. *Earth and Planetary Science Letters* 90, 229-237.
- Rollinson, H. R., 1993. *Using geochemical data: evaluation. Presentation, Interpretation*, Routledge.
- Rong, J., Wang, Y., Zhang, X., 2012. Tracking shallow marine red beds through geological time as exemplified by the lower Telychian (Silurian) in the Upper Yangtze Region, South China. *Science China Earth Sciences* 55, 699-713.
- Rong J Y, Wang Y, Zhan R B, Fan J X, Huang B, Tang P, Li Y, Zhang X L, Wu R C, Wang G X, Wei X., 2019. Silurian integrative stratigraphy and timescale of China. *Science China Earth Sciences* 62, 89–111.
- Rosen, O.M., Abbyasov, A.A., Tipper, J.C., 2004. MINLITH—an experience-based algorithm for estimating the likely mineralogical compositions of sedimentary rocks from bulk chemical analyses. *Computers & geosciences*, 30, 647-661.
- Rudnick, R.I., Rao, S. 2013. 4.1 Composition of the Continental Crust. In: Turekian, K., Holland, H. (Eds). *Treatise on Geochemistry* 2nd Edition, Elsevier. [dx.doi.org/10.1016/B978-0-08-095975-7.00301-6](https://doi.org/10.1016/B978-0-08-095975-7.00301-6)

- Rust, B. R., 1965. The sedimentology and diagenesis of Silurian turbidites in south-east Wigtownshire, Scotland. *Scottish Journal of Geology* 1, 231-246.
- Scheidt, S., Egli, R., Frederichs, T., Hambach, U., Rolf, C., 2017. A mineral magnetic characterization of the Plio-Pleistocene fluvial infill of the Heidelberg Basin (Germany). *Geophysical Journal International* 210, 743-764.
- Schieber, J., 2016. Mud re-distribution in epicontinental basins—Exploring likely processes. *Marine and Petroleum Geology* 71, 119-133.
- Schmidt, V., Günther, D., Hirt, A.M., 2006. Magnetic anisotropy of calcite at room-temperature. *Tectonophysics* 418, 63-73.
- Schoepfer, S. D., Shen, J., Wei, H., Tyson, R. V., Ingall, E., Algeo, T. J., 2015. Total organic carbon, organic phosphorus, and biogenic barium fluxes as proxies for paleomarine productivity. *Earth-Science Reviews* 149, 23-52.
- Schovsbo, N. H., 2003. The geochemistry of Lower Palaeozoic sediments deposited on the margins of Baltica. *Bulletin of the Geological Society of Denmark* 50, 11-27.
- Scrutton, C.T., McCurry, J.A., 1987. The derivation, biostratigraphy and palaeobiogeographic significance of corals from Silurian deep-sea turbidite facies in the south-west Southern Uplands. *Scottish Journal of Geology* 23, 49-64.
- Shen, J., Schoepfer, S.D., Feng, Q., Zhou, L., Yu, J., Song, H., Wei, H., Algeo, T.J., 2015. Marine productivity changes during the end-Permian crisis and Early Triassic recovery. *Earth-Science Reviews* 149, 136-162.
- Skompski, S., Łuczyński, P., Drygant, D., Kozłowski, W., 2008. High-energy sedimentary events in lagoonal successions of the Upper Silurian of Podolia, Ukraine. *Facies*, 54, 277-296.
- Skonieczny C., McGee, D., Winckler, G., Bory, A., Bradtmiller, L. I., Kinsley, C. W., Polissar, P. J., De Pol-Holz, R., Rossignol, L., Malaizé, B. 2019. Monsoon-driven Saharan dust variability over the past 240,000 years. *Sci. Adv.* 5, eaav1887. DOI: 10.1126/sciadv.aav1887.
- Śliwiński, M.G., Whalen, M.T., Meyer, F.J., Majs, F., 2012. Constraining clastic input controls on magnetic susceptibility and trace element anomalies during the Late Devonian punctata Event in the Western Canada Sedimentary Basin. *Terra Nova*, 24, 301-309.
- Smolarek, J., Trela, W., Bond, D. P., Marynowski, L., 2017. Lower Wenlock black shales in the northern Holy Cross Mountains, Poland: sedimentary and geochemical controls on the Ireviken Event in a deep marine setting. *Geological Magazine* 154, 247-264.

- Soreghan, G. S., Heavens, N. G., Hinnov, L. A., Aciego, S. M., Simpson, C., 2015. Reconstructing the dust cycle in deep time: The case of the late Paleozoic icehouse. *The Paleontological Society Papers* 21, 83-120.
- Srodon, J., Drits, V.A., McCarty, D.K., Hsieh, J.C.C., Eberl, D.D., 2001. Quantitative X-ray diffraction analysis of clay-bearing rocks from random preparations. *Clays and Clay Minerals* 49, 514-528.
- Stockey, R.G., Cole, D.B., Planavsky, N.J., Loydell, D.K., Frýda, J., Sperling, E.A., 2020. Persistent global marine euxinia in the Early Silurian. *Nature Communications* 11, doi.org/10.1038/s41467-020-15400-y.
- Sullivan, N. B., Brett, C. E., 2013. Integrating magnetic susceptibility data with sequence stratigraphy in the ironstone bearing successions (Lower Silurian) of eastern North America. *Stratigraphy* 10, 261-280.
- Sullivan, N.B, Loydell, D.K, Montgomery, P., Molyneux, S.G., Zalasiewicz, J. Ratcliffe, K.T, Campbell, E., Griffiths, J.D., Lewis G., 2018. A record of Late Ordovician to Silurian oceanographic events on the margin of Baltica based on new carbon isotope data, elemental geochemistry, and biostratigraphy from two boreholes in central Poland. *Palaeogeography, Palaeoclimatology, Palaeoecology* 490, 95–106.
- Sweere, T., van den Boorn, S., Dickson, A.J., Reichart, G.J., 2016. Definition of new trace-metal proxies for the controls on organic matter enrichment in marine sediments based on Mn, Co, Mo and Cd concentrations. *Chemical Geology* 441, 235-245.
- Tauxe, L., Mullender, T.A.T., Pick, T., 1996. Potbellies, wasp-waists, and superparamagnetism in magnetic hysteresis. *Journal of Geophysical Research: Solid Earth* 101, 571-583.
- Tauxe, L., Bertram, H.N., Seberino, C., 2002. Physical interpretation of hysteresis loops: Micromagnetic modeling of fine particle magnetite. *Geochemistry, Geophysics, Geosystems* 3, 1-22. doi.org/10.1029/2001GC000241
- Taylor, S.R., McLennan, S.M., 1985. *The continental crust: its composition and evolution.* Blackwell Scientific Publications, Oxford.
- Teller, L., 1997. The subsurface Silurian in the East European platform. *Palaeontologia Polonica* 56, 7–21.
- Theiling, B. P., Elrick, M., Asmerom, Y., 2017. Constraining the timing and provenance of trans-Laurentian transport using Nd and Sm isotopes from Silurian and Devonian marine carbonates. *Palaeogeography, Palaeoclimatology, Palaeoecology* 466, 392-405.
- Thomson, J., Jarvis, I., Green, D.R., Green, D.A., Clayton, T., 1998a. Mobility and immobility of redox-sensitive elements in deep-sea turbidites during shallow burial. *Geochimica et Cosmochimica Acta* 62,643-656.

- Thomson, J., Jarvis, I., Green, D.R., Green, D., 1998b. Oxidation fronts in Madeira Abyssal Plain turbidites: persistence of early diagenetic trace-element enrichments during burial, site 950. In: Weaver, P.P.E., Schmincke, H.-U., Firth, J.V., Duffield, W. (Eds.), *Proceedings of the Ocean Drilling Program, Scientific Results 157*, 559-571
- Thomson, J., Mercone, D., De Lange, G.J., Van Santvoort, P.J.M., 1999. Review of recent advances in the interpretation of eastern Mediterranean sapropel S1 from geochemical evidence. *Marine Geology* 153, 77-89.
- Tischendorf, G., Förster, H. J., Gottesmann, B., 2001. Minor-and trace-element composition of trioctahedral micas: a review. *Mineralogical Magazine* 65, 249-276.
- Torrent, J., Barrón, V., Liu, Q., 2006. Magnetic enhancement is linked to and precedes hematite formation in aerobic soil. *Geophysical Research Letters* 33, doi.org/10.1029/2005GL024818.
- Torsvik, T.H., Cocks, L.R.M., 2013. New global palaeogeographical reconstructions for the Early Palaeozoic and their generation. *Geological Society, London, Memoirs* 38, 5-24.
- Trela, W., Podhalańska, T., Smolarek, J., Marynowski, L., 2016. Llandovery green/grey and black mudrock facies of the northern Holy Cross Mountains (Poland) and their relation to Early Silurian sea-level changes and benthic oxygen level. *Sedimentary Geology* 342, 66-77.
- Tribovillard, N., Algeo, T.J., Lyons, T., Riboulleau, A., 2006. Trace metals as paleoredox and paleoproductivity proxies: an update. *Chemical Geology* 232, 12-32.
- Trotter, J. A., I. S. Williams, C. R. Barnes, P. Männik, and A. Simpson, 2016. New conodont $\delta^{18}\text{O}$ records of Silurian climate change: Implications for environmental and biological events, *Palaeogeogr. Palaeoclimatol. Palaeoecol.* 443, 34–48.
- Turner, P., 1979. Diagenetic origin of Cambrian marine red beds: Caerfai Bay shales, Dyfed, Wales. *Sedimentary Geology* 24, 269-281.
- Tyson, R.V., Pearson, T.H., 1991. Modern and ancient continental shelf anoxia: an overview. In: Tyson, R. V., Pearson, T. H. (eds), *Modern and ancient continental shelf anoxia. Geological Society Special Publication*, 58,1-24.
- Valverde-Vaquero, P., Dörr, W., Belka, Z., Franke, W., Wiszniewska, J., Schastok, J., 2000. U–Pb single-grain dating of detrital zircon in the Cambrian of central Poland: implications for Gondwana versus Baltica provenance studies. *Earth and Planetary Science Letters* 184, 225-240.
- Van der Weijden, C.H., 2002. Pitfalls of normalization of marine geochemical data using a common divisor. *Marine Geology* 184, 167-187.
- Verniers, J., Herbosch, A., Vanguetaine, M., Geukens, F., Delcambre, B. Pingot, J.-L., Belanger, I., Hennebert, M., Debaker, T., Sintubin, M., De Vos, W., 2001. Cambrian-Ordovician-Silurian lithostratigraphic units (Belgium). In: Bultynck, P., Dejonghe, L.

- (Eds). Guide to a revised lithostratigraphic scale of Belgium. *Geologica Belgica* 4, 5-38.
- Verniers, J., Maletz, J., Kriz, J., Zigaite, Z., Paris, F., Schönlaub, H.P., Wrona, R., 2008. Silurian of Central Europe. In: McCann, T. (Ed.). *The Geology of Central Europe Vol 1- Precambrian and Palaeozoic*. Geological Society London, pp. 249-302
- Von Dobeneck, T., 1996. A systematic analysis of natural magnetic mineral assemblages based on modelling hysteresis loops with coercivity-related hyperbolic basis functions. *Geophysical Journal International*, 124, 675-694.
- Walden, J., Oldfield, F., Smith, J.P. (Eds.), 1999. *Environmental Magnetism: A Practical Guide*, Quaternary Research Association, Technical Guide, vol. 6. London.
- Wang, D., Van der Voo, R., 2004. The hysteresis properties of multidomain magnetite and titanomagnetite/titanomaghemite in mid-ocean ridge basalts. *Earth and Planetary Science Letters* 220, 175-184.
- Weibel, R., Friis, H., 2004. Opaque minerals as keys for distinguishing oxidising and reducing diagenetic conditions in the Lower Triassic Bunter Sandstone, North German Basin. *Sedimentary Geology* 169, 129-149.
- White, D. E., Barron, H. F., Barnes, R. P., Lintern, B. C., 1991. Biostratigraphy of late Llandovery (Telychian) and Wenlock turbiditic sequences in the SW Southern Uplands, Scotland. *Earth and Environmental Science Transactions of the Royal Society of Edinburgh* 82, 297-322.
- Wilson, D., Burt, C.E., Davies, J.R., Hall, M., Jones, N.S., Leslie, A.B., Lusty, P.A.J., Wilby, P.R., Aspden, J.A., 2016. *Geology of the Llanidloes district, Sheet 164*. British Geological Survey, HMSO.
- Winchester, J.A., Floyd, P.A., 1976. Geochemical magma type discrimination: application to altered and metamorphosed basic igneous rocks. *Earth and Planetary Science Letters* 28, 459-469.
- Winchester, J.A., Floyd, P.A., 1977. Geochemical discrimination of different magma series and their differentiation products using immobile elements. *Chemical Geology* 20, 325-343.
- Wood, E.M., 1906. The Tarannon Series of Tarannon. *Quarterly Journal of the Geological Society* 62, 644-701.
- Worsley, D., Aarhus, N., Bassetti, M. G., Howe, M. P. A., Mork, A., Olausson, S., 1983. The Silurian succession of the Oslo Region. *Norges Geologiske Undersøkelse* 384, 1-57.
- Worsley, D., Baarli, B.G., Howe, M.P.A., Hjaltason, F., Alm, D. 2011. New data on the Bruflat Formation and the Llandovery/Wenlock transition in the Oslo region, Norway. *Norwegian Journal of Geology* 91, 101-120.
- Xie, Y., Meng, J., Guo, L., 2014. REE geochemistry of modern eolian dust deposits in Harbin city, Heilongjiang province, China: Implications for provenance. *Catena* 123, 70-78.

- Young, S.A., Benayoun, E., Kozik, N.P., Hints, O., Martma, T., Bergström, S.M., Owens, J.D., 2020. Marine redox variability from Baltica during extinction events in the latest Ordovician–Early Silurian. *Palaeogeography, Palaeoclimatology, Palaeoecology* 554, doi.org/10.1016/j.palaeo.2020.109792.
- Zalasiewicz, J.A., Taylor, L., Rushton, A.W.A., Loydell, D.K., Rickards, R.B., Williams, M., 2009. Graptolites in British stratigraphy. *Geological Magazine* 146, 785-850.
- Żelaźniewicz, A., Oberc-Dziedzic, T., Slama, J., 2020. Baltica and the Cadomian orogen in the Ediacaran–Cambrian: a perspective from SE Poland. *International Journal of Earth Sciences* 109, 1503–1528.
- Zenkner, L. J., Kozłowski, W., 2017. Anomalous massive water-column carbonate precipitation (whittings) as another factor linking Silurian oceanic events. *GFF* 139, 184-194.
- Zhang, G.L., Pan, J.H., Huang, C.M., Gong, Z.T., 2007. Geochemical features of a soil chronosequence developed on basalt in Hainan Island, China. *Revista Mexicana de Ciencias Geológicas* 24, 261-269.
- Zhang, X.L., Liu, J., Wang, Y., Rong, J., Zhan, R., Xu, H., Tang, P., 2018. Onset of the middle Telychian (Silurian) clastic marine red beds on the western Yangtze Platform, South China. *Palaeogeography Palaeoclimatology Palaeoecology* 497, 52-65.
- Zhang, X.L., Wang, Y., Rong, J.Y., Li, R.Y., 2014b. Pigmentation of the Early Silurian shallow marine red beds in South China as exemplified by the Rongxi Formation of Xiushan, southeastern Chongqing, central China. *Palaeoworld* 23, 240-251.
- Zhang, Y., Pe-Piper, G., Piper, D.J., 2014a. Sediment geochemistry as a provenance indicator: Unravelling the cryptic signatures of polycyclic sources, climate change, tectonism and volcanism. *Sedimentology* 61, 383-410.
- Zhou, L., Wignall, P.B., Su, J., Feng, Q., Xie, S., Zhao, L., Huang, J., 2012. U/Mo ratios and $\delta^{98/95}\text{Mo}$ as local and global redox proxies during mass extinction events. *Chemical Geology*, 324, 99-107.
- Zhou, L., Algeo, T.J., Shen, J., Hu, Z., Gong, H., Xie, S., Huang, J., Gao, S., 2015. Changes in marine productivity and redox conditions during the Late Ordovician Hirnantian glaciation. *Palaeogeography Palaeoclimatology Palaeoecology* 420, 223-234.
- Ziegler, A.M., Mckerrow, W.S. 1975. Silurian marine red beds. *American Journal of Science* 275, 31–56.

Figure captions

Fig.1. Site locations on a simplified European Terrane map (based on Winchester et al. 2002). Black dots are sample sites, and black circles additional cores and sections mentioned in text.

Red bed locations from Table 1. Red bed distribution in Estonia-Latvia from Kiipli (2004). The A/B cores are those used by Gambacorta et al. (2018, 2019).

Fig. 2. Correlation of the Telychian magnetic susceptibility (MS) for the Polish cores and sections. Bardo Stawy data from Hounslow et al. (2021b). The stage slices of Cramer et al. (2011) and McAdams et al. (2019) are shown for the biochronology (slanting line, indicates uncertainty in biozone position). Carbon isotope data and interpretation of the lower Sheinwoodian carbon isotope excursion (ESCIE) from Sullivan et al. (2018). Ordovician chronostratigraphy for Zwierzyneic-1 and Grabowiec-6 from Hounslow et al. (2021a), Silurian from Sullivan et al. (2018). See the SI for a detailed graptolite biozonation of the Tłuszcz IG-1 core.

Fig. 3. K_{surf} with respect to the mineralogy based on X-ray diffraction (XRD) data from Grabowiec-6. a) K_{surf} and XRD derived calcite content, which is divided into two main fields (boundary marked grey), of low carbonate content and a high carbonate content (>20% calcite). The two largest MS values in the Ordovician indicate the Ordovician data relationships may be better represented by a calcite-dilution relationship (dashed blue line). b) K_{surf} versus calcite content based on the calcite transfer function, using the portable XRF data (see SI for details). c) and d) K_{surf} normalised with respect to the non-carbonate content (K_{scf}) plotted against XRD determined percentage chlorite in c) and against illite-smectite content in d). In c) and d) the region of samples with high carbonate content is indicated by the grey bounding line. In a, c, d) the Katian-Hirnantian data are from 3993.4- 3814.2 m depth in Grabowiec-6 (Fig. 2c).

Fig. 4. Hysteresis data for samples from Grabowiec-6. a) Percent paramagnetic proxies (using calcite-free values). b) The Fabian (2003) plot showing the relationship between the shape parameter (σ_{Hys}) and $B_{\text{th}}/B_{\text{cr}}$ ratio as proxies for the domain state of magnetite. A 'bag' is drawn around the bulk of those samples with %paramagnetic <50%. c) The multidomain (MD) part of the domain state diagram of Tauxe et al. (2002). Titanomagnetite (TM60) and low Ti-magnetite trends of Wang and Van der Voo (2004), along with the space between these lines representing the range expected for oxidized TM60 titanomagnetite. The hysteresis data of Niezabitowska et al. (2019) from the Wenlock from N. Poland are also shown. d) the domain state plot of Lascu et al. (2010) showing the MD mixing relationships with various types of single domain (SD) particles (locations for 10, 20 and 30% SD material shown). Range of $\chi_{\text{ARM}}/\text{SIRM}$ for magnetite inclusions in silicates from western European basement samples (excluding gneiss) from Hounslow and Morton (2004). Key above b) applies to a) to d). Those with %paramagnetic ($100 \times \chi_{\text{para}}/\chi_{\text{tot}}$) >50% flagged with a small tick.

Fig. 5. Rock magnetic data for all three Polish Cores. a) Saturation isothermal remanence (SIRM at 1T) versus the χ_{lf} illustrating the increase in ferromagnetic content with larger SIRM for those from the Telychian oxygenation event. Arrows on right show the mean and 2σ range of SIRM in inclusions in silicates from western European basement (from Hounslow and Morton 2004). b) Relationship of SIRM and s-ratio, with upper axis showing the %magnetite (in mass magnetite+haematite content) using the mixing relationships of

Frank and Nowaczyk (2008). $-IRM_{0.1T}$ is the backfield IRM at 0.1 T. c), d), e) Relationships of carbonate-free K_{surf} (K_{scf}) and Fe_2O_3 , TiO_2 and MnO in the portable XRF geochemical data for Zwierzyniec-1. c), d), e) use samples with estimated calcite contents less than 23% (i.e. data in Fig. 3b).

Fig. 6. Geochemical diagenetic zonation indicators for Zwierzyniec-1 using: a) those from Algeo and Tribovillard (2009), b, c) protocols proposed by Algeo and Li (2020a), and d) from Bennett and Canfield (2020). Enrichment factors (subscript EF) use the post-Archean average Australian shale (PAAS) normalisation values in Table 3 of Tribovillard et al. (2006). The Baltic Basin data in a) (red bag around data spread) and d) is from Gambacorta et al. (2019) covering a similar Silurian age interval as Zwierzyniec-1 (recalculated using same PAAS values). In d) The Mo/Al and U/Al boundary ‘adjustments’ (shown with arrows) are necessary to approximately change the modern seawater composition expressed in data of Bennett and Canfield (2020) to Silurian seawater. The purple, ‘not-present’ field marks an area in which data from modern sediments does not plot in. Uses the ICP OES-MS geochemical data from Sullivan et al. (2018).

Fig. 7. Summary of redox-related data for the Hirnantian to lower Homerian in Zwierzyniec-1, placed against the K_{surf} data in a). b) Estimated quartz and calcite+dolomite contents based on XRD to geochemistry transfer function for ICP-OES data (see SI for details); c), d), e) f) redox proxies discussed in the text. The three fields (within OMZ, euxinic or within OMZ and below OMZ) from the upper panel in Fig. 6d, calculated as V_{EF} , are shown as divisions in d). g), h) total rare earth elements (ΣREE) and Al_2O_3 normalisation of P_2O_5 . h) The oceanic state intervals as inferred from Fig. 6d. The Mo_{EF} , C_{org}/P and Zn_{EF} proxies have colour-filled intervals on the curves representing the oxic-suboxic intervals at threshold values of 1.25 ($Mo/AL = 0.15 \mu g g^{-1}$), 45, 1.0 respectively. That filled for Tl/Th uses the fully-oxic ocean intervals in h). Values for PAAS and upper continental crust (UCC; Rudnick and Gao 2013) indicated on columns. Uses the ICP OES-MS geochemical data from Sullivan et al. (2018). Blue horizontal lines are stage boundaries.

Fig. 8. A), b) Palaeo-weathering indices CIA (Nesbitt and Young 1982), STI (Jayawardena and Izawa 1994) and WIP (Price and Velbel 2003; Table 2). The STI and WIP indices have been reversed (as STI_R and WIP_R) to show values increasing for an increase in weathering like the CIA index. The fields for average Archean to middle Proterozoic igneous rock types, and PAAS are from Condie (1993). The average felsic-volcanic field plots off the STI_R axis in b), below the granites and TTG field. ICP-OES geochemical data from Sullivan et al. (2018).

Fig. 9. Palaeo-weathering (b, c) and magnetic-related (a, d, e, f) proxies for Zwierzyniec-1. A) shows the portable XRF data for Fe (%Fe, portable), which has a similar stratigraphic spacing to K_{surf} data. Other source geochemical proxies are based on the ICP OES-MS data of Sullivan et al. (2018). Blue horizontal lines are stage boundaries.

Fig. 10. Provenance-related proxies (b to e) and K_{surf} (a) for Zwierzyneic-1. f) The fuzzy cluster analysis classification, with the radius of the circle indicating the probability (0 to 1.0, key shown) of membership of the resistate clusters 1A to 3C. The ‘unclear’ marker is indicated for depths in which cluster membership probability does not exceeds 0.5, indicating it has no natural cluster assignment. g) The stratigraphic divisions into provenance zones (PZ1, PZ2) and subzones (H to W₂). A similar plot with all the provenance proxies used is Supplementary Fig. S10. Uses the ICP-MS data of Sullivan et al. (2018).

Fig. 11. Variable selection and principle component analysis (PCA) for the ICP OES-MS data of Sullivan et al. (2018) and χ_{cf} for Zwierzyniec-1. A) Aikes information criteria (AIC) versus step number in the forward-backward multiple-linear regression, showing the entry and exit of variables. Greyed variables not included in final selection set, with [...] indicate the two associated elements with the largest R_s values (‘-’ indicates negative correlation). b) The normalised PCA loadings for the first three principal components (PC1, PC2, PC3), and the two elements most closely associated (largest R_s) with the selected variable (‘-’ indicates negative correlation). c), d) biplots (Gabriel and Odoroff 1990) of the PC2 and PC3 against the PC1 component, with inferred interpretations of the relationships between the variables and data points. Some outlier points are marked with their extreme placements (lge=near maximum, low=near minimum, max=maximum value in set, min=minimum value in set). Large arrows show direction of inferred controlling response.

Fig. 12. a) Accumulation rate model for Zwierzyniec-1, with 3-point linear average (linear) and LOCFIT-derived (adaptive) accumulation rates. The palaeoproductivity proxies in b) and c) use the protocols proposed by Schoeper et al. (2015) using the adaptive accumulation rate model. On b) are the geometric mean primary productivity estimates (arrows with labels) using C_{org} accumulation flux, and equation 21 of Schoeper et al. (2015) for selected intervals. ESCIE= early Sheinwoodian carbon isotope excursion. d) Circulation state proxy of Sweere et al. (2016) with upwelling (<0.5, in green) and restricted (>2, in grey) circulation thresholds indicated. e) Temperature trends from Trotter et al. (2016) and Brenchley et al. (2003) and f) productivity-preservation states based on Algeo and Li (2020). Uses the geochemistry data of Sullivan et al. (2018).

Fig. 13. Summary of red-bed ages. a) positions of Llandovery eustatic highstands proposed by Haq and Schutter (2008), Johnson (2010) and Davies et al. (2016). b) the age range of northern European marine red beds. c) Avalonia and Baltica graptolite zones from Loydell (2012), with older zonations converted using fig. 2 of Zalasiewicz et al. (2009). Stage slices (S.S) from McAdams et al. (2019). Data sources in Table 1.

Table 1. Marine red beds from the Llandovery in the eastern Avalonia fringing continents. The graptolite biozones here use the definition of Rickards (1976), rather than newer biozone definitions of Zalasiewicz et al. (2009), Loydell (2012) unless indicated with #. Locations shown on Fig. 1.

Location	Formation	Biozone{slice}	Depositional Environment	Reference
Laurentia				
Wigtown and Kirkcudbright Peninsulas, SW. Scotland	Carghidown	<i>crenulata</i> {Te3-e.Te5}	Turbiditic and hemipelagic mudstones	Rust 1965; Kemp 1986; Scrutton and McMurray 1987; White et al. 1991.
Rhinns of Galloway, SW. Scotland	Chair Mbr of Mull of Logan Fm	<i>sedgwickii</i> or <i>turriculatus</i> {Ae3-Te1}	Turbiditic and hemipelagic mudstones	Scrutton and McCurry 1987
Kilbride Peninsula, W. Eire	Tonalee	Late Telychian, probably <i>crenulata</i> {Te3-e.Te5}	Deep water, benthic shelly <i>Clorinda</i> community	Doyle et al. 1990; Rickards 1973
Pomeroy Inlier, Northern Ireland	Corrycroar Group	<i>crenulata</i> ?	graptolitic fine sandstones and mudstones	Fernside et al. 1906 Aldridge et al. 2002
Girvan, SW. Scotland	Lauchlan Mudstone	<i>griestoniensis</i> and <i>crenulata</i> {1.Te2-e.Te5}	shelly <i>Clorinda</i> community, turbiditic and deepwater	Floyd and Williams 2002
Pentland Hills S. Scotland	Reservoir	# <i>spiralis</i> {1.Te3}	Deepwater fan to deep shelf	Bull and Loydell 1995; Barron 1998
East Avalonia Terrane				
Balbriggan inlier, E. Eire	Balbriggan	late Telychian	Mudstones and turbiditic sandstones, graptolitic	Rickards et al. 1973; Aldridge et al. 2002
Kildare inlier, Eire	Rahilla	Telychian	Overlies graptolitic shales	Parkes and Palmer 1994
Cumbria, Howgill Fells, Cross Fell Inlier, UK.	Hebblethwaite Mbr	<i>crenulata</i> {Te3-e.Te5}	Deep water, graptolitic	Rickards 1973; Rickards and Woodcock 2005; Aldridge et al. 2002; Hounslow et al. 2021b
Mid and NE. Wales	Dolgau Mudstones Formation	<i>crenulata</i> {Te3-e.Te5}	Deep water, graptolitic, locally turbiditic	Wood 1906, Wilson et al. 2016
Banwy River, E. Wales	Tarannon	# <i>crispus</i> to lower (?)	Deep water, graptolitic	Loydell and Cave 1996

	Mudstones	<i>spiralis</i> {e.Te2- 1.Te3}		
Buttington Quarry, Long Mountain, E. Wales	Tarannon Mudstones	# <i>turriculatus</i> to <i>spiralis</i> {Te1-1.Te3}	Mudstones and thin sandstones, partly graptolitic	Cave and Dixon 1993; Mullins and Loydell 2002; Aldridge et al. 2000; Hounslow et al. 2021b
Shropshire, England	Purple Shales	<i>turriculatus</i> to <i>crenulata</i> {Te1-e.Te5}	<i>Clorinda</i> community of the deep-water shelf	Benton and Gray 1981; Aldridge et al. 2002; Cocks and Rickards 1968
Condroz inlier, Belgium	Dave	<i>griestoniensis</i> to <i>crenulata</i> {1.Te2-e.Te5}	outer shelf environment	Maes et al. 1979; Verniers et al. 2001, 2008
Baltica				
Ringerike and Asker districts. Oslo, Norway	Vik	# <i>crispus</i> to <i>crenulata</i> {Te2-e.Te3}	Deep water shelf, graptolitic	Worsley et al. 1983; Baarli 1990a; Calner et al. 2013.
Gotland, subsurface		<i>sedgwickii</i> and. <i>spiralis</i> zones {Ae3-Te3}	mid water shelf	Grahn 1995
Aizpute-41, Ventpils-D3 and Vik cores, W. Latvia- SW Estonia,	Velise and Jurmala	# <i>turriculatus</i> to <i>crenulata</i> {1.Te1-e.Te3}	Deep offshore shelf claystones	Kiipli et al. 2000b, 2012; Kiipli 2004; Loydell et al. 2003; Munnecke and Männik 2009
Gotland, subsurface		<i>cyphus</i> {Rh3}	Deep water shelf,	Grahn 1995
Latvia, Aizpute-41 and Engure cores	Remte Fm and Juura Stage	late Rhuddanian {Rh3}	Deep offshore shelf claystones	Kiipli et al. 2000b, 2004; Loydell et al. 2003; Radzevičius 2013.

Table 2. Geochemical weathering indices used here. CIA = Chemical index of alteration; WIP=weathering index of Parker; Silica-Titania index. Formula's using molecular proportions of element oxides. From Price and Velbel (2003). We use here $WIP_R = 100 - WIP$ and $STI_R = 100 - STI$, since these then invert the relationship to weathering, with the reverse-index conforming to a positive relationship with degree of weathering like CIA. CaO* = corrected for CaO in apatite, calcite, dolomite and ankerite (Fedo et al. 1995), as determined by MINLITH (Rosen et al. 2004) from the bulk-rock ICP-OES data of Sullivan et al. (2018).

Index	Formula	Fresh/totally weathered values	Allow Al-mobility	Reference
CIA	$100 \times [Al_2O_3 / (Al_2O_3 + CaO^* + Na_2O + K_2O)]$	$\leq 50 / 100$	No	Nesbitt and Young 1982
WIP	$100 \times [2Na_2O / 0.35 + (MgO / 0.9) + (2K_2O / 0.25) + CaO^* / 0.7]$	$> 100 / 0$	Yes	Parker 1970; Price and Velbel 2003
STI	$100 \times [SiO_2 / TiO_2 / ((SiO_2 / TiO_2) + (SiO_2 / Al_2O_3) + (Al_2O_3 / TiO_2))]$	$> 85 / \text{ca. } 60$	No	Jayawardena and Izawa 1994

Table 3. Geometric means of the provenance-specific trace element ratios for the provenance subzones in Zwierzyniec-1. Resistate fuzzy clusters which correspond to the subzonal divisions indicated in last column. SCF= strata discrimination function of Hounslow and Morton (2004), which is a proxy for the stratigraphic-related noisiness of a dataset (larger values indicate less noisy).

Provenance zone	subzone	Depth range (m)	0.1×Zr/Sc	10×Sc/Cr	Ga/Sc	0.1×Zr/Nb	25×TiO₂/Nb	Resistate clusters
PZ2	W ₂ :	2900-2911.0	1.24	1.56	1.30	1.36	1.46	3C/2C
	W ₁ :	2912-2933.48	1.24	1.56	1.38	1.25	1.35	2C/3C/1C
	M ₂ :	2934.0-2953.51	1.20	1.70	1.20	1.25	1.33	1C/2C
	M ₁ :	2954.0-2968.42	1.06	1.85	1.09	1.16	1.34	1C/2C/B
PZ1	A:	2968.8- 2971.0	0.92	1.24	1.08	1.19	1.33	1A/2A
	R ₂ :	2971.2-2973.5	0.89	1.35	1.00	1.08	1.26	B/2A
	R ₁	2973.9-2987.0	0.94	1.31	1.09	1.07	1.29	1A/B
	H:	2987.4-3010.0	1.01	1.30	1.13	1.20	1.34	2A/1A
		SCF	0.68	0.70	0.64	0.48	0.36	

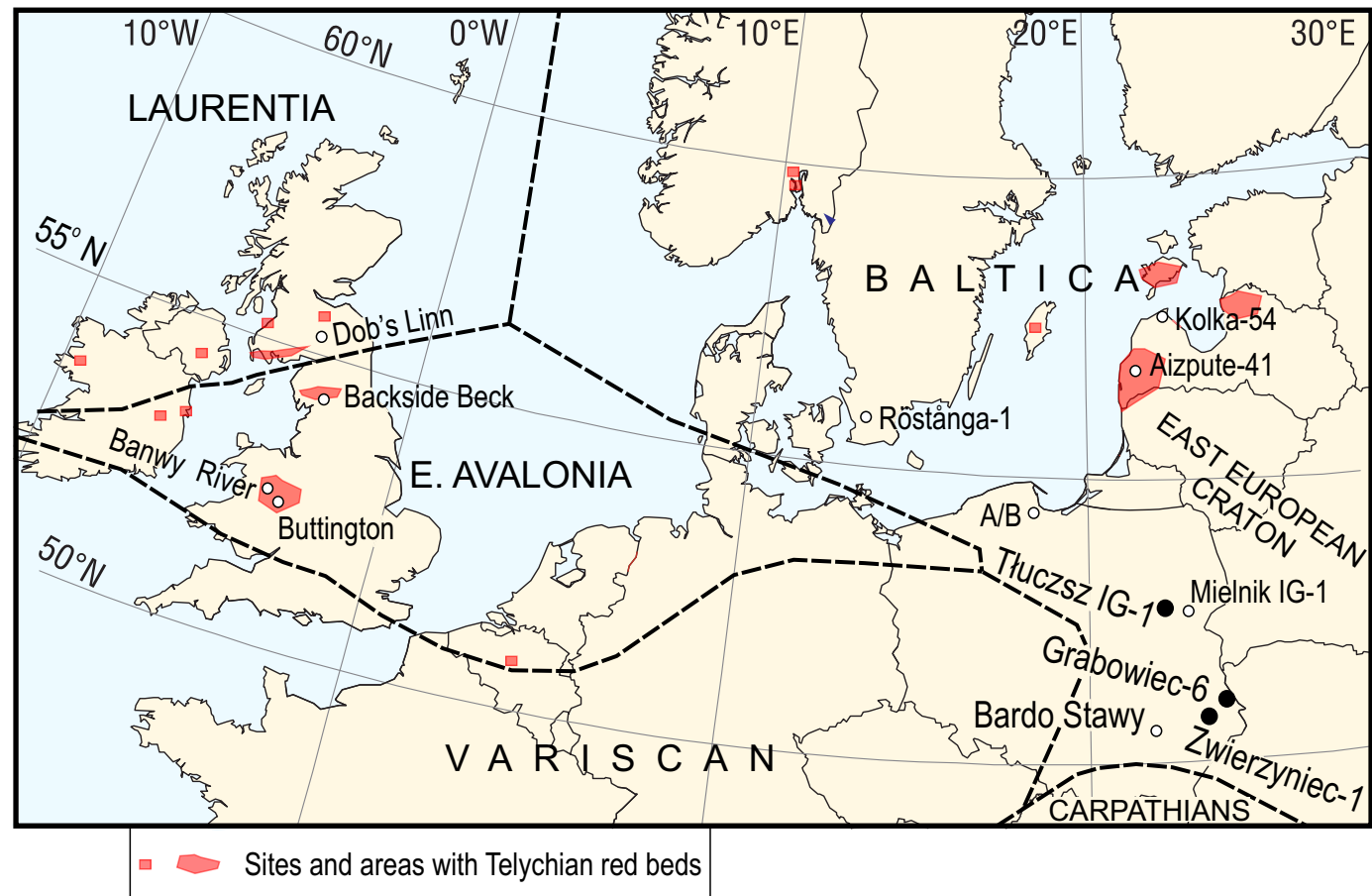


Fig. 1.

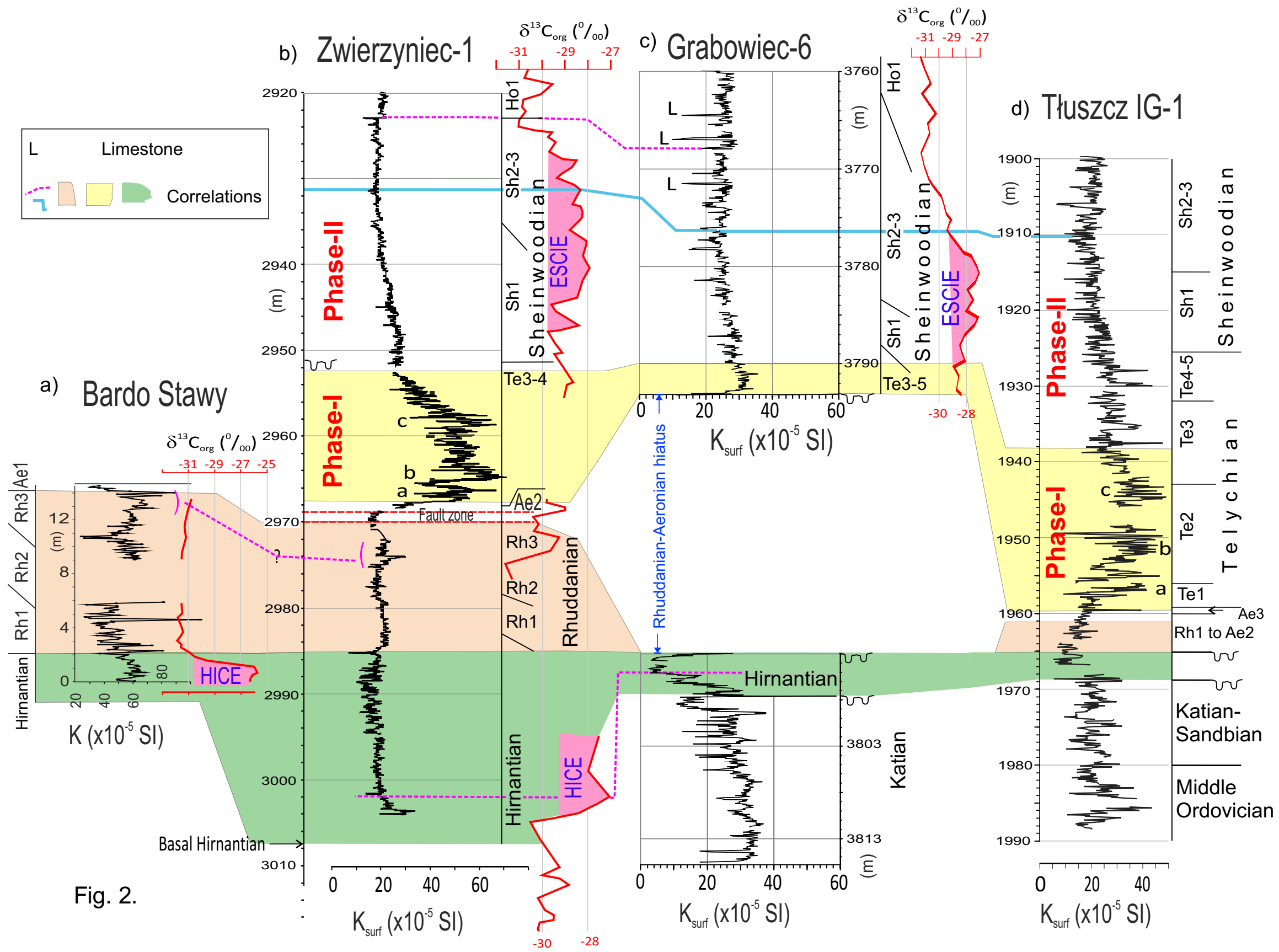


Fig. 2.

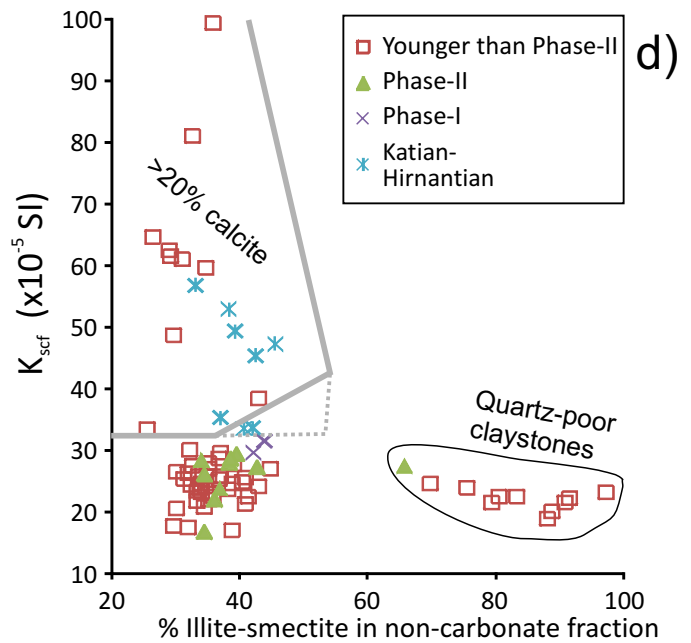
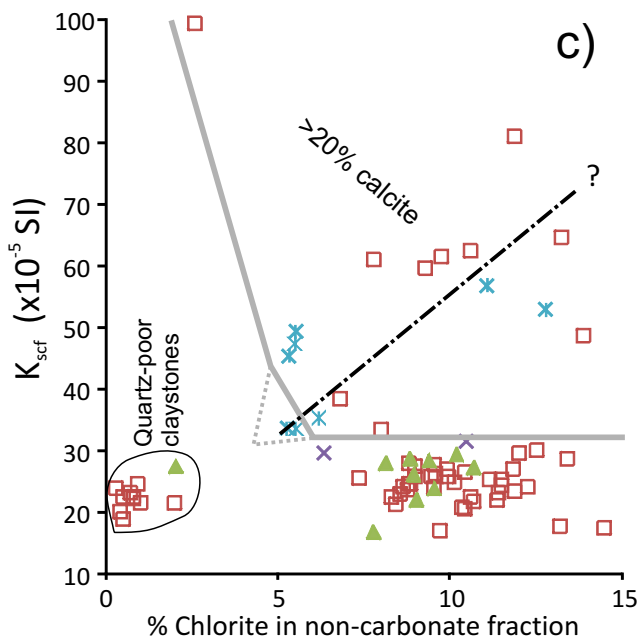
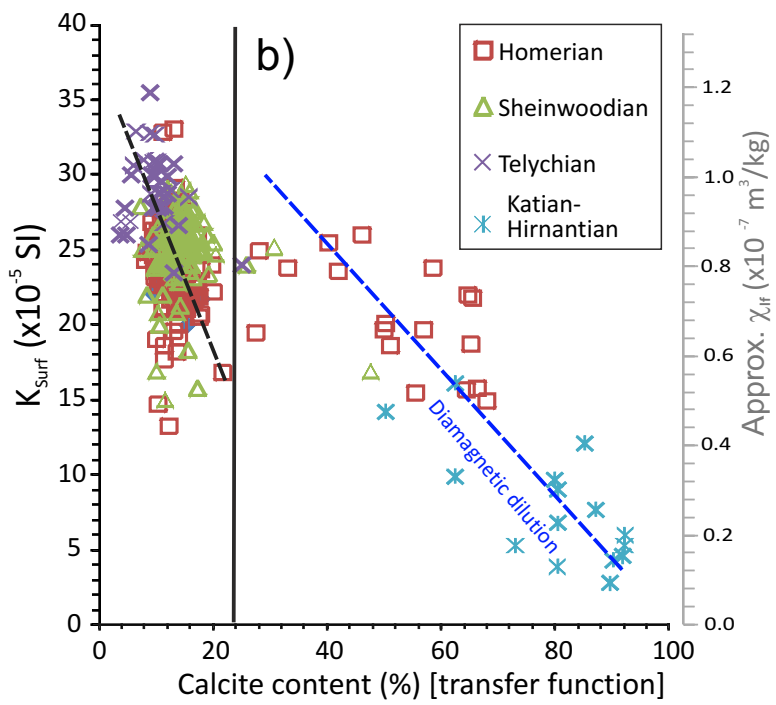
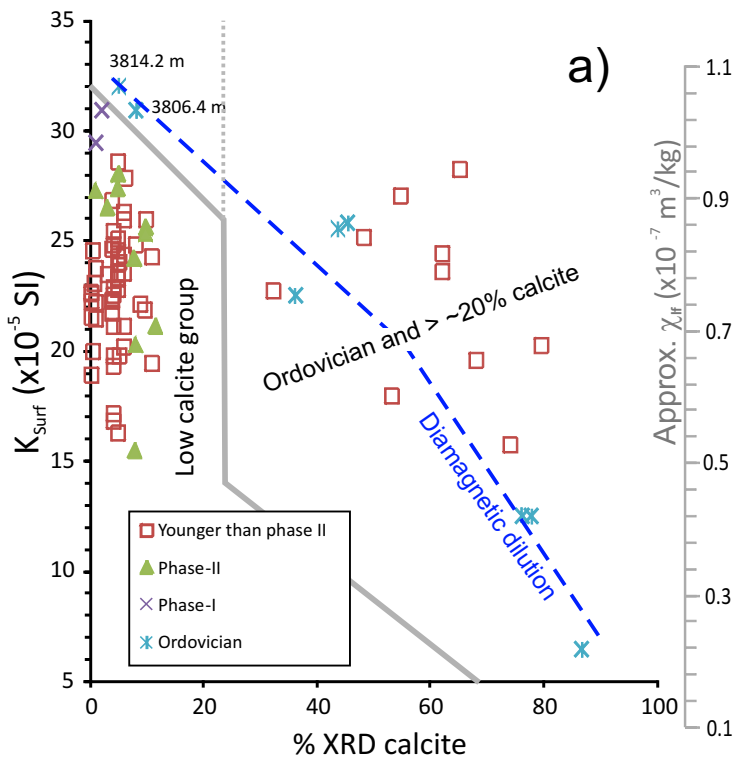


Fig. 3.

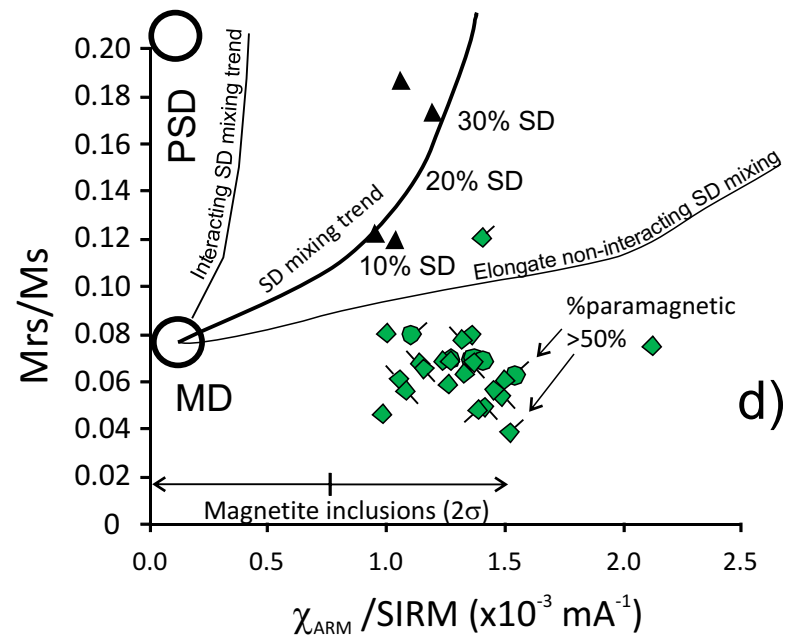
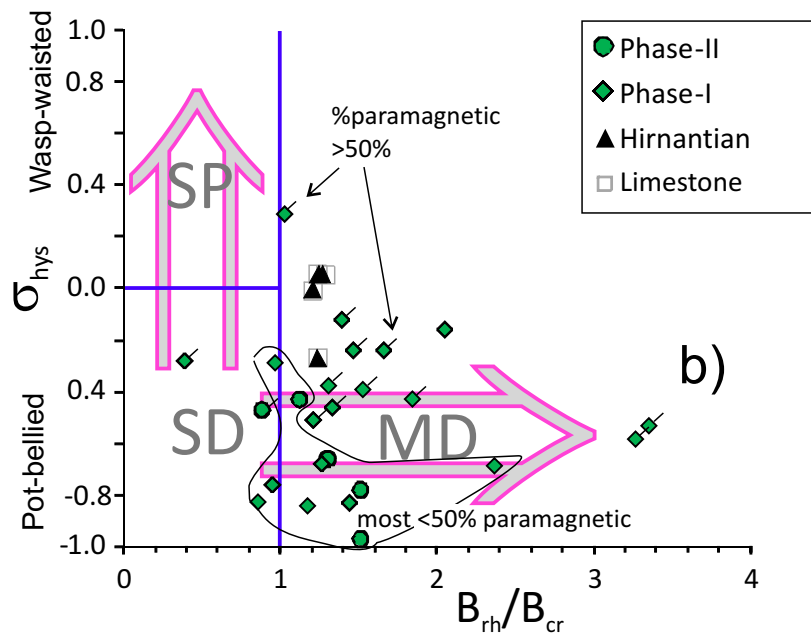
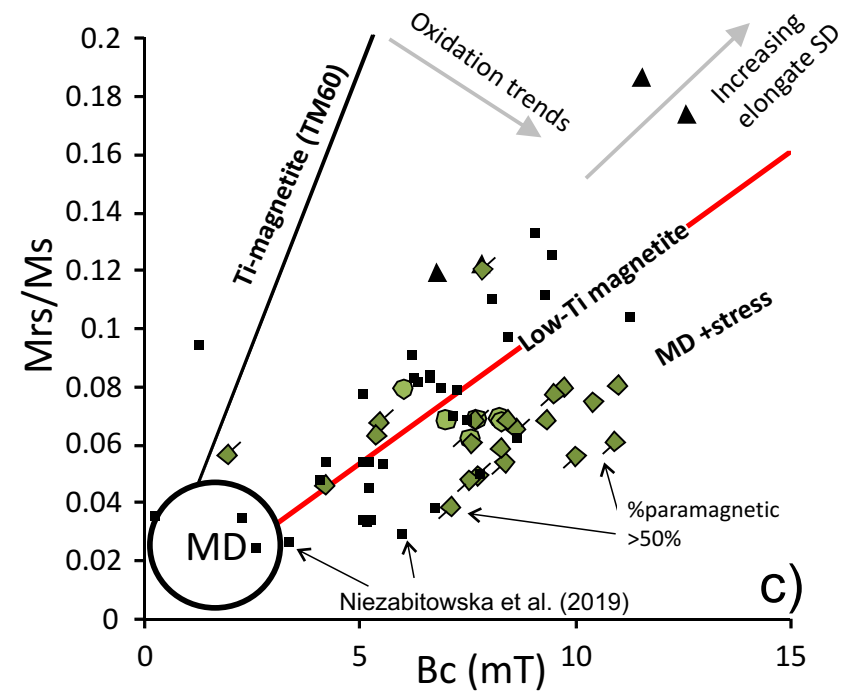
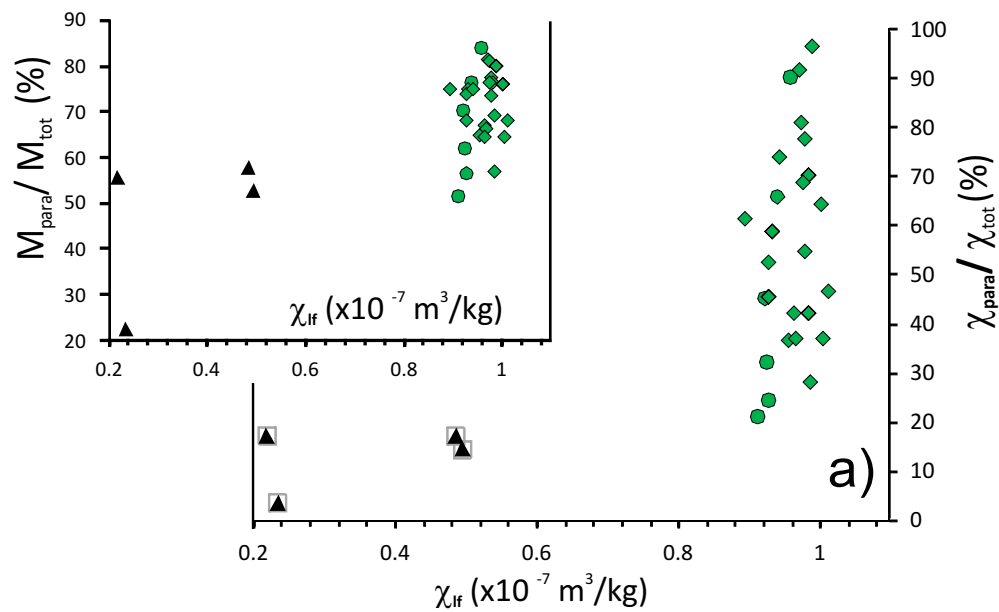


Fig. 4.

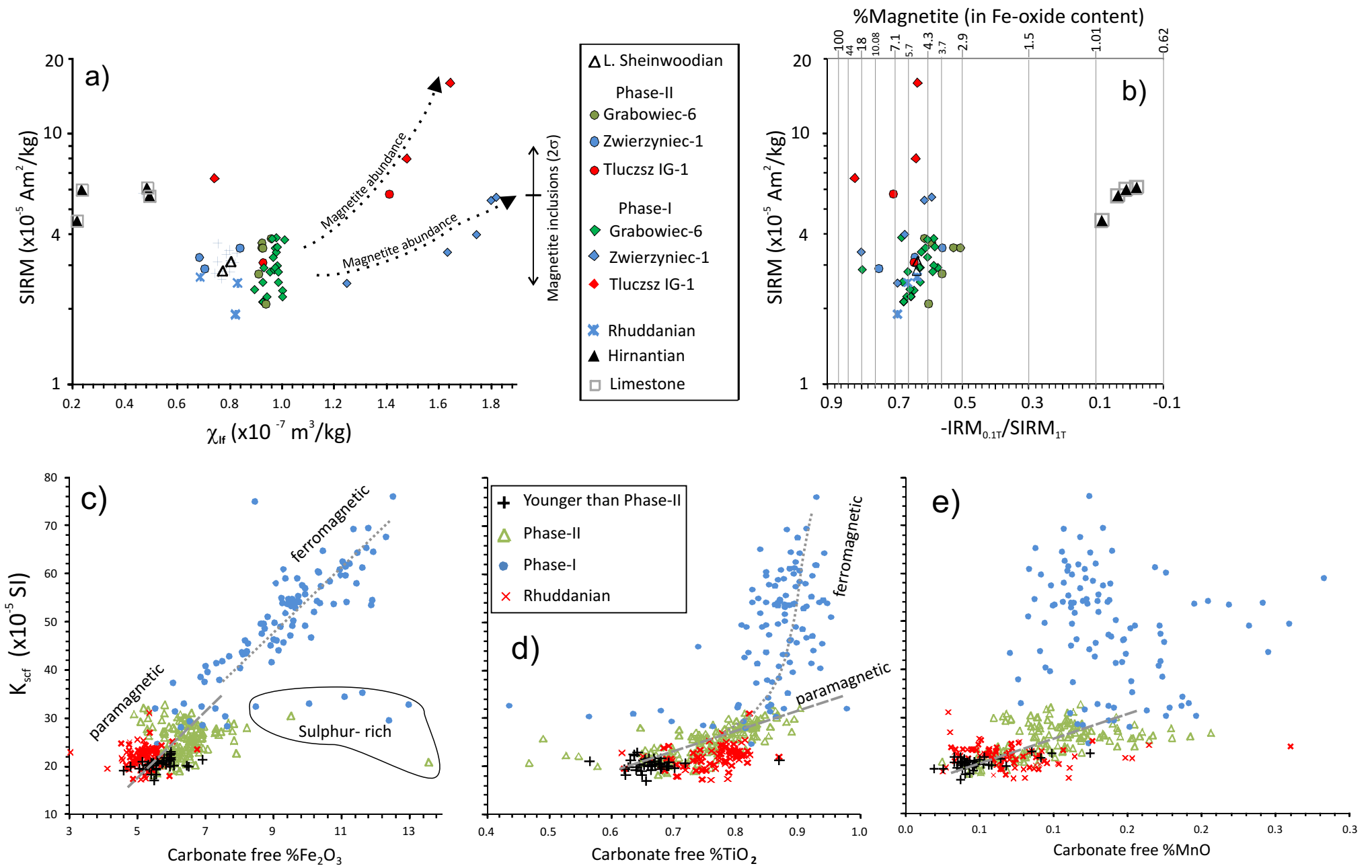


Fig. 5

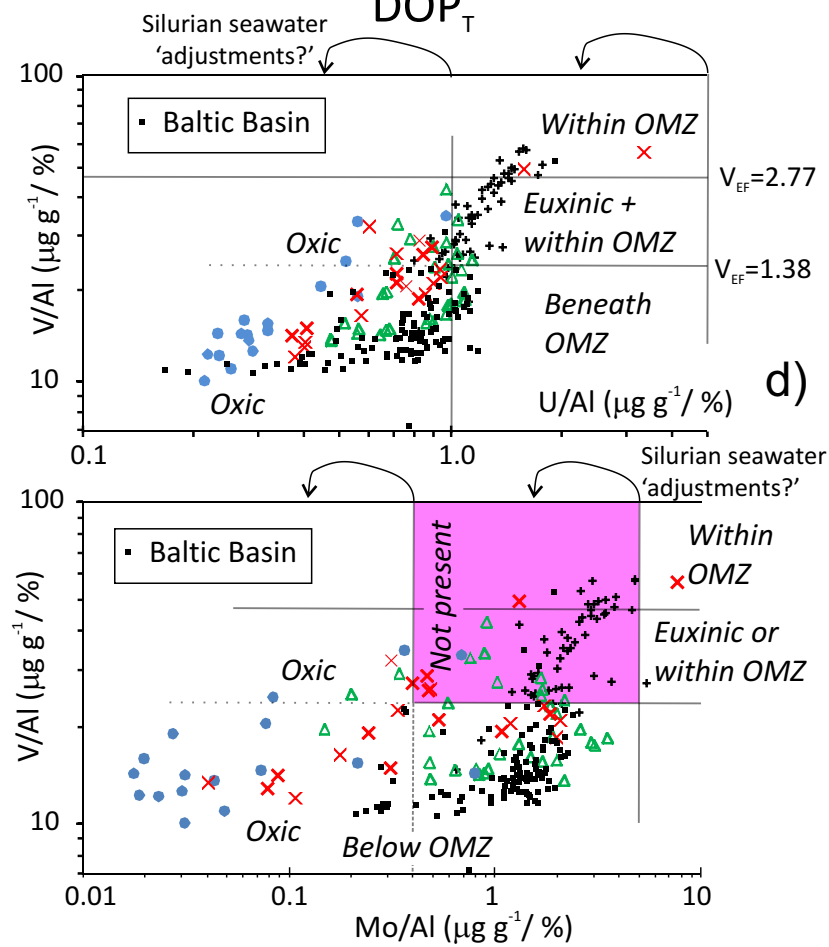
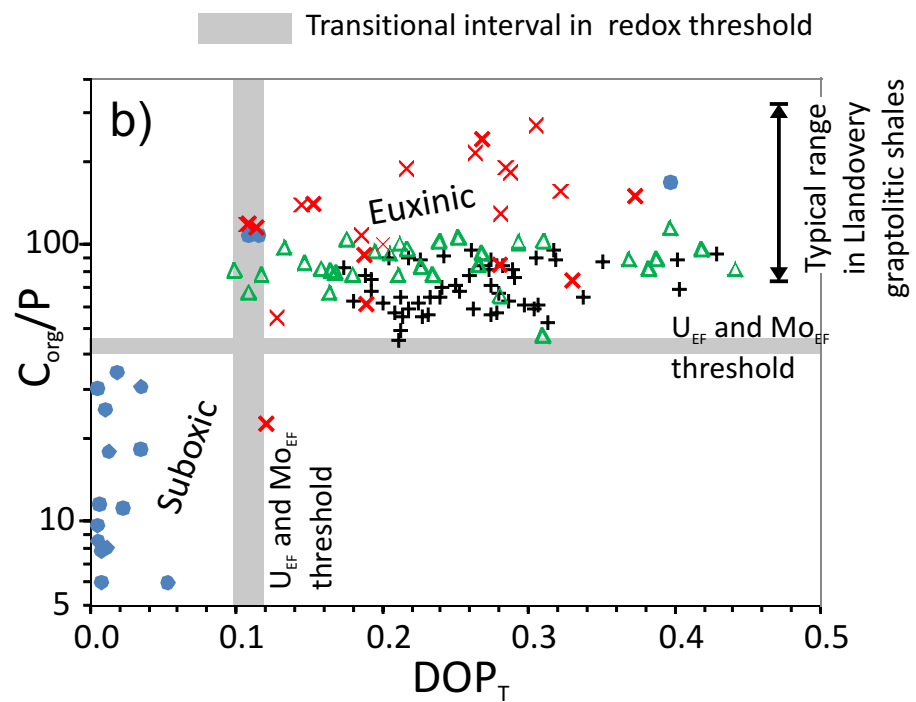
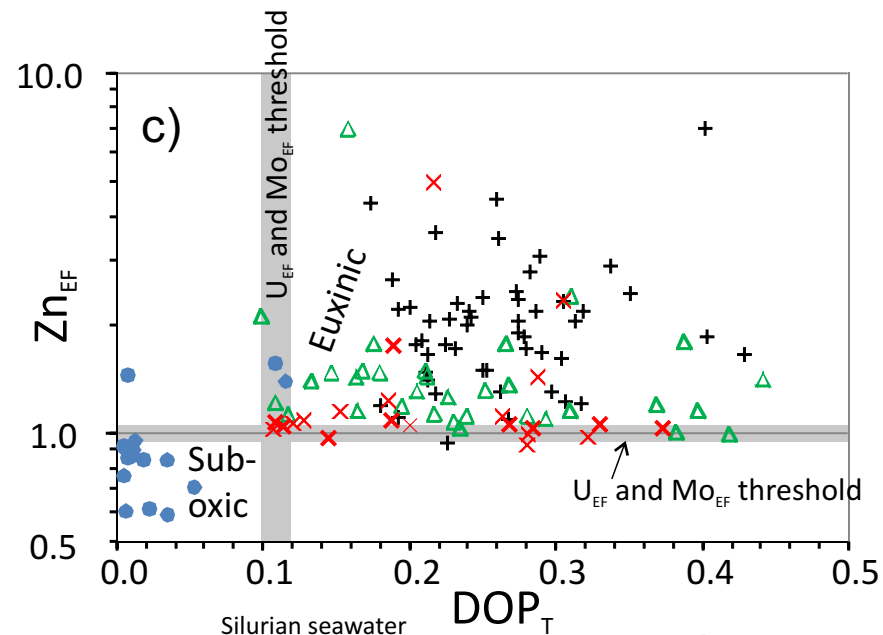
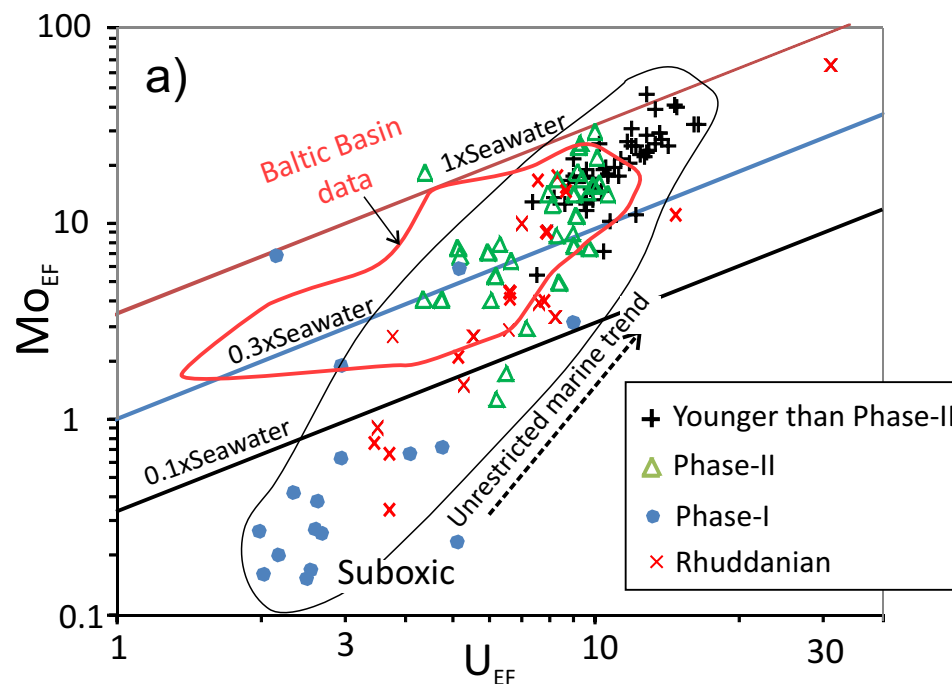


Fig. 6

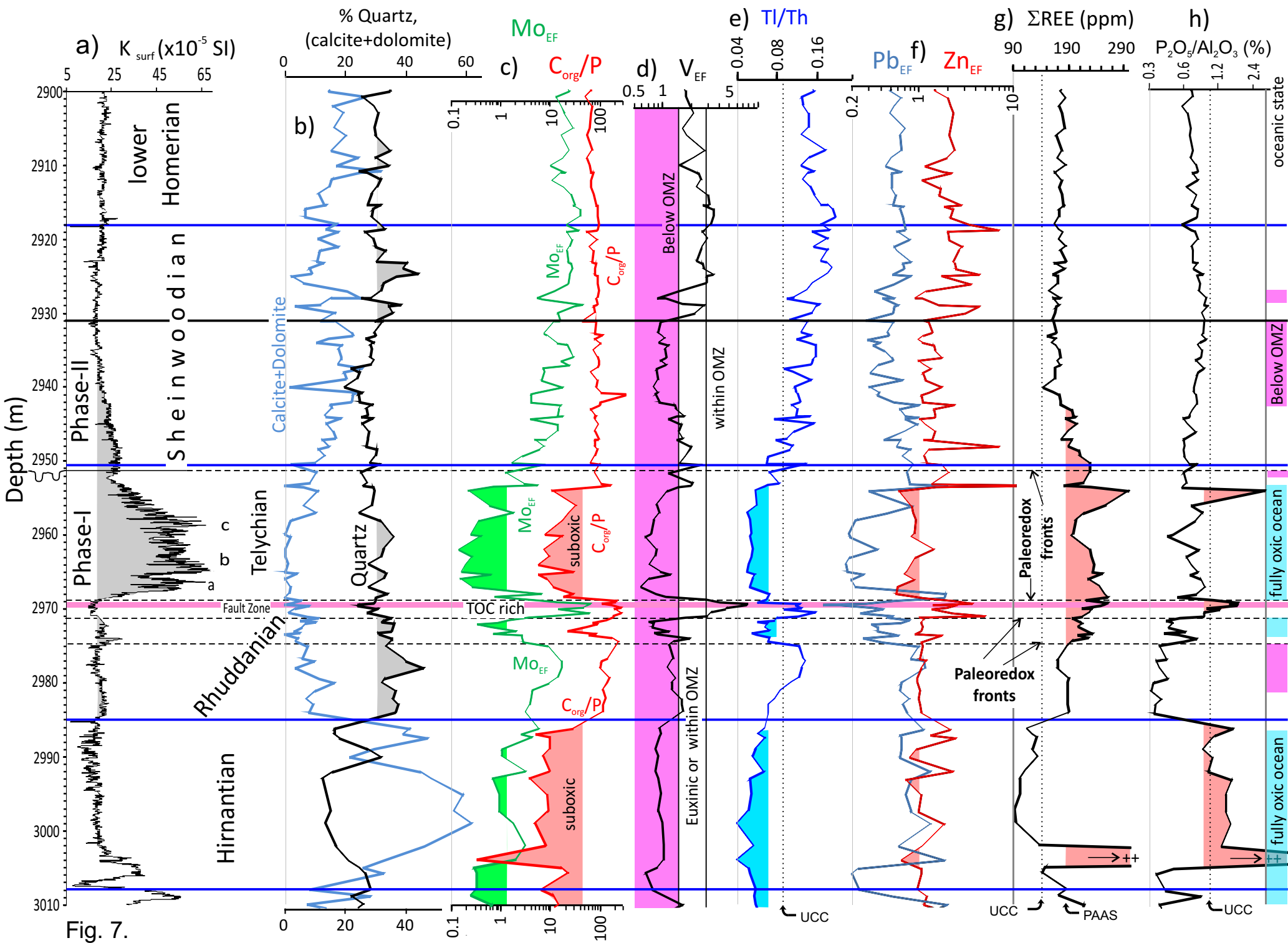


Fig. 7.

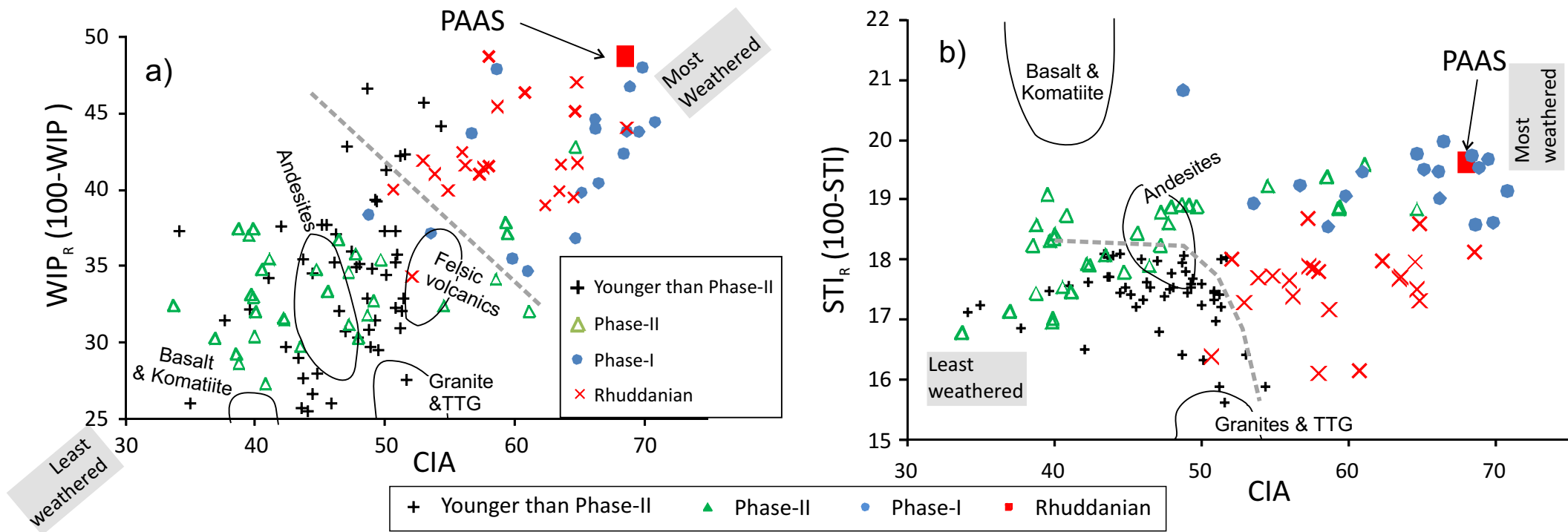


Fig. 8.

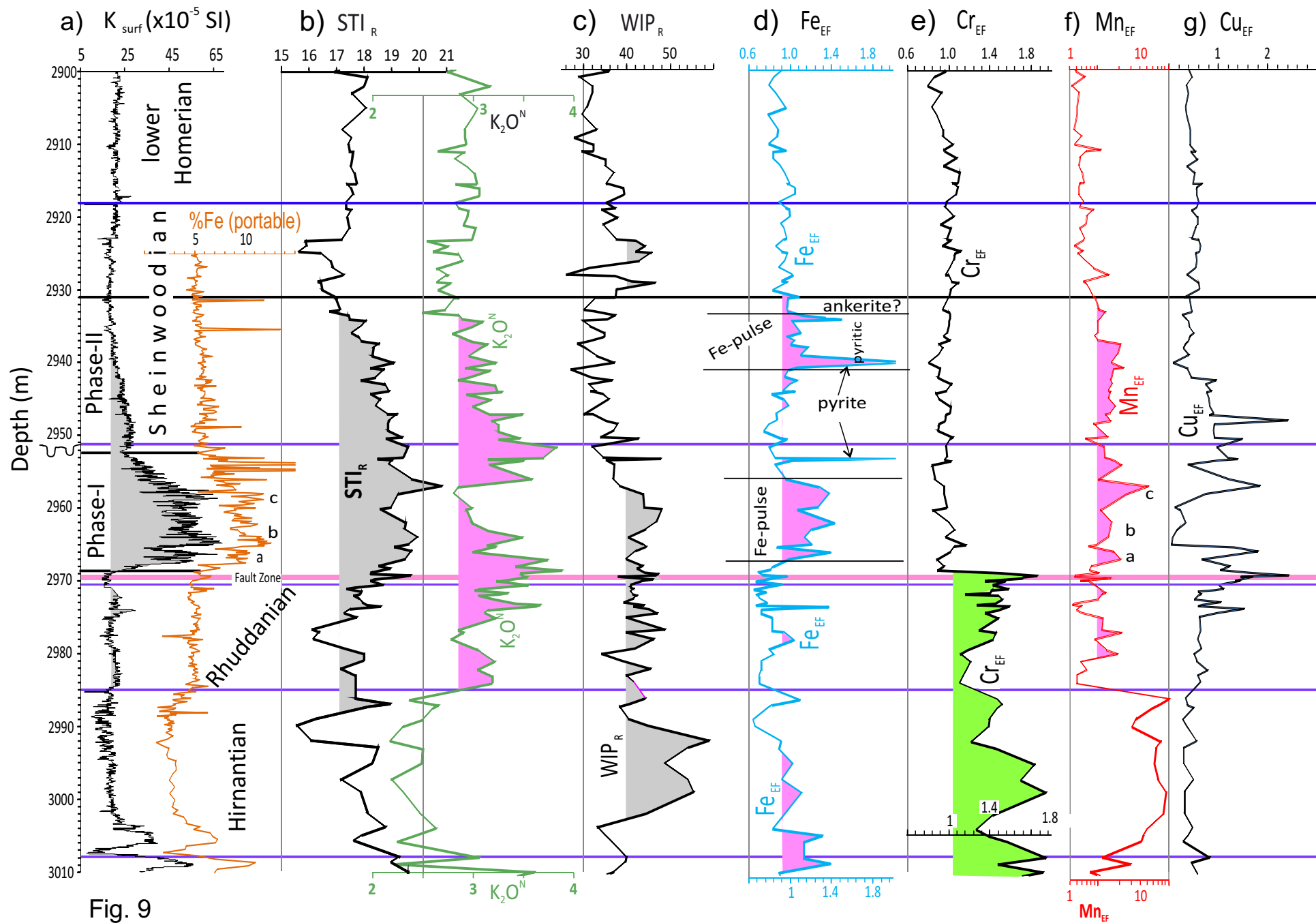


Fig. 9

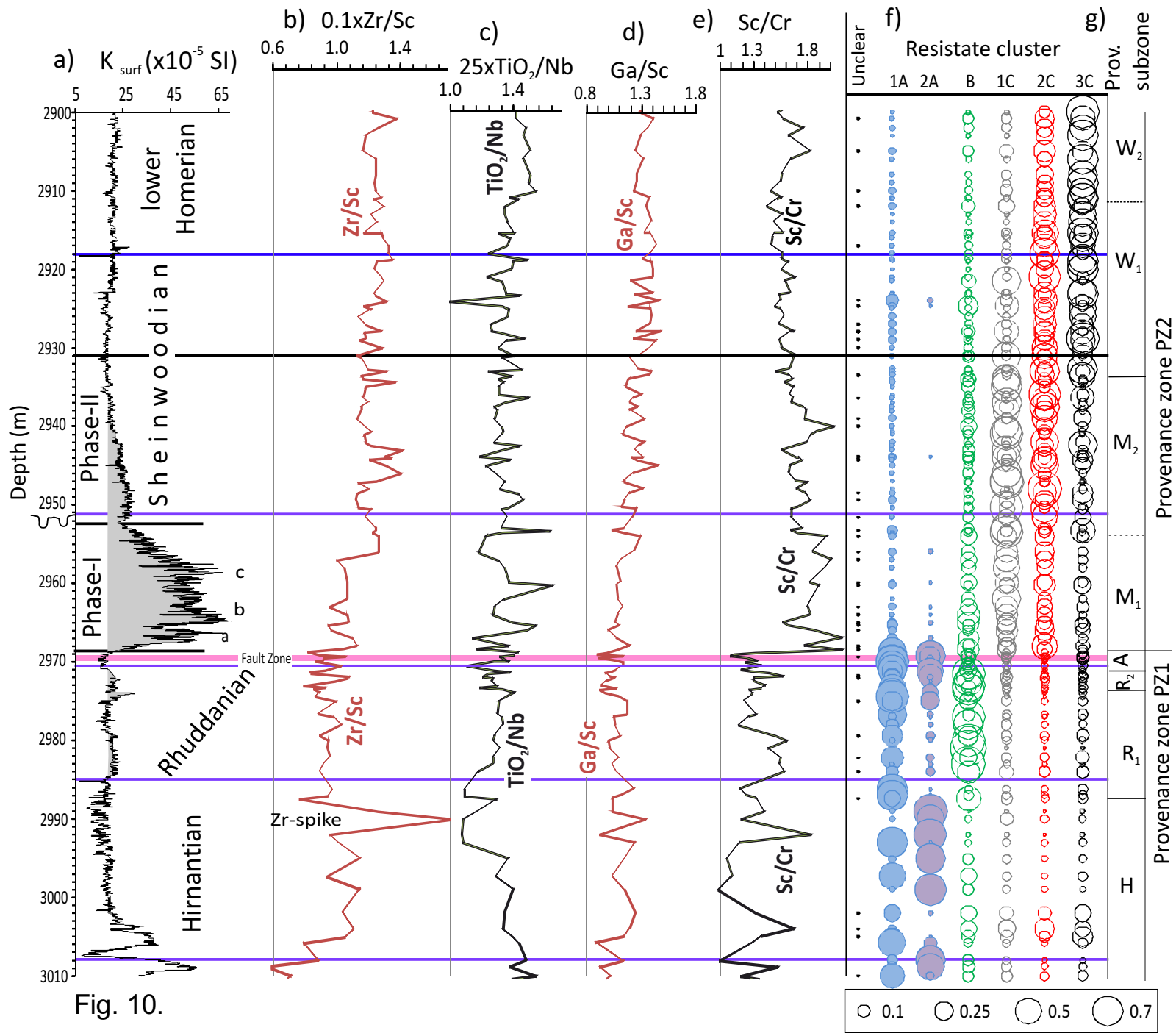


Fig. 10.

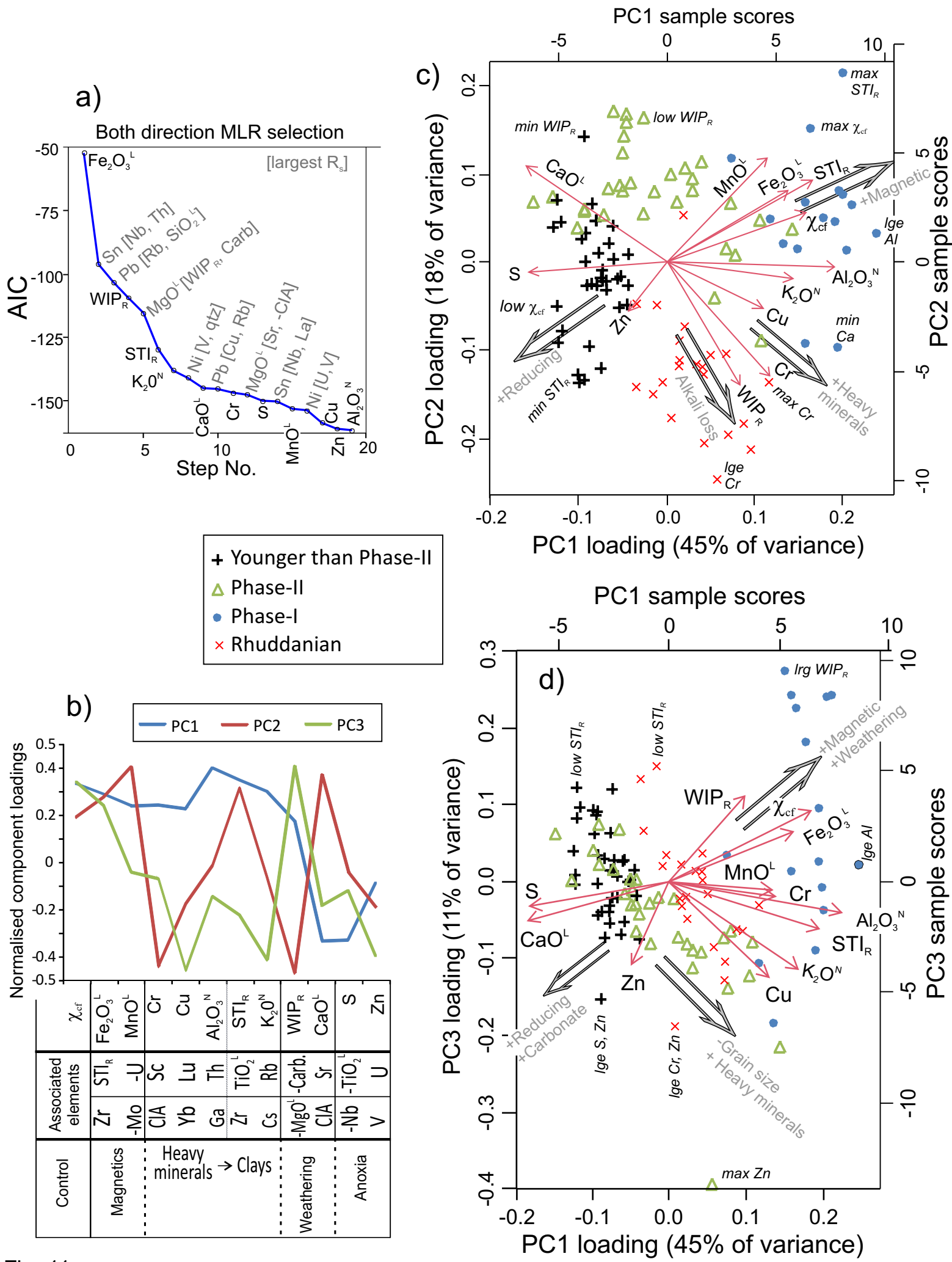


Fig. 11.

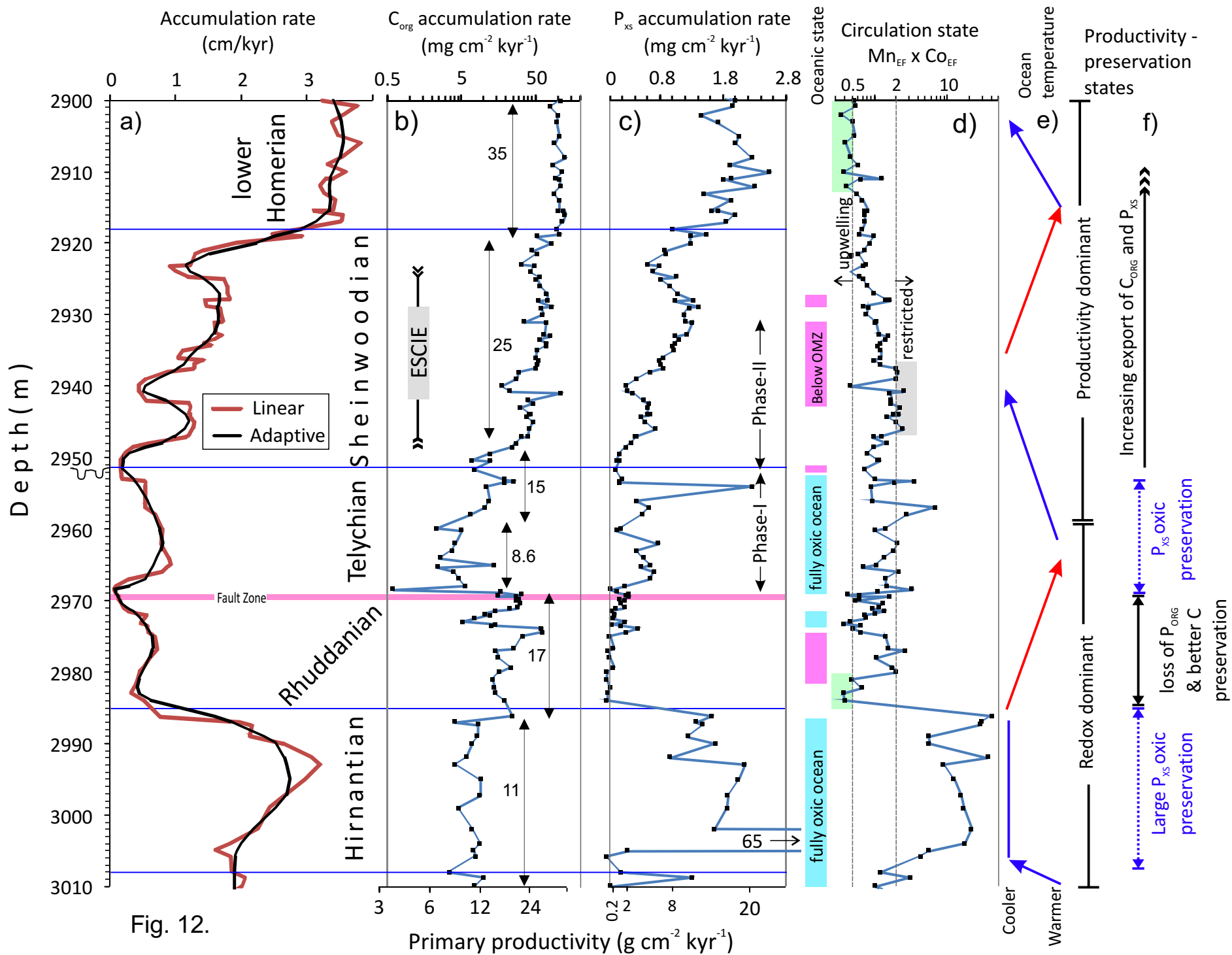
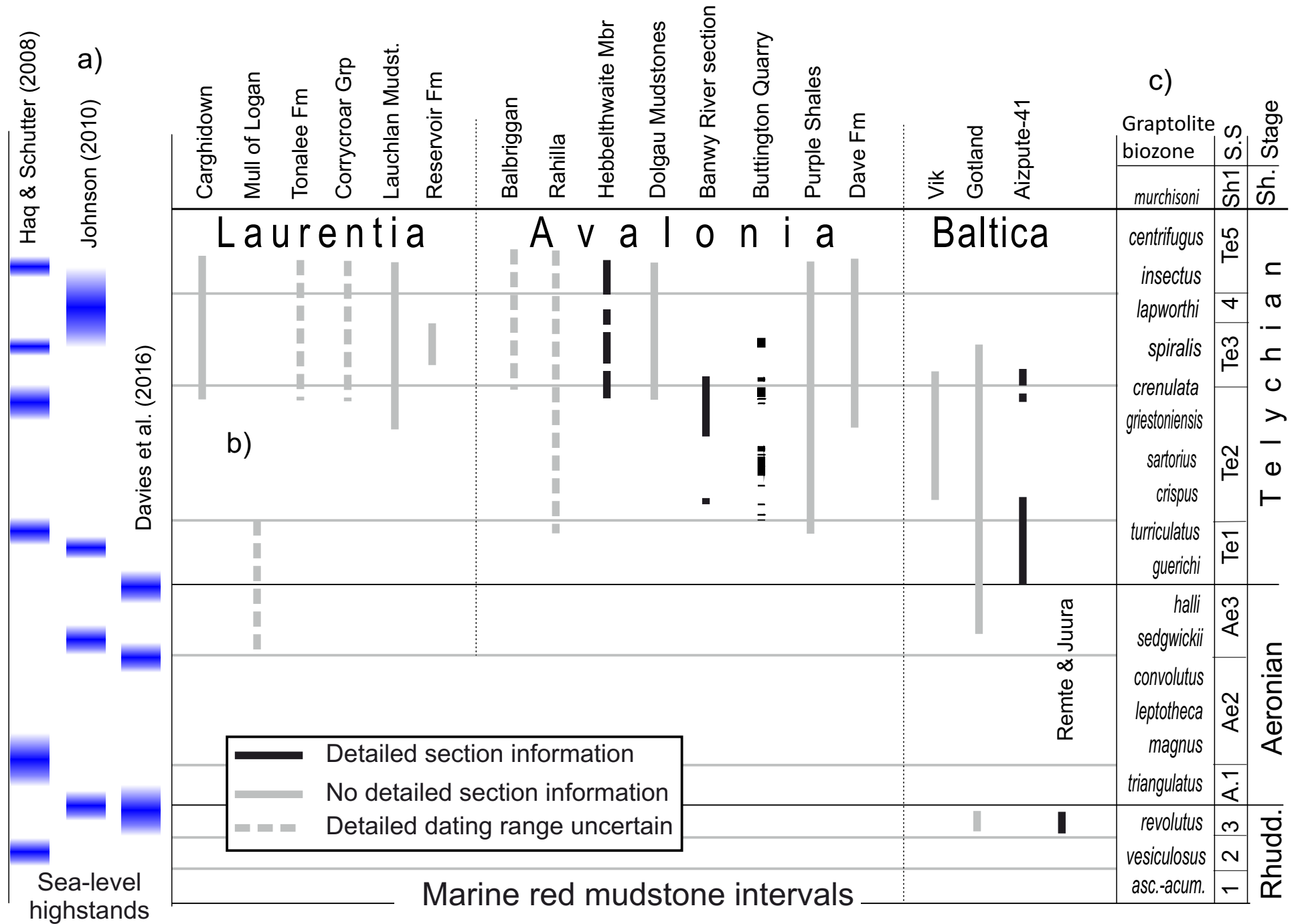


Fig. 12.

Fig. 13.



The Telychian (early Silurian) oxygenation event in northern Europe: A geochemical and magnetic perspective

Supplementary information

Mark W. Hounslow, Kenneth T. Ratcliffe, Samuel E. Harris, Jerzy Nawrocki, Krystian Wójcik, Paul Montgomery, Nigel H. Woodcock.

This contains the following:

1. Data on mineralogical components and gamma- magnetic susceptibility(MS) relationships of Grabowiec-6 and Zwierzyniec-1.
2. Threshold plots for redox proxies for Zwierzyniec-1.
3. Rare earth element data interpretation for Zwierzyniec-1.
4. Provenance evaluation of Zwierzyniec-1, of the likely East European Craton sediment sources.
5. Age-depth model for Zwierzyniec-1, flux and estimation of detrital P.
6. Additional statistical details of MS to element correlations.
7. Associated Excel file with datasets

1. Data on mineralogical components of Grabowiec-6 and Zwierzyniec-1

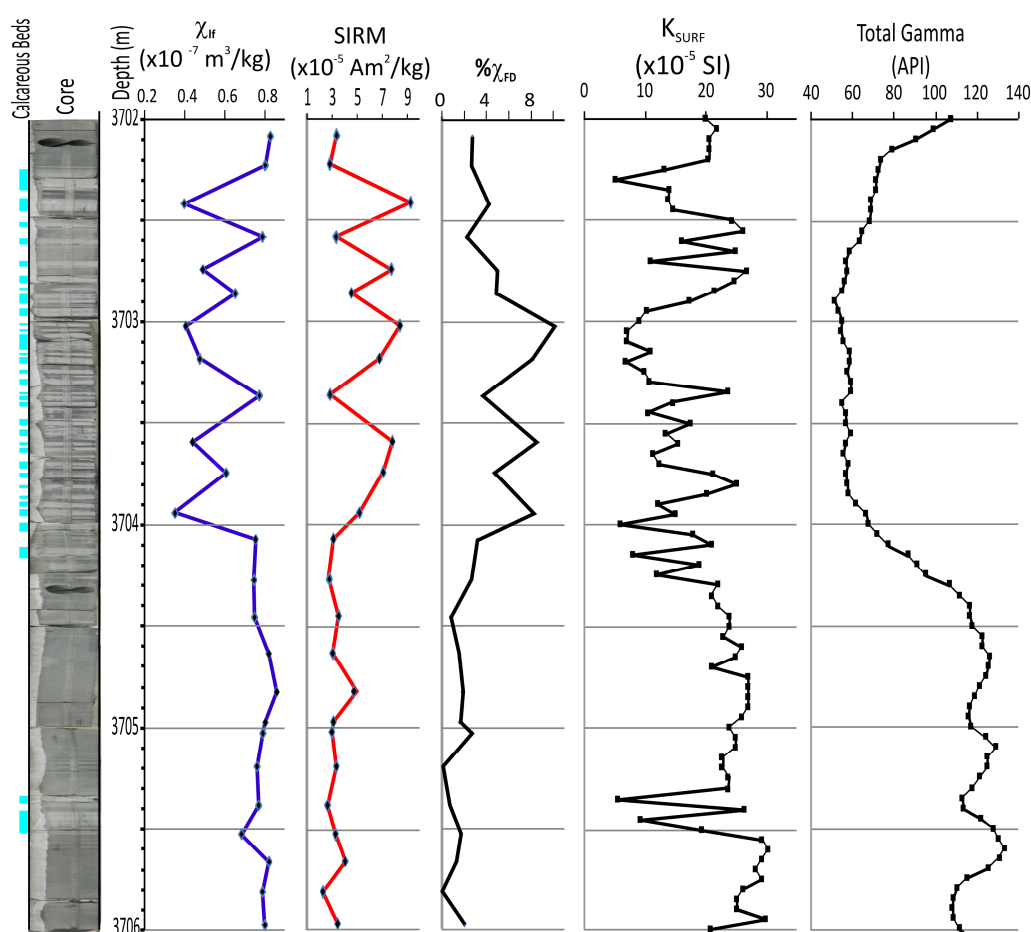


Fig. S1. Example of carbonate, gamma and magnetic datasets from the lower Gorstian part of the Grabowiec-6 core, illustrating the carbonate ‘dilution’ effect on MS and gamma. The left hand column is a compressed core photograph, on which the carbonate-rich levels are marked in light blue.

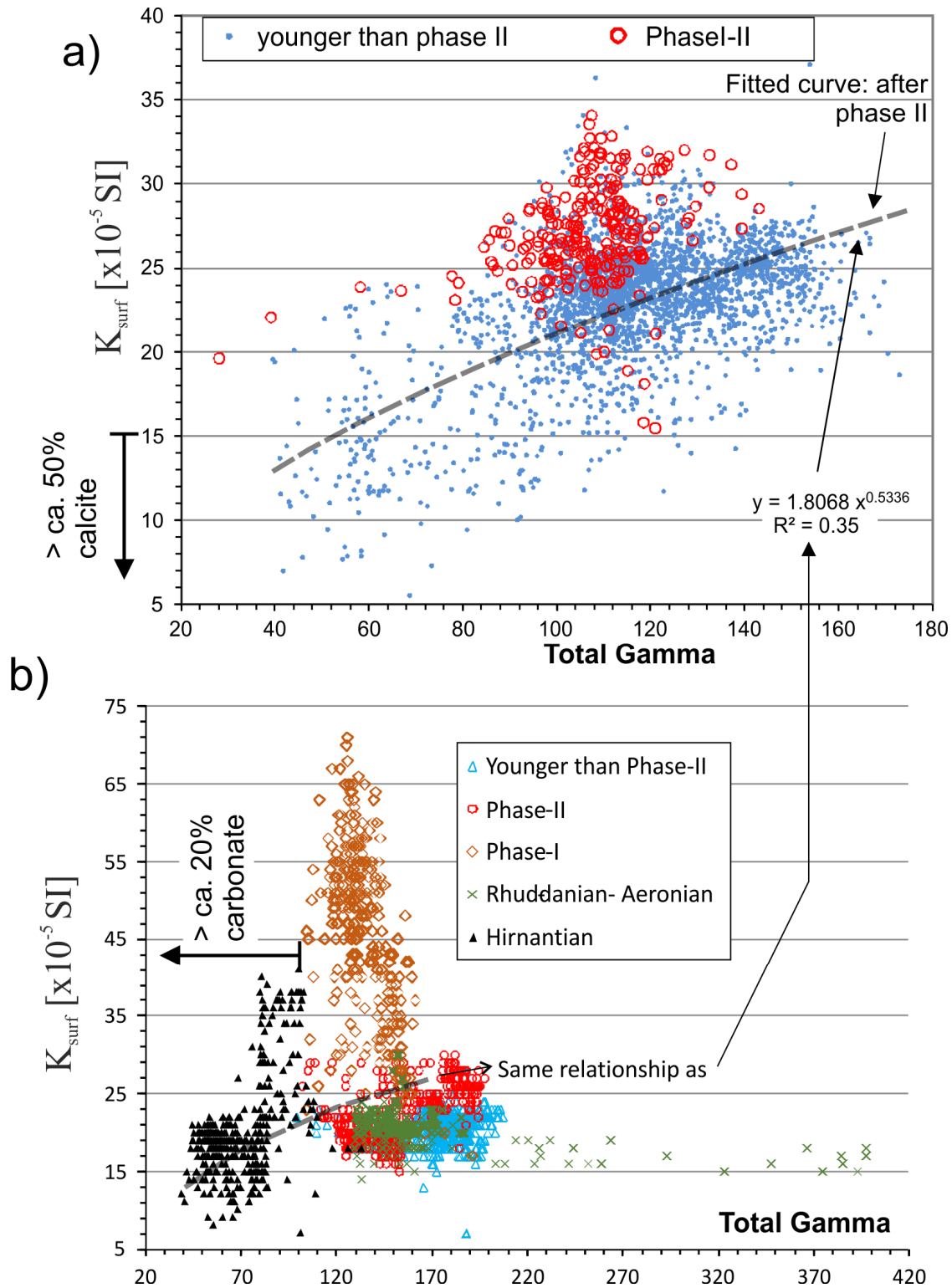


Fig. S2. a) Gamma (API) versus K_{surf} for Grabowiec-6, showing the generally positive relationship between gamma and K_{surf} . 10 cm spaced K_{surf} values have been smoothed using a bandwidth of 7 and a quadratic filter (Gorry 1990) to best match the intrinsically smoothed gamma. Curve between gamma and K_{surf} is for the data younger than the Phase-II interval. b) K_{surf} data (unsmoothed) for Zwierzyniec-1 verses gamma illustrating only a partial relationship, partly related to the carbonate dilution (curve shown in a).

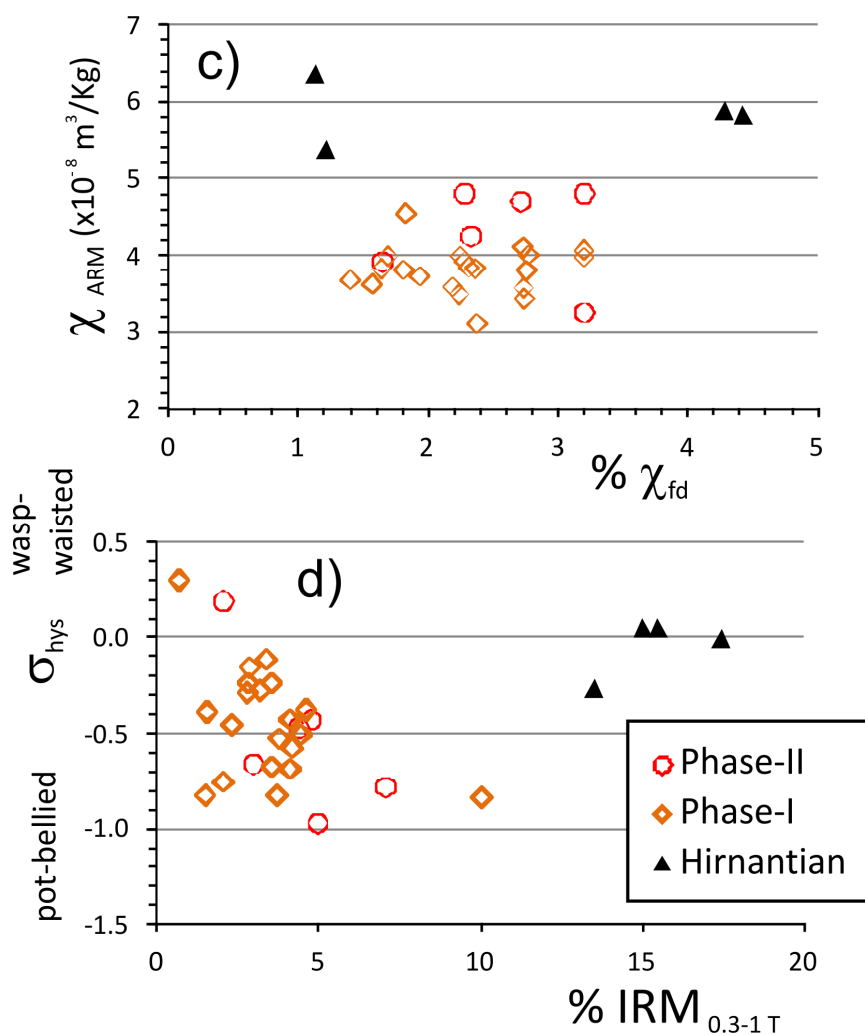


Fig. S2. Rock magnetic data for the Llandovery and Hirnantian in Grabowiec-6. C) χ_{ARM} versus the $\% \chi_{\text{fd}}$. χ_{ARM} is a proxy for concentration of ultra-fine-grained magnetite near to the single-domain superparamagnetic boundary. $\% \chi_{\text{fd}}$ is a proxy for the amount of superparamagnetic magnetic which contributes to the MS (values around 10% indicate substantial contributions). D) σ_{hys} versus the percent IRM acquired between 0.3- 1T fields ($\% \text{IRM}_{0.3-1\text{T}}$) with respect to an IRM acquired at the maximum 1T field. $\% \text{IRM}_{0.3-1\text{T}}$ is a proxy for the relative proportion of haematite(+goethite) with respect to the total ferromagnetic content. In this case indicating the Hirnantian samples contain proportionally more haematite.

In order to determine mineralogical components we have used the limited quantitative XRD data and generated a transfer function using the bulk rock ICP-OES- geochemistry to infer calcite, quartz contents. In each case the transfer functions in Figs S3, S4a,b. list the coefficients for the oxide components, so the calculated content is say, $X = C + \sum(f_i \cdot O_i)$, $i = 1 \dots n$ oxides; where C = constant value, f_i = coefficient of oxide-1, and O_i is the relevant oxide content in wt%. These were determined in excel solver function to minimise the squared difference, with anchoring to the origin (0,0).

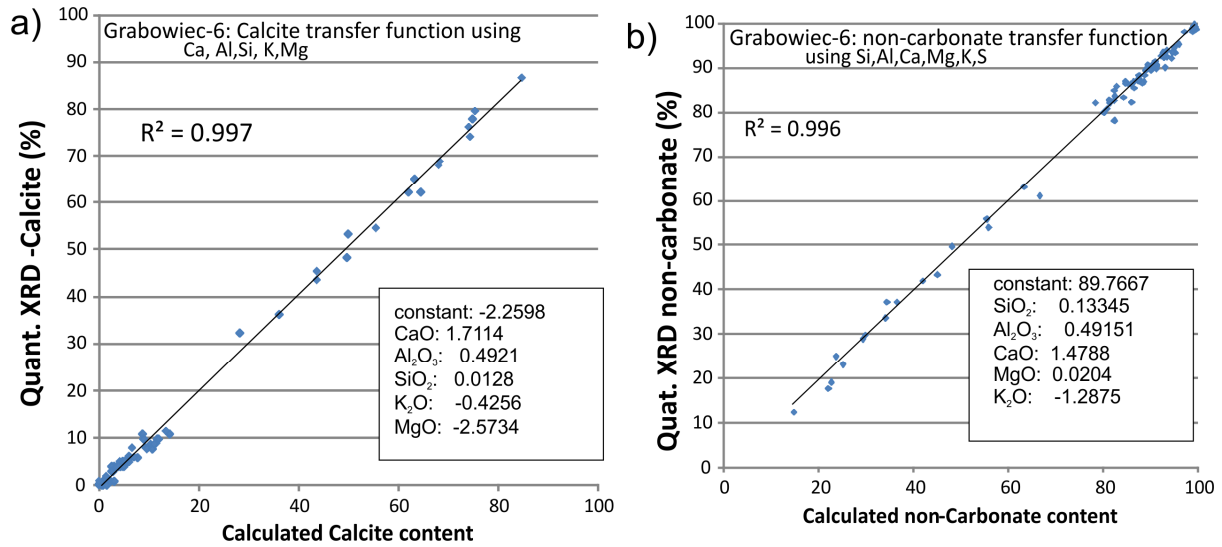


Fig. S3. The a) calcite and b) non-carbonate transfer functions for Grabowiec-6. R^2 is the Pearson correlation coefficient between XRD determined contents and calculated percentage.

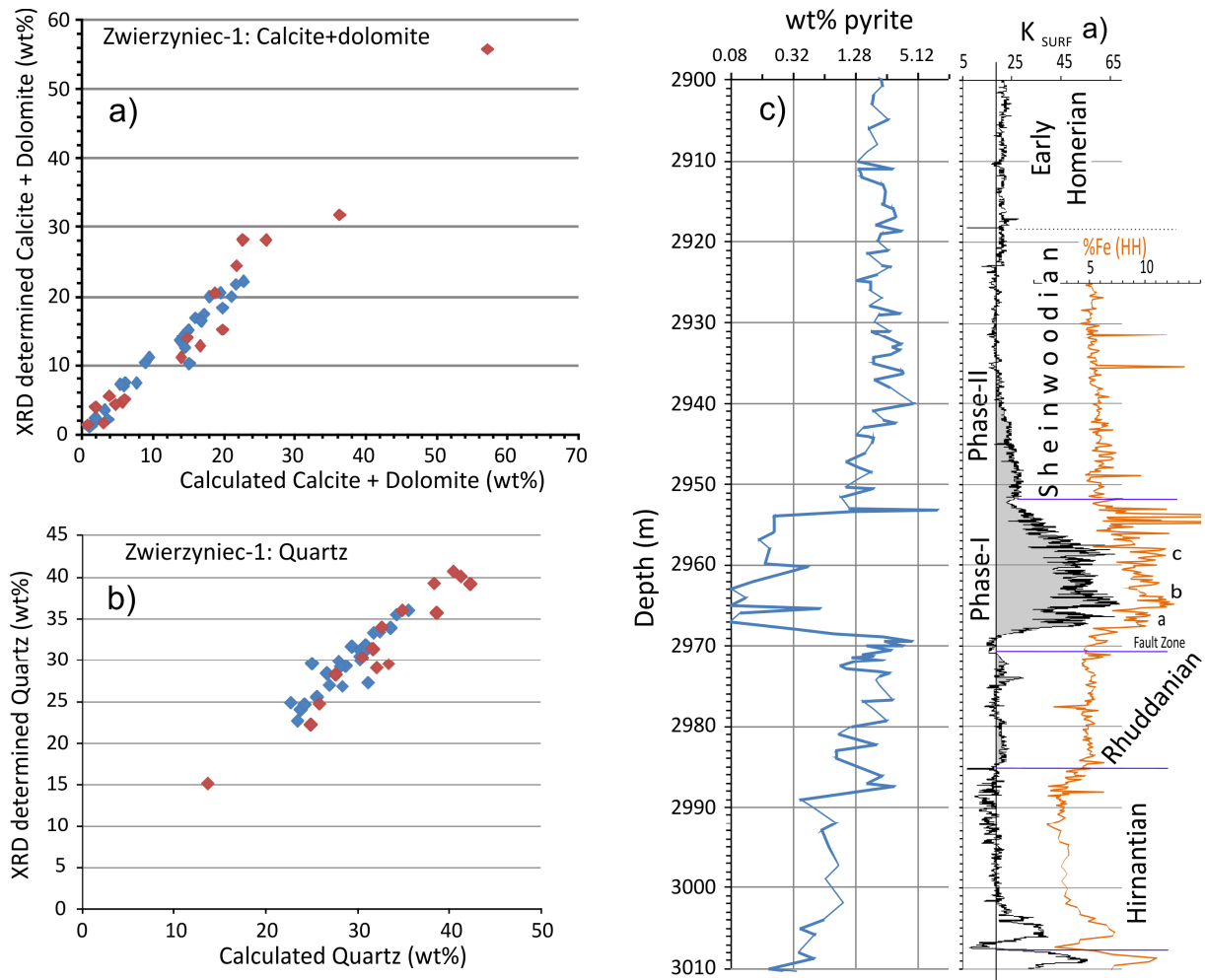


Fig. S4. Data for Zwierzyniec-1. Transfer functions for a) calcite+ dolomite ($R^2=0.964$), and b) quartz content ($R^2=0.898$). Using ICP-OES dataset of Sullivan et al. (2018). The different coloured symbols represent different laboratories used for quantitative XRD determination.

C) The MINLITH (Rosen et al. 2004) determined pyrite content, which is largely based on the ICP-OES sulphur content, shown against the portable XRF %Fe and K_{surf} values.

2. Threshold plots for redox proxies

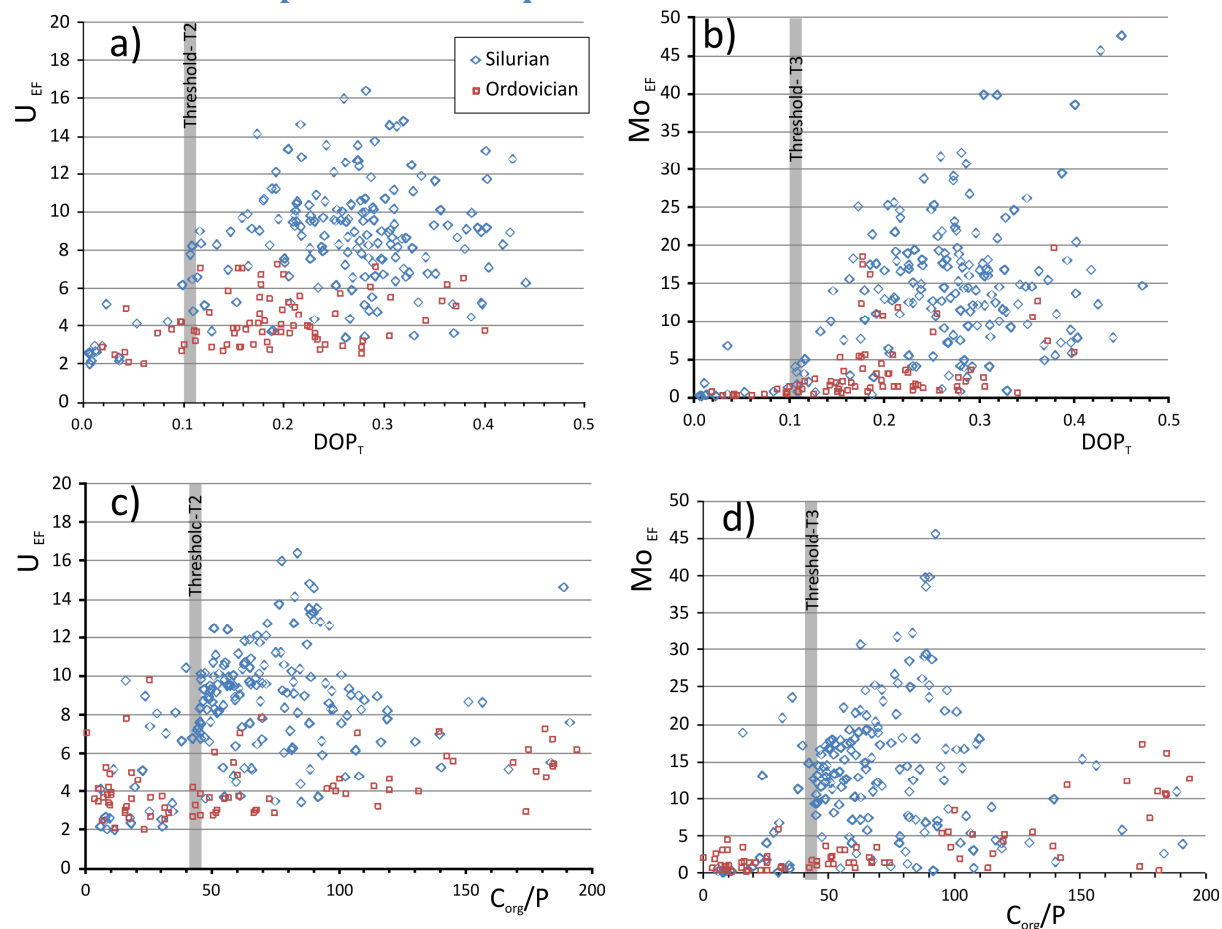


Fig. S5. Following the redox threshold protocol proposed by Algeo & Li (2020), these show the bi-plots of trace element enrichment factors (U_{EF} , Mo_{EF}) against the redox parameters DOP_{T} (degree of pyritisation) and C_{org}/P (P in wt%). Where, $DOP_{\text{T}} = \{S_{\text{T}} \cdot (55:85/64:12) \cdot Fe_{\text{T}}\}$, and S_{T} and Fe_{T} are the total sulphur and iron in wt% (of the ICP-OES data of Sullivan et al. 2018). The inferred thresholds for the T2 and T3 redox transitions (see Algeo & Li, 2020), are indicated in grey. Enrichment factors normalised to PAAS values from Tribouillard et al. (2006).

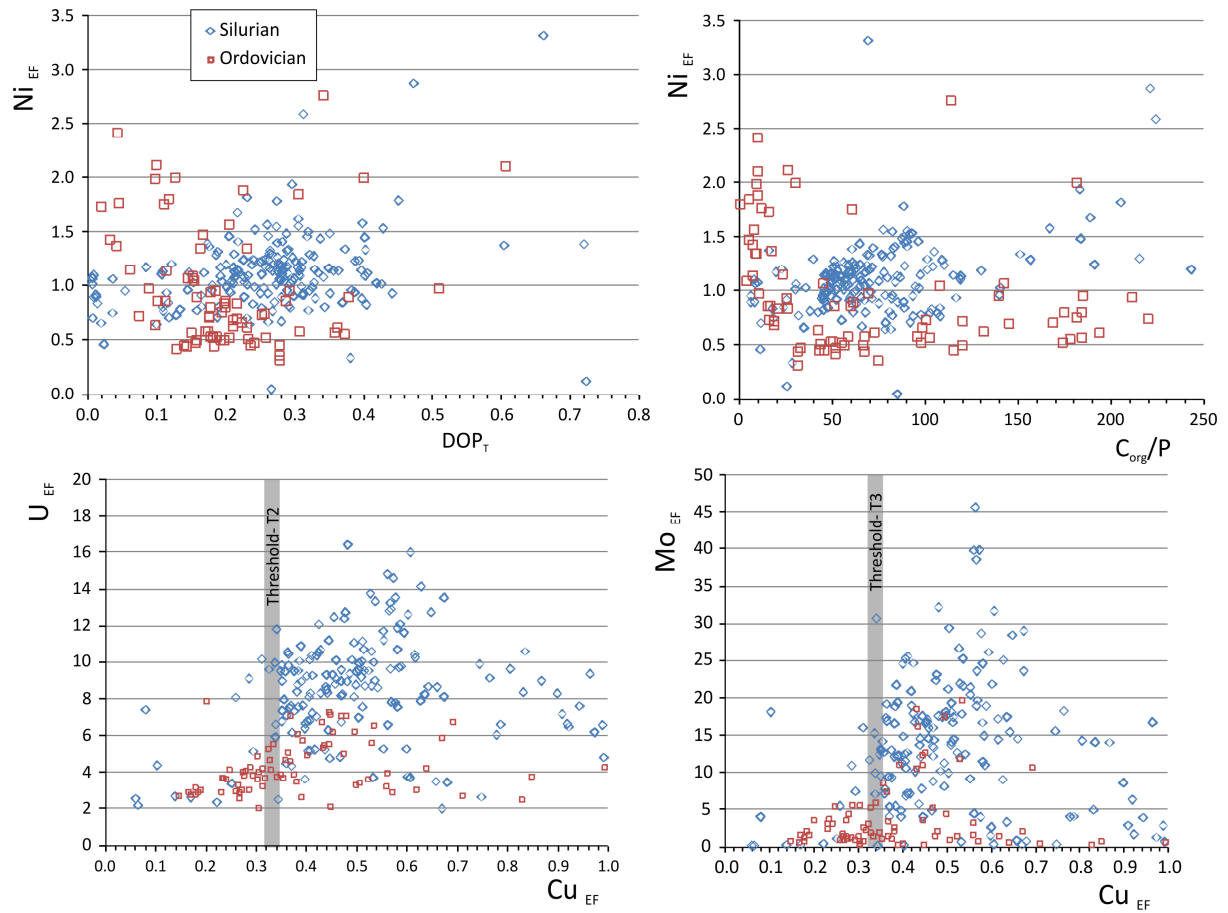


Fig. S6. Following the protocol proposed by Algeo & Li (2020), these show the bi-plots of trace element enrichment factors U_{EF} , Mo_{EF} and Ni_{EF} . See Fig. S5 for details. Ni_{EF} does not show a clear threshold.

3. The rare earth element (REE) data in Zwierzyniec-1

Y/Ho ratios (and Zr/Hf) indicate a detrital-clastic control on the REE patterns (Bau et al. 1997; Chen et al. 2015), with lower Y/Ho ratios due to larger Ho (and REE) content in the Al-rich samples (Figs. S7a, S7c), since Y is less correlated to Al_2O_3 than Ho. The ΣREE content also has a secondary relationship to the P_2O_5 content (Fig. S7b), since the most-phosphate enriched samples are also those with the largest REE content, although the relationship differs for the intervals with lower ΣREE (Fig. S7b).

The geometric average of the PAAS normalised REE patterns show a mild ‘mid-REE bulge’ (Fig. S7d), which has a number of possible interpretations (Haley et al. 2004; Yang et al. 2017). Here it is associated with mild phosphate-related, preferential mid-REE enrichment, expressed by the BSI index of Tostevin et al. (2016) (Figs. S7e,f).

Rare phosphatic fossils are known from the Polish Silurian (Bojanowski et al. 2019), but it seems likely the phosphate is of detrital origin (probably apatite, monazite) with significant diagenetic addition from phosphogenesis (peaks in ΣREE) focussed particularly on three intervals at 2954.0 m (mid Telychian, lower *O. spirilis* Biozone?), 2969.15 m in the late Aeronian (*P. leptotheca* Biozone), and 3005 m in the Hirnantian (main text Fig. 7g,h). The bulk of the REE data are similar to the total REE and mid REE enrichment in average upper continental crust (Rudnick & Gao 2003) and PAAS (Fig. S7e). The relative diagenetic enrichment in phosphate is probably expressed by $\% \text{P}_2\text{O}_5/\text{Al}_2\text{O}_3$, and the Silurian intervals of enrichment are similar in magnitude (and mid-REE enrichment, shown by BSI), to the middle and upper Hirnantian (main text Fig. 7h). Normalising the ΣREE by Al, also shows also highs in the same intervals as the $\% \text{P}_2\text{O}_5/\text{Al}_2\text{O}_3$ highs, which are likely indicative of enhanced diagenetic phosphate in the suboxic intervals in the core. The REE patterns show very similar Eu/Eu*, BSI (Fig. S7f) and heavy and light REE contents to other Cambrian- Ordovician (whole-rock) phosphates (Eu/Eu* uses formulation in Ling et al. 2013). That is a trend to higher BSI and Eu/Eu* away from the ‘UCC/PAAS-like signal’ for those with the largest ΣREE . This is inferred to be a diagenetic signal with a number of possible origins (Sheilds & Stile 2001; Sheilds & Webb 2004; Chen et al. 2015; Yang et al. 2017).

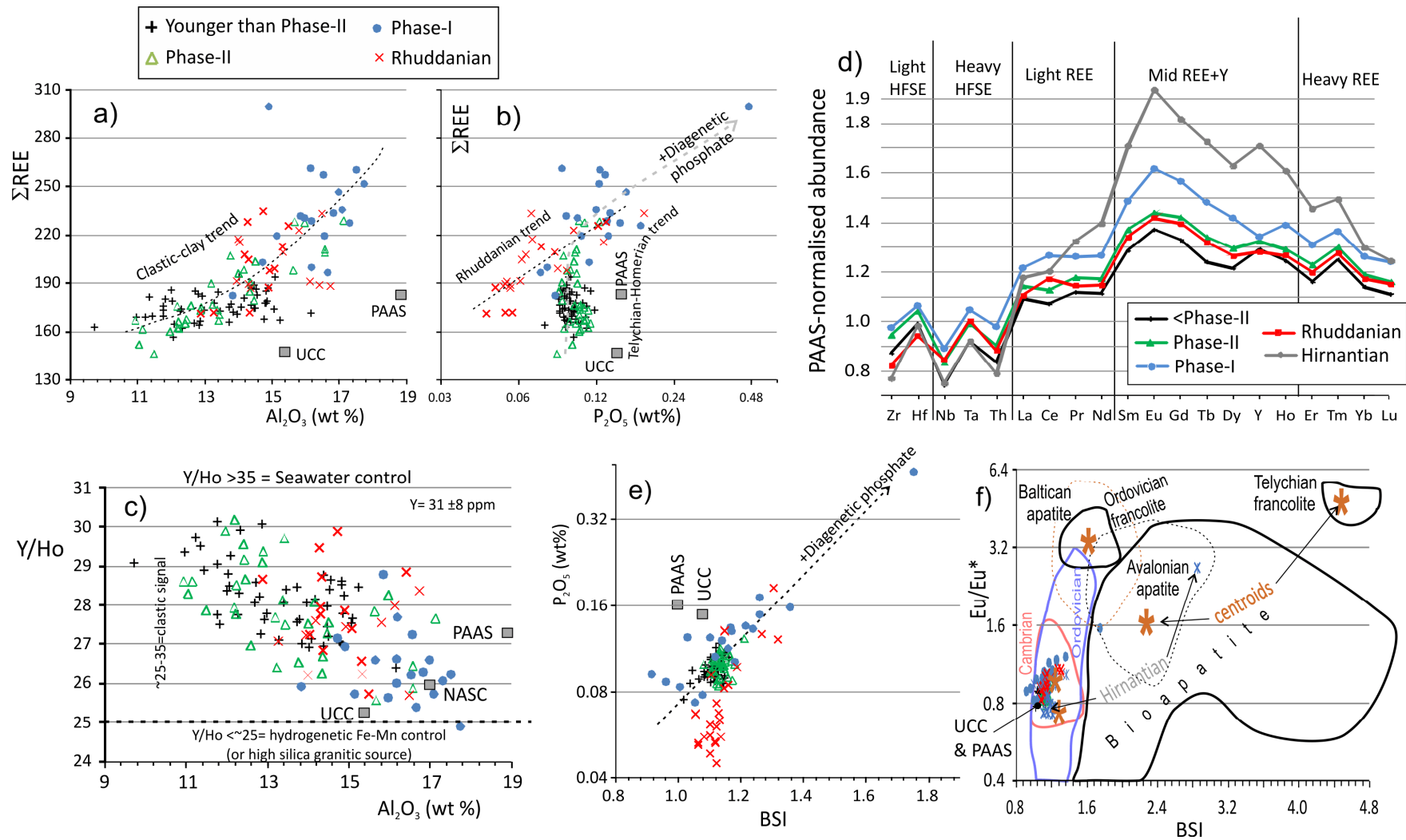


Fig. S7. REE data for Zwierzyniec-1. Key which applies to a), b), c), e), f) is at the top left. Data envelopes shown in f) from Emsbo et al. (2015), Zhang et al. (2016), Ray et al. (2011), Batchelor & Jeppsson (1999), Batchelor & Clarkson (1993), Ray (2007), Batchelor et al. (1995), Ray et al. (2013). The 'dotted' Baltican and Avalonian envelopes are apatites from volcanic ashes, other envelopes are sedimentary phosphates.

4. Trace element provenance discrimination using the East European Craton database

A database of whole rock geochemical data were compiled from the references indicated in Table S1, using a geographic separation of basement segments into east Sarmatia, West Sarmatia and southern Svecofennian basement. The number of geochemical records for each region and rock category are indicated in Table S2. As can be seen the records available are strongly biased to igneous datasets with limited metasediment data from western Sarmatia and southern Svecofennian basement.

Area	Rock Type [n]	Reference Sources
West Sarmatia	Igneous	Gurov et al. (1998), Dubyna et al. (2014), Duchesne et al. (2017), Liivamägi et al. (2018), Shnyukov et al. (2018), Shumlyanskyy (2014), Shumlyanskyy et al. (2016).
East Sarmatia	Igneous	Lobach-Zhuchenko et al. (2014a), Savko et al. (2019), Terentiev et al. (2016a,b, 2017, 2018,2020), Terentiev & Santosh (2016), Terentiev & Savko (2016).
South Svecofennian	Igneous	Åhäll et al. (2002), Baginski et al. (2001), Dorr et al. (2002), Mansfeld (1996), Skridlaitė et al. (2003, 2007), Soesoo et al. (2006), Sundblad et al. (1994), Wiszniewska et al. (2002, 2007).
West Sarmatia	Metamorphic	Bibikova et al. (2010, 2012, 2013), Gurov et al. (1998), Lobach-Zhuchenko et al. (2017).
East Sarmatia	Metamorphic	Lobach-Zhuchenko et al. (2014b), Terentiev & Santosh (2016).
South Svecofennian	Metamorphic	Krzemińska et al. (2005), Skridlaitė et al. (2008), Soesoo et al. (2006), Williams et al. (2009), Wiszniewska et al. (2007),

Table S1. Sources used in the geochemical database. Not all the sources contain all the trace elements used in the element ratios.

In order to better understand the petrogenetic relationship of the trace element ratios, the major element parameters of the modified alkali index (MALI), the total Fe-index [$\text{FeO}_{\text{tot}}/(\text{FeO}_{\text{tot}} + \text{MgO})$], indicated as Fe* and the aluminium - saturation index [ASI; molecular $\text{Al}/(\text{Ca} - 1.67*\text{P} + \text{N} + \text{K})$] as used in Frost et al. (2001) and Frost & Frost (2008). In addition two other compositional parameters were determined, the alkali index [AI, molecular $(\text{K}+\text{Na})/\text{Al}$] and Rittmann Serial Index [RSI; $(\text{Na}_2\text{O} + \text{K}_2\text{O})^2/(\text{SiO}_2 - 43.0\%)$] (Yang 2007). The Spearman correlation coefficients between these parameters and the element ratios is shown in Table S3. Since, these parameters are genetic indicators for igneous rocks, also included are some of the main oxides which may be more relevant for metamorphic rocks.

Region	Type	Ga/Sc:	10*Sc/Cr:	25*TiO ₂ /Nb	0.1*Zr/Nb	0.1*Zr/Sc	N
East Sarmatia	Igneous	0.69	1.66	2.08	2.18	0.63	515
	Meta-igneous	-	-	2.03	1.35	-	5
	metasediment	0.74	2.99	2.12	2.17	0.55	92
West Sarmatia	Igneous	0.84	4.23	2.70	1.32	0.83	181
	Meta-igneous	0.90	2.78	3.53	1.79	0.96	23
	metasediment	4.09	0.69	2.42	2.02	1.85	16
Southern Svecofennian	Igneous	1.80	2.47	1.68	2.29	1.52	140
	Meta-igneous	-	-	3.09	1.24	0.11	31
	metasediment	-	1.28	1.58	1.68	0.53	14

Table S2. Medians of key trace element ratios, and number of records (N) corresponding to each geographic and rock category. Note; the number used in each median may be \leq N, due to incomplete geochemistry data.

Dataset	Index	Ga/Sc:	10*Sc/Cr:	25*TiO ₂ /Nb	0.1*Zr/Nb	0.1*Zr/Sc
Igneous	AI	0.45	-0.14	-0.74	-0.08	0.58
	Al ₂ O ₃	0.11	0.32	0.20	0.12	0.08
	ASI	-0.02	0.25	0.14	0.14	-0.03
	Fe*	0.56	0.57	-0.31	-0.22	0.56
	K ₂ O	0.46	-0.03	-0.66	-0.02	0.59
	MALI	0.51	0.05	-0.75	-0.04	0.62
	RSI	0.47	0.18	-0.27	-0.16	0.46
	SiO ₂	0.26	-0.04	-0.67	0.17	0.35
Metamorphic	AI	0.26	0.07	-0.43	0.21	0.08
	Al ₂ O ₃	0.51	0.30	0.17	-0.31	-0.27
	ASI	0.15	0.02	-0.09	0.24	-0.17
	Fe*	0.02	0.24	-0.18	0.05	-0.12
	K ₂ O	0.55	0.12	-0.28	-0.05	-0.20
	MALI	0.50	0.25	0.01	-0.08	-0.14
	RSI	0.58	0.30	-0.11	-0.12	-0.01
	SiO ₂	-0.49	-0.17	-0.22	0.65	0.27

Table S3. Spearman correlation coefficients (R_s) between trace element ratios, genetic geochemical indicators and main oxides. The largest one or two correlation coefficients are indicated in bold for each element ratio.

In order to illustrate the relationships to the Zwierzyniec-1 data, the key relationships (the bold R_s values indicated in Table S3) between trace element ratios and the petrogenetic indexes, from information in the database are shown in Figs. S8 to S13. Each of the trace element ratios is discussed in more detail below.

4.1 General Comparisons

All the element ratios from Zwierzyniec-1 have a much more limited 2σ range than the element data in the database (shown as greyed intervals in the SI Figs. S8 to S13), indicating that the data from the core represents a considerably-averaged and homogenised representation of the likely source rocks. Of course this feature is typical for shale-mudstone

successions in general (Condie 1991; McLennan 2001). This suggests the changes in trace element ratios from the core, as represented by the provenance zones and subzones, represent relatively small differences in sediment provenance.

4.2. Sc/Cr ratio (Fig. S8)

The largest provenance changes is between the PZ1 and PZ2 zones with a transition around the Aeronian- Telychian boundary, shown mostly by $10^*Sc/Cr < 1.5$ in PZ1 and mostly greater than 1.5 in PZ2, connected to a major reduction in Cr content in PZ2 (main Fig. 9e). For the igneous dataset the largest R_s is between Sc/Cr and Fe* (in both east and west Sarmatia datasets; Fig. S8). A value of $10^*Sc/Cr < 1.5$ and $Fe^* < 0.55$ neatly divides the igneous datasets (Fig. S8a, S8c), with most west Sarmatian igneous rocks having larger Sc/Cr due to larger Fe*. Those data with $10^*Sc/Cr < 1.5$ belong to Paleoproterozoic basic and intermediate igneous rocks from eastern Sarmatia of Terentiev et al. (2016b), Terentiev & Santosh (2016), Terentiev & Savko (2016) or mafic bodies and dykes from western Sarmatia (dated around 1.8 - 2.4 Ga in the Paleoproterozoic) (Bogdanova et al. 2013; Shumlyanskyy et al. 2016). A few gabbro samples from 1.8 Ga Svecofennian crust also have this Sc/Cr signature (Åhäll et al. 2002). In modern basalts Cr content is positively related to $(1-Fe^*)$ where olivine is the principal Cr-bearing silicate, although Cr also has large partition coefficients for clinopyroxene and spinels (Doe 1997).

Conversely in western Sarmatia metamorphic rocks with Archean protoliths (Bibikova et al. 2010; 2012; 2013) have $10^*Sc/Cr < 1.5$ (Fig. S8d). In contrast, Paleoproterozoic metasediments from eastern Sarmatia have mostly $10^*Sc/Cr > 1.5$ (Terentiev & Santosh 2016).

The change in the Sc/Cr ratio between PZ1 to PZ2 therefore suggests two possible scenarios: a) a change from PZ1 to PZ2, between magnesian to more ferroan type (basic and intermediate) igneous rock sources (from both west and east Sarmatia), or; B) rather more western Sarmatia Archean metasediment sources in PZ1 and east Sarmatia Paleoproterozoic metasediment sources in PZ2 (i.e. Fig. S8d). The Sc/Cr ratio also varies significantly through the PZ1 and PZ2 zones, with largest Sc/Cr being during the M₁ subzone, and the average next largest Sc/Cr ratio during the M₂ subzones. Along with Ga/Sc this ratio helps define the M₂-W₁ subzone boundary. The lowest Sc/Cr ratio is during subzone A (Fig. S10).

4.3. Zr/Sc ratio (Figs. S9)

The largest change in Zr/Sc is between the M₁ and M₂ subzones, with the M₂ to W₁ to W₂ subzone interval having similar Zr/Sc ratios. The M₁ and M₂ transition occurs at a $0.1^*Zr/Sc$ value of 1.1. The M₁ and H subzones have similar $0.1^*Zr/Sc$ ratios, intermediate between values for the R₁ and R₂ subzones (Fig. S10).

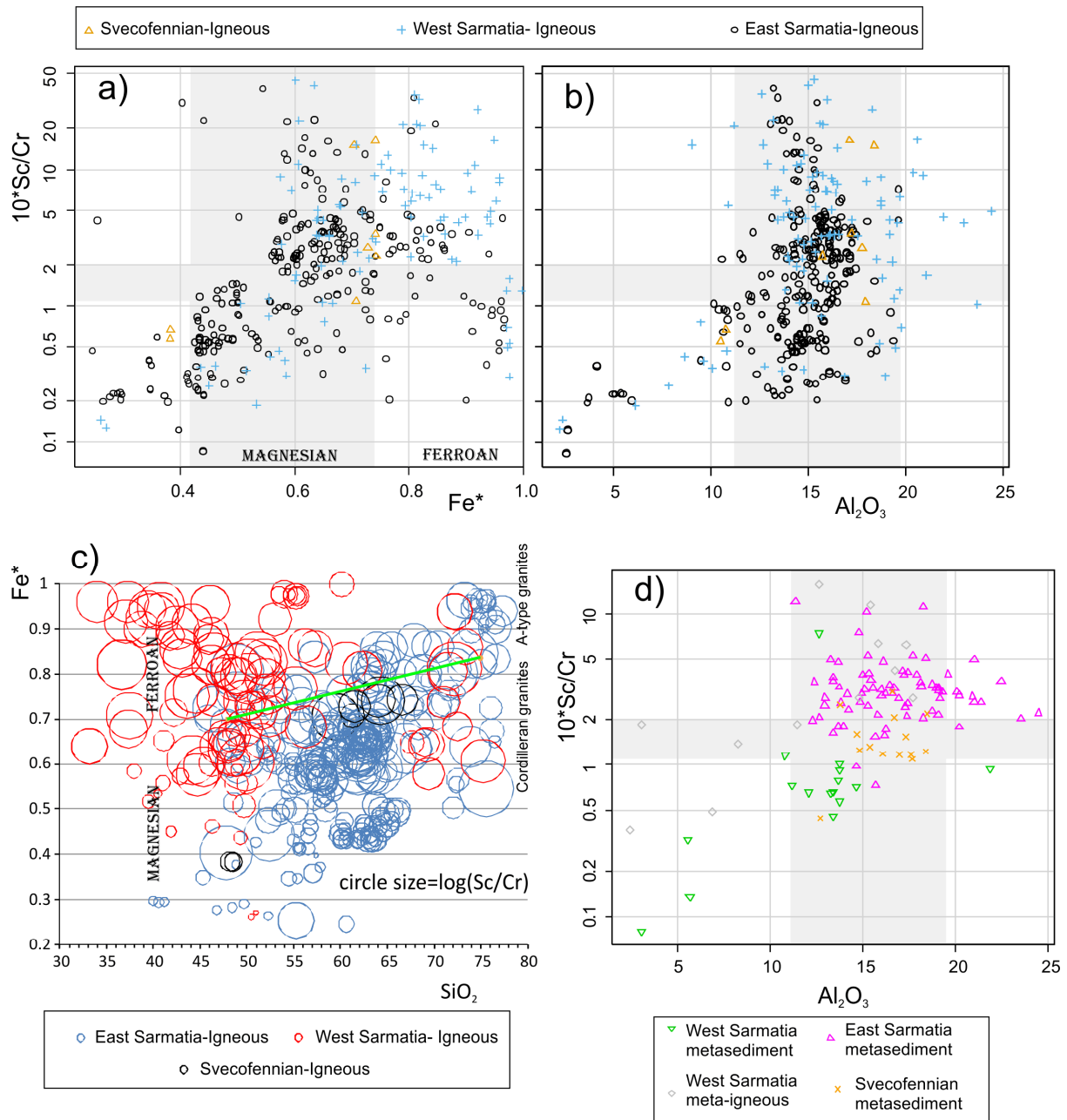


Fig. S8. a) to c) The EEC data for Sc/Cr from igneous rocks, and d) for metamorphic rocks; plotted against, Fe^* , Al_2O_3 and SiO_2 . The Fe^* is the petrogenetic indicator of Frost & Frost (2008) and their magesian and ferroan fields are marked on c) with the separating line shown in green. The grey bands in a), b) and d) represent the 2σ range of the values in the Zwierzyniec-1 core (2900- 3010 m). i.e. their central ‘crossing window’ represents a box around the range in the core. The diameter of the circles in c) represents the size of the log transformed Sc/Cr ratio.

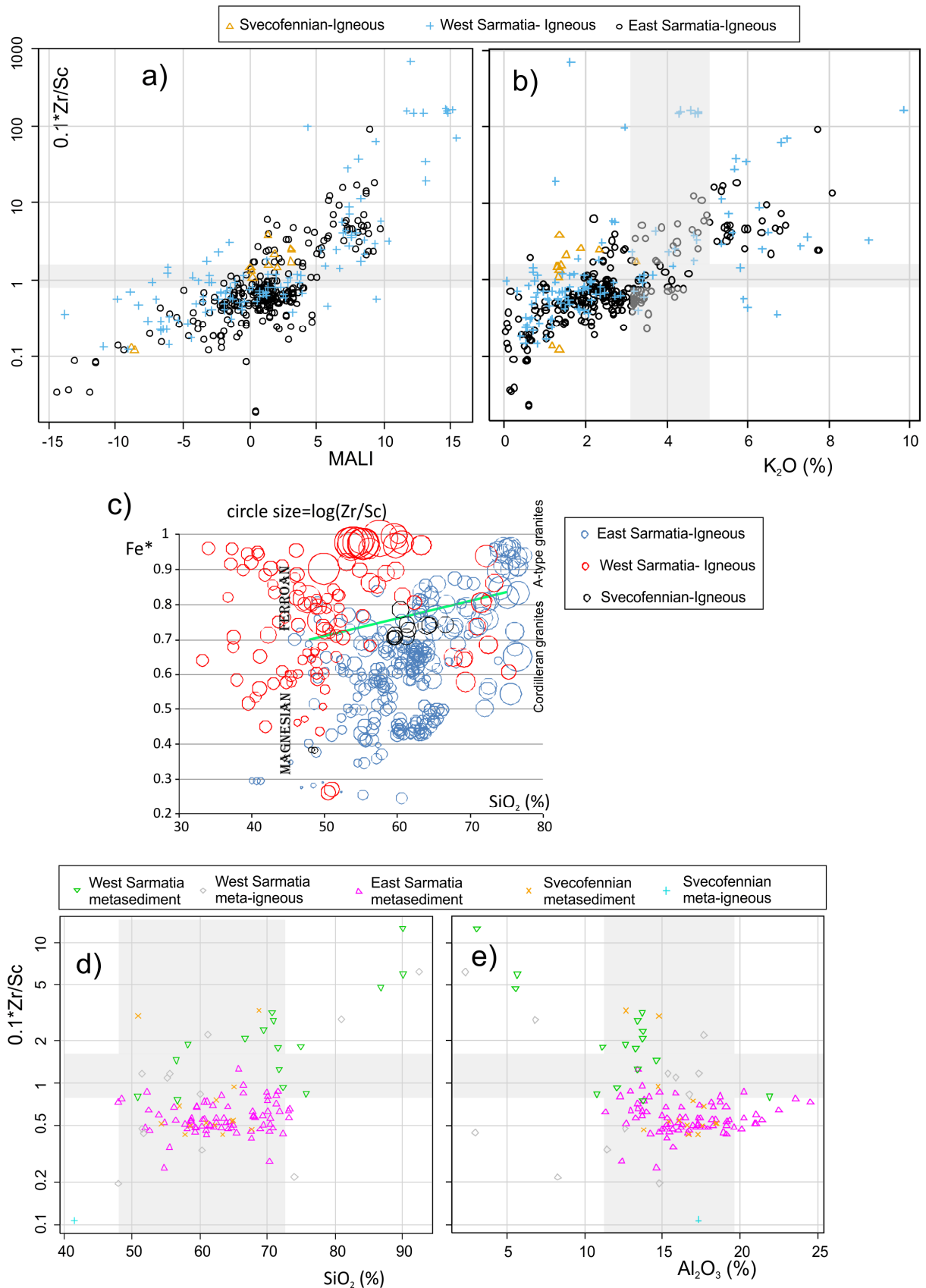


Fig. S9. a) to c) The EEC data for Zr/Sc from igneous rocks and d), e) for metamorphic rocks plotted against MALI, K_2O , Fe^* , Al_2O_3 and SiO_2 . MALI=modified alkali-lime index (Frost & Frost 2008). See Fig. S8 for details.

However, the data from Zwierzyniec-1 plots along the compositional trend of the Sarmatian-Svecofennian igneous source rocks (Fig. S14a), and that for the metamorphic rocks (Fig. S14b). Zircon detrital concentration is usually shown by a deflection to larger Zr/Sc at Th/Sc ratios larger than 1 (Ortis & Roscher 2006), which is not shown in the Zwierzyniec-1 data, suggesting zircon detrital concentration is not an important factor in changing the Zr/Sc ratio (Fig. S14). The bulk of the Zwierzyniec-1 data has Th/Sc <1 with only a few samples from the interval younger than Phase-II having Th/Sc >1. A change in the Th/Sc ratio at the PZ1 to PZ2 boundary is also evident (Fig. S10) coincident with the major switch in Sc/Cr (see Fig. S10, main text Fig. 11e).

The key switch to larger Zr/Sc ratios occurs in the younger part of the M₁ subzone, and remains similar in the whole younger interval. Two possible scenarios for this change are: a) a change to more alkalic igneous rocks sources (Fig S9a, b) also likely richer in SiO₂ (Fig. S9c) for the interval younger than M₁, or; b) a greater contribution from west Sarmatian metasediments in the younger interval, that have the more elevated Zr/Sc (Fig. S9d) and Th/Sc values (Figs. S10, S14b).

4.4 Ga/Sc ratio (Fig. S11)

The Ga/Sc ratio is largest (> ca. 1.3) in the W₁ subzone, but this is superimposed on a progressive upwards increase in Ga/Sc from a low of ~1.0 in the R₂ subzone (Fig. S10). Ga/Sc shows a strong relationship to MALI and Fe* (Figs. S11a,b), which is controlled by the well known relationship of Ga and Sc to differentiation, since alkaline rocks show increased concentration of Ga with differentiation and Sc shows decreased contents with increasing differentiation for alkaline and sub-alkaline igneous rocks (Winchester and Floyd 1977). The igneous database has largest Ga/Sc for >70% SiO₂, MALI > ~5, and lowest ratios for Fe * <0.45 (Fig. S11). For the metasediment dataset Ga/Sc is positively related to K₂O (Fig. S11e) and RSI (but data few) and negatively to SiO₂. However, the bulk of the Zwierzyniec-1 data fall above the east Sarmatia metasediment data (Fig. S11e), and the sparse west Sarmatia data fall at or above the range in the core. In the Zwierzyniec-1 data the Ga/Sc shift at the top of the M₁ subzone to values >1.1 corresponds approximately to Ga/Sc >1 (at ~ 0.6 Fe* and MALI ~ 0) in the igneous dataset (Figs. S10, S11a,b). The largest Ga/Sc values are from 1.7 - 2.1 Ga syenites, anorthosites and rapakivi granites (Dubyna et al. 2014; Shnyukov et al. 2018) and 2.6 Ga high-silica rhyolites and granites (Savko et al. 2019).

A possible scenario for the increase in Ga/Sc from the R₂ to W₁ subzones is a progressive younging-change to more silic igneous source rocks (Fig. S11c), poorer in K₂O content- since the K₂O content declines over this interval in the Zwierzyniec-1 core (main text Fig. 9b). Although the data are sparse for metasediment sources (Fig. S11e), it is possible an alternative scenario may be more western Sarmatian metasediment sources.

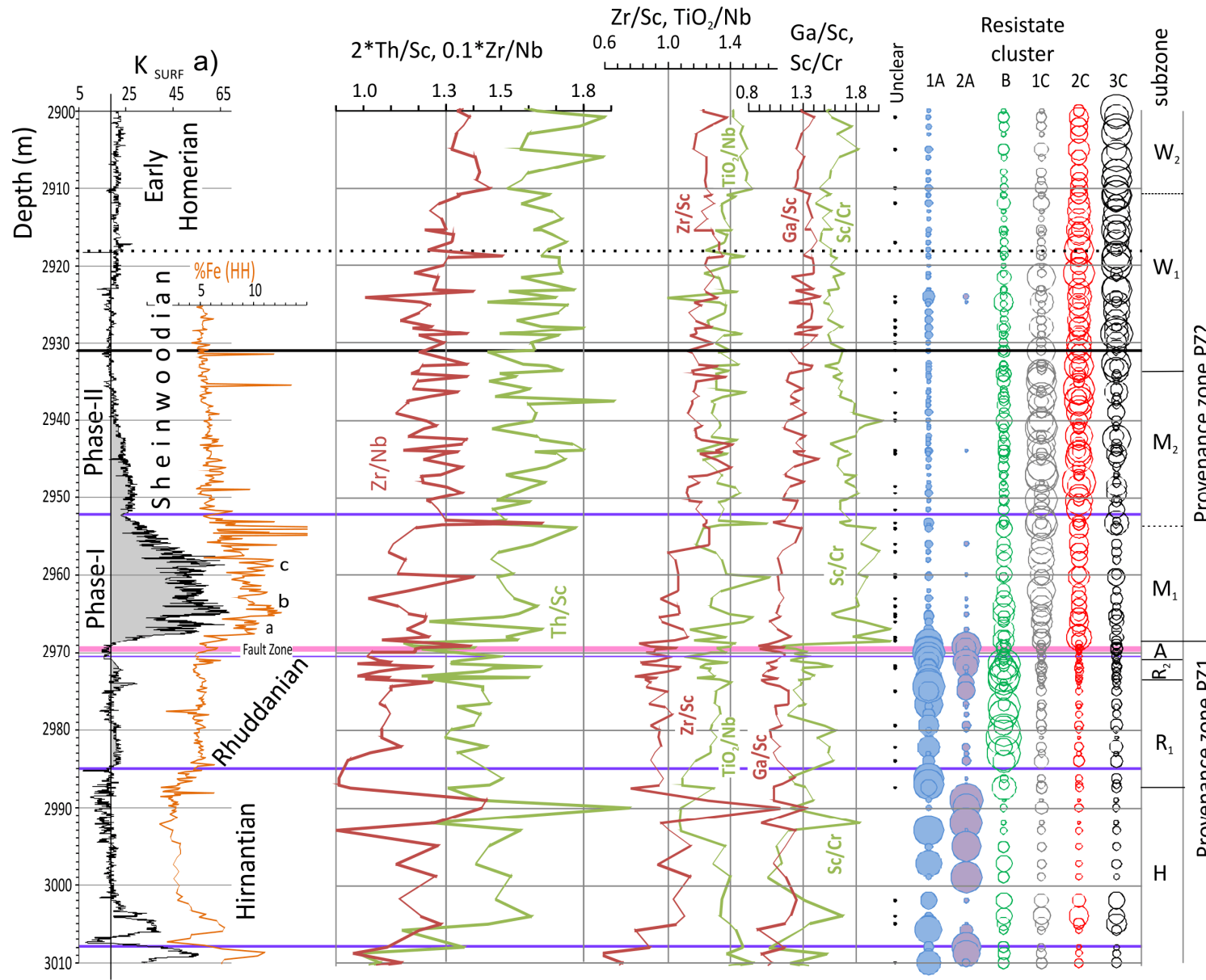


Fig. S10. A plot like Fig. 10 in main text, but showing all the trace element ratios investigated and used in the provenance evaluation.

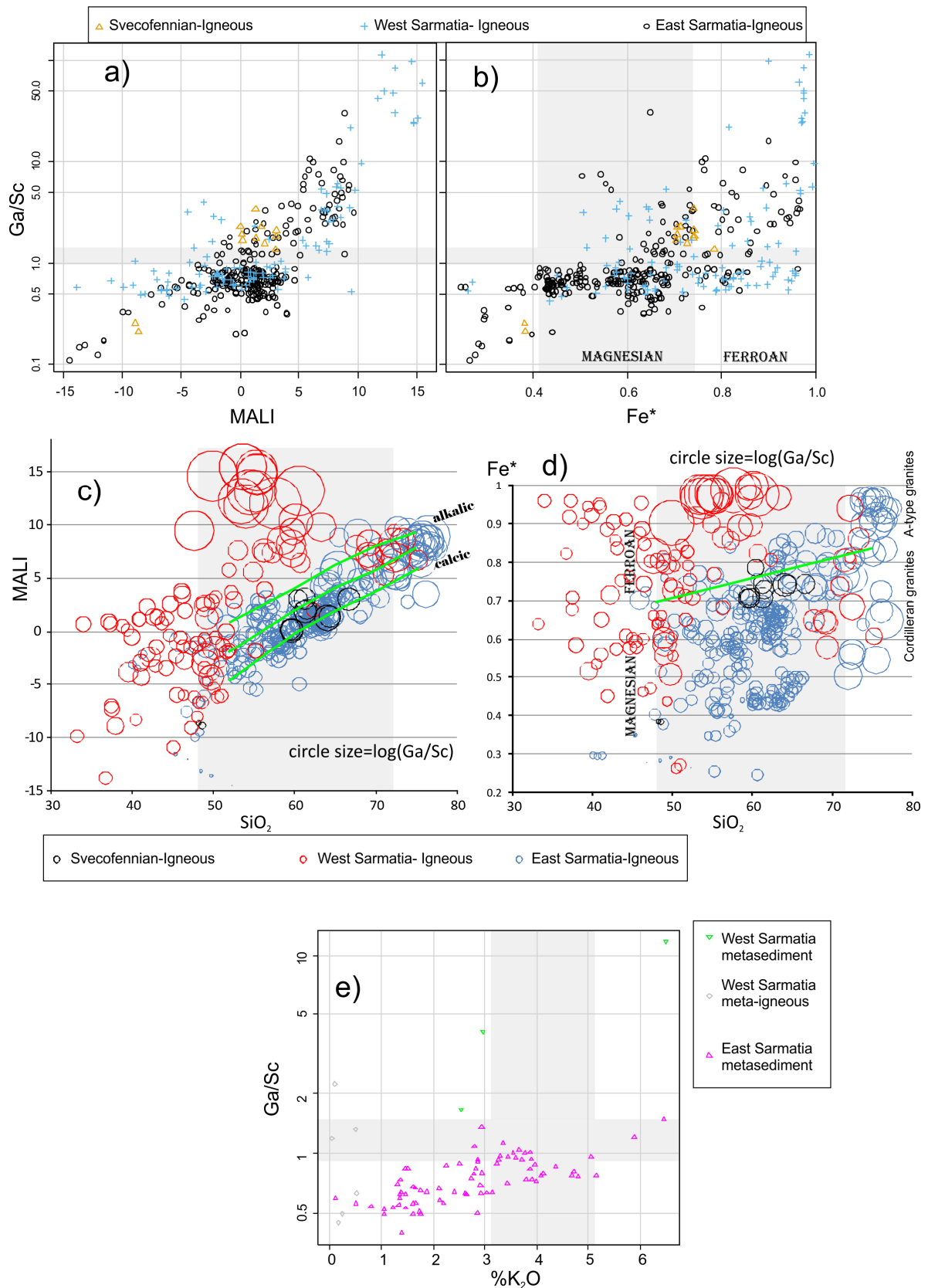


Fig. S11. The EEC data for Ga/Sc from igneous rocks a) to d) and e) for metamorphic rocks plotted against MALI, Fe*, SiO₂ and K₂O. See Figs. S8, S9 for details. Calcic and alkalic lines in c) from Frost & Frost (2008).

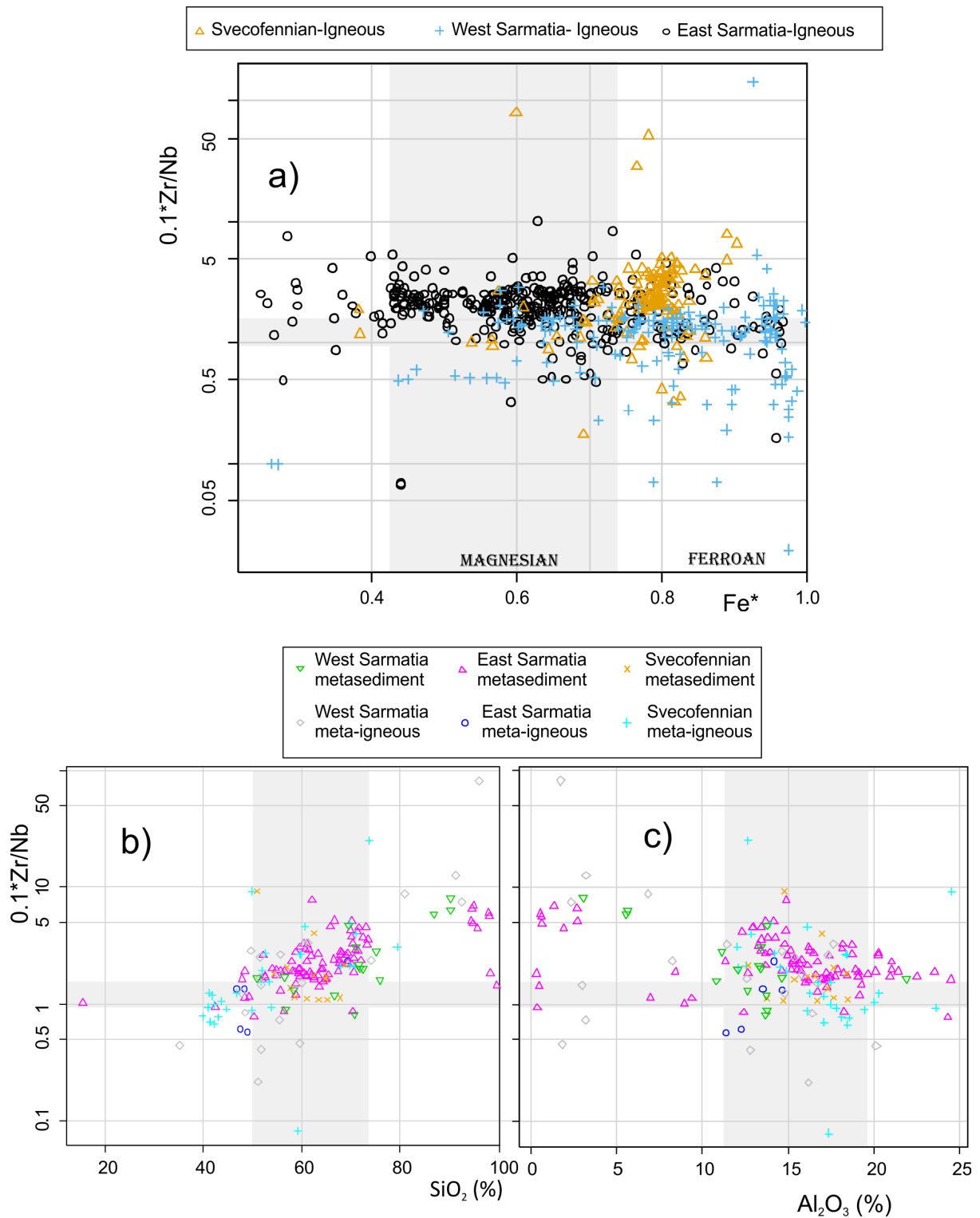


Fig. S12. The EEC data for Zr/Nb from igneous rocks a); and b), c) for metamorphic rocks plotted against Fe^* , SiO_2 and Al_2O_3 . See Figs. S8, S9 for details.

4.5 Zr/Nb ratio (Fig. S12)

The Zr/Nb ratio is largest in the W_2 subzone, similar during the underlying M_1 , W_1 and H subzones, but lowest for the R_1 and R_2 subzones (Fig. S10).

The Zr/Nb ratio seems to have little petrological significance for the Sarmatian-Svecofennian igneous rocks, with little relationship to alkali, silica or Fe* indices (Table S3). However, on average the Zr/Nb ratio appears to distinguish west and east Sarmatia igneous sources (average $0.1 \cdot \text{Zr/Nb}$ of 1.3 and 2.2 respectively; Table S2). The west Sarmatia data sources with low (<0.5) $0.1 \cdot \text{Zr/Nb}$ are largely from 1.7 - 2.1 Ga alkali and nepheline syenites (Dubyna et al. 2014). Svecofennian averages are similar to east Sarmatia sources. The Zr/Nb ratio has been inferred to be useful for distinguishing various kinds of basalts (Pearce & Norry 1979; Snow 2006), mainly due to the Nb content being sensitive to mantle depletion and enrichment processes (Meschede 1986), as such it may be useful for distinguishing basaltic magma sourced from differing parts of the mantle (Condie 2005), along with use in discriminating some kinds of granites (Pearce et al. 1984). If Zr/Nb is responding in this manner, it may be indicative of sediment sources with differing mantle regions for east and west Sarmatian igneous rocks.

In the datasets the strongest relationship (Table S3) is with SiO_2 (Fig. S12b) for both metasediments and meta-igneous, so it appears this may be a good metamorphic silica indicator.

Therefore possible scenarios for the increase in $0.1 \cdot \text{Zr/Nb}$ from low values in the R_1+R_2 subzones (~ 1.05) to higher values (~ 1.35) in the W_2 subzone may be: a) increasing contributions (in W_2) from eastern Sarmatia crust, or b) increasing contributions from silica enriched metasediments (sourced throughout the EEC).

4.6. $25 \cdot \text{TiO}_2/\text{Nb}$ ratio (Fig. S13)

The TiO_2/Nb ratio has high values (~ 1.46) in the W_2 subzone with lower values in the R_1 , R_2 and upper part of the H subzones (~ 1.29), with most of the remaining intervals having similar values (~ 1.33). This ratio is important for defining the W_2 subzone (Fig. S10). The Zwierzyniec-1, 2σ range of this ratio is a small part of the total range in the possible source rocks (Fig. S13), and is the noisiest (SCF = 0.38) of the provenance indicators used, so it is probably most indicative of changes into the W_2 subzone.

For the igneous dataset $25 \cdot \text{TiO}_2/\text{Nb}$ has strong negative correlations to MALI and AI (and SiO_2 ; Fig S13a,b,c), with values <0.2 values from Dubyna et al. (2014); Shnyukov et al. (2018); and Savko et al. (2019). In the metamorphic dataset, TiO_2/Nb is has the largest negative correlations with the AI index, influenced by quartzites from east Sarmatia with AI values >1 from Lobach-Zhuchenko et al. (2014b) and meta-igneous rocks with $25 \cdot \text{TiO}_2/\text{Nb} >4$ (Fig. S13d). Hill et al. (2000) suggested Ti/Nb is rather less sensitive to source weathering than when Ti is ratioed to Y or Zr, and also likely less impacted by sediment sorting (Garcia et al. 1994).

Possible scenarios for the increase in TiO_2/Nb from low values in the R_1+R_2 , and late H subzones (~ 1.29) to higher values (~ 1.35) in the W_2 subzone may be: a) Increased

contributions from more calcic or basic igneous sources in subzone W₂, or b) greater contributions from silica-poor metasediments in W₂. These may be connected if metamorphic sources were richer in meta-basic rocks.

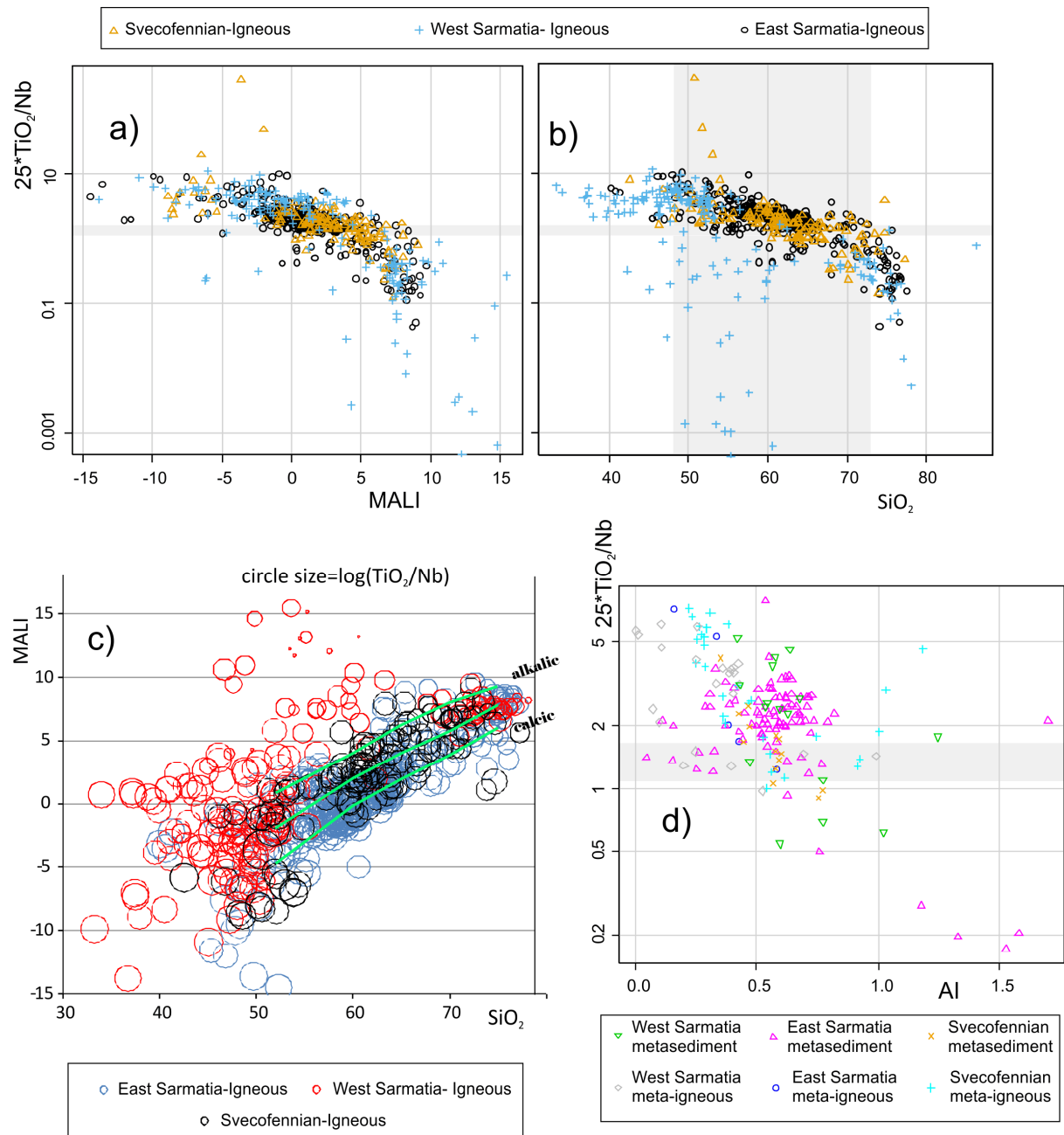


Fig. S13. The EEC data for TiO_2/Nb from igneous rocks a) to c), d) for metamorphic rocks plotted against MALI, SiO_2 and the alkalinity index (AI). See Figs. S8, S9 for details. Calcic and alkalic lines in c) from Frost & Frost (2008).

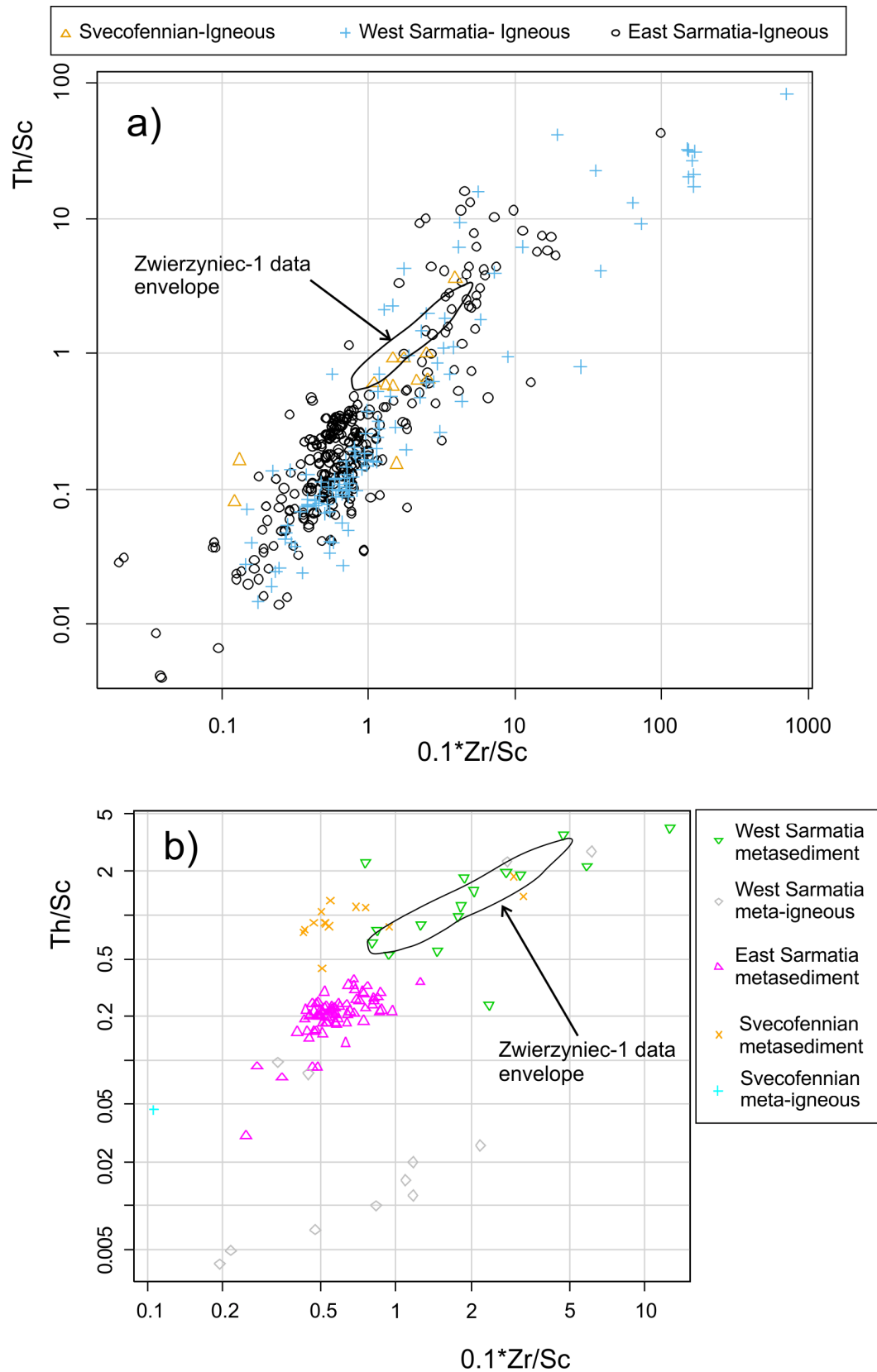


Fig. S14. The EEC data for Th/Sc from a) igneous rocks b) for metamorphic rocks plotted against Zr/Sc. The data envelope for the Zwierzyniec-1 dataset (2900-3010 m) is shown; most of the samples from the core have Th/Sc < 1 within these envelopes.

4.7 Provenance Synthesis

It is not possible with this dataset to fully unravel the likely spatial and source rock contributions to the provenance differences, expressed by the provenance sub-zones. However, some inferences can be made (Fig. S15).

- a) Some of the scenarios based on individual element ratios may be unlikely in that they do not marry with scenarios expressed by other element ratios. For example, for Zr/Nb ratios, expressing increase in silica-rich metasediments between R₁ to W₂ subzone does not marry with the converse relationship shown by Ti/Nb, indicating that probably the converse scenario (i.e. more E. Sarmatia crustal sources) for Zr/Nb may be the more likely (Fig. S15).
- b) Some element ratios in the cores show rather more progressive changes throughout the core (e.g. Ga/Sc; Fig. S10), whereas others such as Sc/Cr, Zr/Sc, Zr/Nb and Ti/Nb in parts have more step-like changes in ratios (Fig. S10). This indicates a mix of progressive and step-like changes in provenance.
- c) The key step changes occur at the boundary of the A-M₁ (Zr/Nb and Ti/Nb; Fig. S10), W₁-W₂ and M₁-M₂ boundaries. That at A-M₁ boundary may relate to a switch between magnesian-type to more ferroan igneous rocks sources or a switch between metamorphic Archean to more Palaeoproterozoic crust. That at the W₁-W₂ boundary may relate to a switch to more eastern Sarmatian or more basic (less silica) igneous or meta-igneous sources. That at the boundary between M₁-M₂ may be an upwards change to more silic igneous rocks, or increase in contribution of W. Sarmatian metasediments.

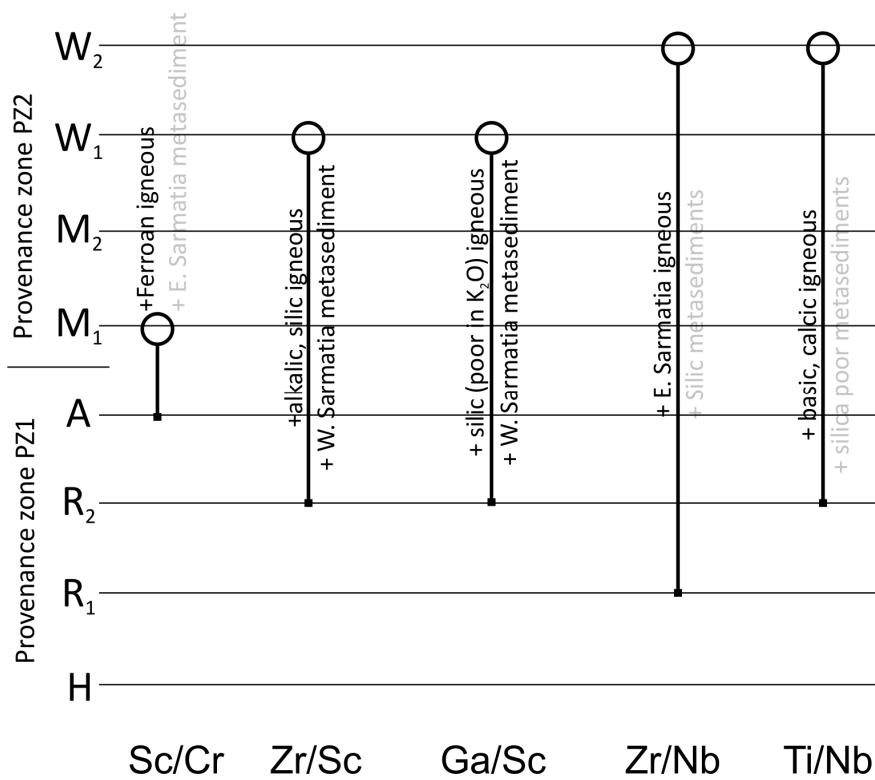


Fig. S15. Diagram summarising the likely changes in provenance as inferred from the trace element ratios, and the comparison to the EEC data. The left shows the provenance zones and subzones, and the ‘lollipops’ show where change starts and ends. The ‘+’ indicates an increase in this component, with possible igneous-related changes on the left of the lollipop and metamorphic-related on the right. Those in grey are considered unlikely based on the balance of evidence in these data.

5. Age-depth model, accumulation rate and flux for Zwierzyniec-1

To construct the age-depth model we use the Bayesian-based approach of Haslett & Parnell (2008) and Parnell et al. (2008). The radiometric date uncertainties are normally distributed values (σ_R , column A, in Table S4). Bchron uses procedures to deal with radiometric date outliers, which flags the tie point with a probability of being an outlier (P_{out} in Table S4). Uncertainties in the location of the biozone with respect to the depth scale (i.e. a tie points unknown position within the biozone) are handled as a ‘defined range’ (described as sample depth range in Parnell et al. 2008) in the depth scale, in which the date occurs ($\pm es$; column F, in Table S4), and treated as coming from a uniform distribution. In order to estimate this ‘defined range’ in depth (i.e. $\pm es$; meters), this uncertainty in Ma was estimated from the tie points likely position within the biozone, and converted to a Ma uncertainty estimate from the biozone-age scales in Melchin et al. (2012) and Cooper et al. (2012). This defined range is shown as column D in Table S4. In order to convert the defined range in Ma into depth meters (as required by Bchron), polynomials were fitted to the age (that in column A) to depth relationship in 4 segments (427.18 - 430.35 Ma; 431.50 - 432.9 Ma; 434.85 - 438.49 Ma; 438.49 - 445.5 Ma shown as coloured intervals in column A in Table S4. Note some overlapping). From the fitted polynomial equation, the defined range in Ma could be converted to a defined range in meters (i.e. $\pm es$) as shown in column F in Table S4. The final age model is shown in Fig. S16b.

Accumulation rates were determined by evaluating the gradient of the depth versus age relationship using the median line in Fig. S16b. This gradient evaluation used local regression and likelihood as implemented in the LOCFIT routines in R (Loader 1999). Both constant bandwidth smoothing and locally adaptive smoothing of the gradient were tested, and it was judged that constant bandwidth (using generalised cross validation for bandwidth selection) failed to give a suitable smoothed curve for accumulation rate (it was noisier than the linear fit in main text Fig. 12). The adaptive bandwidth method (using a localized version of Akaike’s information criteria) was superior and used a data point weighting equal to the width of the 95% HDR band. The smoothing function was 0.1 for the nearest neighbour and fixed fractions, with the penalty for the locally adaptive fit equal to the average halfwidth of the HDR band (i.e. 0.3 Ma).

In order to determine the flux (in $\text{g cm}^2 \text{ kyr}^{-1}$) an estimate of the dry bulk density was determined by a transfer function between the XRD-determine density estimates and the geochemistry of these samples, allowing mapping of density to other samples. Some outliers were filtered out first. The final relationship is shown in Fig. S17. This is superior to assuming average bulk density as in Schoeper et al. (2016).

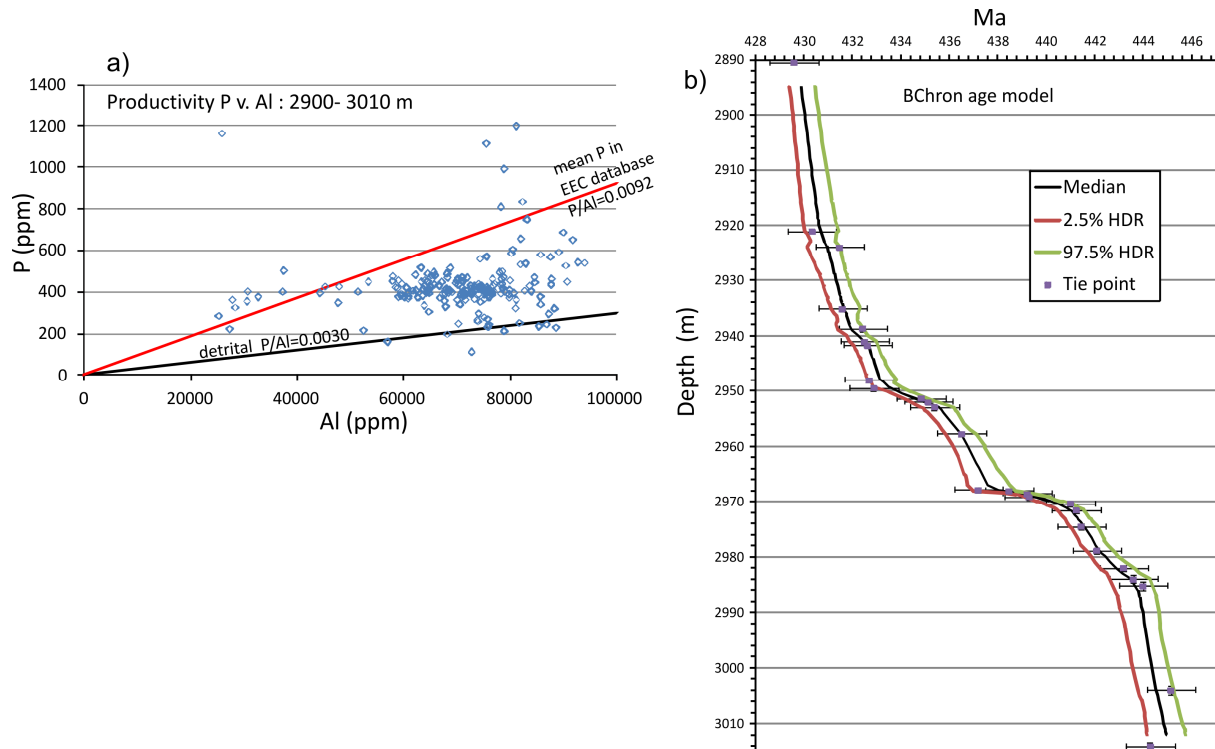


Fig. S16. a) Method of estimating the detrital P component in Zwierzyniec-1. The red line represents the average P/Al content in the EEC database, indicating the P-content in the core is much depleted in comparison to its likely EEC sources, probably due to loss to seawater during burial and diagenesis. $P_{XS} = P - P_{\text{detrital}}$ which is that used in the P-based productivity estimate. B) Bchron age-depth model for Zwierzyniec-1. The tie point ages have the x-axis error bars shown as σ_R (column A, Table S4) and the defined range (in meters on y-axis). The band between the 2.5% and 97.5% highest posterior density (HDR) lines is the 95% HDR confidence interval in the age model. The median is the final age model.

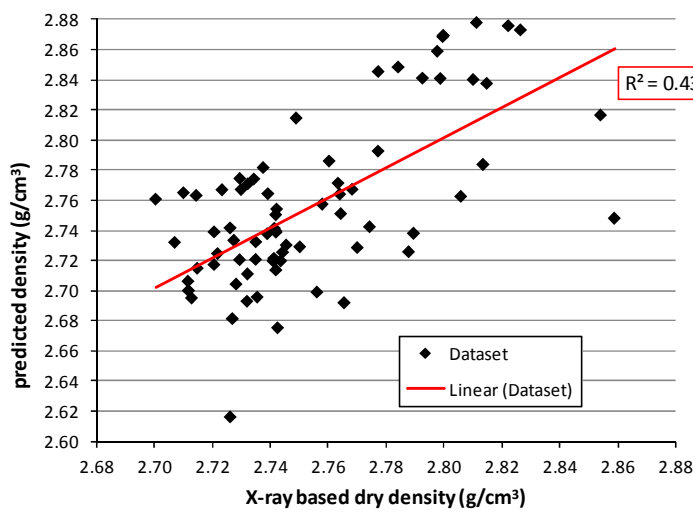


Fig. S17. Transfer function relationship for predicting the dry bulk density in Zwierzyniec-1. Where predicted density = $f_1 \cdot \text{SiO}_2 + f_2 \cdot \text{Al}_2\text{O}_3 + f_3 \cdot \text{CaO} + f_4 \cdot \text{MgO} + f_5 \cdot \text{Fe}_2\text{O}_3 + f_6 \cdot \text{K}_2\text{O} + C$, where $f_1 = 0.010561$, $f_2 = 0.072392$, $f_3 = 0.022630$, $f_4 = 0.000825$, $f_5 = 0.021847$, $f_6 = 0.163170$, $C = 1.520233$, oxides in weight%. The gradient was fixed to 1, and the coefficients are determined using excel solver, origin anchored to 2.7

g/cm^3 on both axes. ICP-OES data of Sullivan et al. (2018) used.

A. Age (σ_R) Ma	B. 'Chronostratigraphic' tie point etc	C. Depth range (m) of tie point	D. Uncertainty in placing position (Ma)	E. Depth (m)	F. \pm es (m)	G. P_{out}
427.18 (0.28)	Gorstian, <i>Bohemograptus bohemicus</i> and <i>Spinograptus spinosus (nilssoni)</i> Biozone	2825.0 - 2825.2	0.35	2825.1	2.22	0.016
429.42 (0.30)	<i>testis</i> subzone of <i>lundgreni</i> Biozone	2870	0.2	2870	8.35	0.006
429.60 (0.30)	<i>testis</i> subzone of <i>lundgreni</i> Biozone	2890.5	0.3	2890.5	13.44	0.011
430.35 (0.40)	<i>lundgreni</i> Biozone	2921.07 - 2872.9	0.15	2921.07	8.63	0.006
431.50 (0.40)	top ESCIE (base of Sh3 slice)	2924	0.15	2924	1.49	0.016
431.60 (0.40)	<i>Cy. rigidus</i> Biozone	2935.1 - 2925.3	0.5	2935.1	5.31	0.007
432.45 (0.44)	<i>M. riccartonensis</i> Biozone	2938.7	0.1	2938.7	1.62	0.005
432.51 (0.44)	<i>M. riccartonensis</i> Biozone	2941	0.1	2941	1.66	0.012
432.65 (0.44)	<i>murchisoni</i> up to this level	2941.49 - 0.92	0.1	2941.7	1.76	0.004
432.70 (0.44)	base ESCIE (top <i>Cy. murchisoni</i> to base <i>M. firmus</i> , Cramer et al. 2010)	2948	0.1	2948	1.79	0.009
432.90 (0.44)	<i>C. murchisoni</i> Biozone	2949.0 - 2950	0.15	2949.5	1.15	0.017
	Probable hiatus	2951.25				
434.85 (0.45)	lower <i>lapworthi</i> Biozone	2951.32 - 2951.48	0.25	2951.32	0.92	0.009
435.15 (0.46)	base Te4 correlated from Tluszcz	2952	0.1	2952	0.70	0.009
435.40 (0.46)	<i>St. vesiculosus</i> : upper <i>spiralis</i> Biozone	2952.95	0.15	2952.95	1.00	0.005

436.51 (0.45)	base Te3 correlated from Tluszcz	2957.7	0.15	2957.7	0.81	0.005
437.20 (0.45)	base Te2 correlated from Tluszcz	2967.8	0.15	2967.8	0.68	0.015
438.49 (0.45)	base Te1 correlated from Tluszcz	2968	0.15	2968	0.46	0.02
439.22 (0.45)	upper <i>leptotheca</i> or lower <i>convolutus</i> biozones	to 2968m	0.1	2968.5	0.05	0.012
439.30 (0.45)	<i>leptotheca</i> Biozone	2969 - 2969.35	0.1	2969.15	0.06	0.006
441.00 (0.50)	<i>Per. revolutus</i> Biozone	2970.31 -2970.42	0.15	2970.31	0.47	0.003
441.25 (0.50)	<i>Per. revolutus</i> Biozone	2971.63 -2971.73	0.15	2971.6	0.55	0.015
441.45 (0.50)	<i>Per. revolutus</i> Biozone	2974.5 - 2974.6	0.15	2974.5	0.62	0.007
442.10 (0.50)	<i>Cys. vesiculosus</i> Biozone	2978.88	0.2	2978.88	1.16	0.005
443.20 (0.55)	<i>N. trifilis</i> : mid <i>ascenus</i> - <i>acuminatus</i> Biozone	2981.97	0.2	2981.97	1.85	0.008
443.60 (0.70)	<i>Ak ascenus</i> Biozone	2984	0.15	2984	1.61	0.004
444.00 (0.75)	<i>Me. parvulus</i> : mid <i>Me persculptus</i> to mid <i>Ak. ascenus-acuminatus</i>	2985.2 -2985.24	0.2	2985.2	2.46	0.004
445.16 (0.75)	first rise in HICE, $\delta^{13}\text{C}$ (base or just below base <i>extraordinarius</i> Biozone)	3004	0.15	3004	2.61	0.007
444.30 (0.70)	<i>M. parvulus</i> : low in <i>Me. persculptus</i> Biozone	3013.97	0.25	3013.97	3.38	0.007
445.50 (0.60)	<i>Dicellograptus anceps</i> to <i>Normalograptus extraordinarius</i> zones	3018	0.3	3018	5.72	0.007

Table .S4. Data used to constrain the age model for Zwierzyniec-1, as generated from BChron. Columns:- A) Estimated age based on the CONOP based ages of biostratigraphic zones as listed in Table 20.1 of Cooper et al. (2012) and Table 21.1 of Melchin et al. (2012). σ_R = standard deviation in Ma from the same tables. B. The biostratigraphic or correlation tie point, from Sullivan et al. (2018) and this work. C. The depth range of the tie point in C. Column D. The estimated uncertainty (defined range in Ma) in the placing the tie point in B (from the core)

onto the dated biostratigraphic scales in Cooper et al. (2012) and Melchin et al. (2012). E. The depth used in the input to Bchron- this is mostly similar to C or if a range, the mid-point of the range. Column F. The estimated stratigraphic uncertainty used as ‘defined range’ uncertainty in BChron (see text). G. P_{out} , probability (0 to 1.0) the tie point may be an outlier (from Bchron processing); bigger values suggest this is more likely. All P_{out} , are very small indicating good consistency between the age tie points. The probable hiatus cannot be included into the BChron model, but is seen as a reduction in the accumulation rate.

6. Additional statistical details

	STI_R	$Al_2O_3^N$	Th	TiO_2^L	La	Ta	Zr	Hf	Ga	Nd	Ce	$Fe_2O_3^L$	Pr	Nb	Sc
χ_{cf}	0.66	0.64	0.60	0.59	0.58	0.58	0.57	0.57	0.56	0.56	0.55	0.55	0.55	0.54	0.53
As.1	$Al_2O_3^N$ (0.82)	Th (0.93)	Ta (0.96)	Sc (0.93)	Pr (0.97)	Th (0.96)	Hf (0.92)	Zr (0.92)	Th (0.91)	TiO_2^L (0.87)	Pr (0.97)	STI_R (0.66)	Nd (0.99)	TiO_2^L (0.87)	TiO_2^L (0.87)
As.2	Zr (0.77)	Ga (0.90)	$Al_2O_3^N$ (0.93)	Ta (0.91)	Nd (0.96)	TiO_2^L (0.91)	TiO_2^L (0.87)	Th (0.88)	$Al_2O_3^N$ (0.90)	Ta (0.86)	La (0.96)	Zr (0.60)	La (0.97)	Ta (0.86)	Ta (0.91)
As.3	TiO_2^L (0.76)	Ta (0.90)	Ta (0.91)	$Al_2O_3^N$ (0.89)	Ce (0.96)	Sc (0.91)	Th (0.81)	Ga (0.87)	La (0.90)	Sc (0.84)	Nd (0.96)	TiO_2^L (0.57)	Ce (0.97)	Sc (0.85)	$Al_2O_3^N$ (0.88)

Table S5. Selected Spearman correlation coefficients (R_s) for Silurian ICP OES-MS data from Zwierzyniec-1 (source data of Sullivan et al. 2018). Data excluded the faulted-interval, and included depths up to 2900 m in the core. All data, including elements were expressed as carbonate-free, to remove the carbonate dilution effect. Top row shows the 15 elements/indices with the largest R_s against carbonate free susceptibility. The lowest three rows (As.1 etc) are the three elements/indices with the largest R_s against the element/index in the top row (R_s value), indicating the key associations of this element or index. Included in the correlation matrix were $Al_2O_3^N$, Ba, Be, CIA, %calcite+dolomite, CaO^L , Ce, %TOC, Co, Cr, Cs, Cu, Dy, Er, Eu, $Fe_2O_3^L$, Ga, Gd, Hf, Ho, K_2O^N , La, Lu, MgO^L , MnO^L , Mo, Na_2O^L , Nb, Nd, Ni, $P_2O_5^L$, Pb, Pr, %quartz, Rb, S, Sc, SiO_2^L -Sm, Sn, Sr, STI_R , Ta, Tb, Th, TiO_2^L , Tl, Tm, U, V, W, WIP_R , Y, Yb, Zn and Zr.

Supplementary References

- Åhäll, K. I., Connelly, J. N., Brewer, T. S., 2002. Transitioning from Svecofennian to Transcandinavian Igneous Belt (TIB) magmatism in SE Sweden: implications from the 1.82 Ga Eksjö tonalite. *GFF* 124, 217-224.
- Algeo, T. J., Li, C., 2020. Redox classification and calibration of redox thresholds in sedimentary systems. *Geochimica et Cosmochimica Acta*. 287, 8-26.
- Baginski, B., Duchesne, J. C., Vander Auwera, J., Martin, H., Wiszniewska, J., 2001. Petrology and geochemistry of rapakivi-type granites from the crystalline basement of NE Poland. *Geological Quarterly* 45, 33-52.
- Batchelor, R. A., Clarkson, E. N. K., 1993. Geochemistry of a Silurian metabentonite and associated apatite from the North Esk Inlier, Pentland Hills. *Scottish Journal of Geology* 29, 123-130.
- Batchelor, R. A., Jeppsson, L. 1999. Wenlock metabentonites from Gotland, Sweden: geochemistry, sources and potential as chemostratigraphic markers. *Geological Magazine* 136, 661-669.
- Batchelor, R. A., Weir, J. A., Spieldnaes, N., 1995. Geochemistry of Telychian metabentonites from Vik, Ringerike District, Oslo Region. *Norsk Geologisk Tidsskrift*, 75, 219-228.
- Bau, M., Möller, P., Dulski, P., 1997. Yttrium and lanthanides in eastern Mediterranean seawater and their fractionation during redox-cycling. *Marine Chemistry* 56, 123-131.
- Bibikova, E. V., Claesson, S., Fedotova, A. A., Artemenko, G. V., Il'inskii, L., 2010. Terrigenous zircon of archean greenstone belts as a source of information on the early earth's crust: Azov and Dnieper domains, Ukrainian shield. *Geochemistry International* 48, 845-861.
- Bibikova, E. V., Fedotova, A. A., Claesson, S., Artemenko, G. V., Anosova, M. O., 2012. The early crust beneath the Azov Domain of the Ukrainian Shield: Isotopic-geochronological and geochemical investigations of detrital zircons from metasedimentary rocks of the Fedorovka structure. *Stratigraphy and Geological Correlation* 20, 125-138.
- Bibikova, E. V., Claesson, S., Fedotova, A. A., Stepanyuk, L. M., Shumlyansky, L. V., Kirnozova, T. I., Fugzan, M.M., Il'insky, L. S., 2013. Isotope-geochronological (U-Th-Pb, Lu-Hf) study of the zircons from the Archean magmatic and metasedimentary rocks of the Podolia domain, Ukrainian shield. *Geochemistry International* 51, 87-108.
- Bogdanova, S. V., Gintov, O. B., Kurlovich, D. M., Lubnina, N. V., Nilsson, M. K., Orlyuk, et al., 2013. Late Palaeoproterozoic mafic dyking in the Ukrainian Shield of Volgo-Sarmatia caused by rotation during the assembly of supercontinent Columbia (Nuna). *Lithos* 174, 196-216.
- Bojanowski, M. J., Kędzior, A., Porębski, S. J., Radzikowska, M., 2019. Origin and significance of early-diagenetic calcite concretions and barite from Silurian black shales in the East European Craton, Poland. *Acta Geologica Polonica* 403-430.
- Chen, J., Algeo, T. J., Zhao, L., Chen, Z. Q., Cao, L., Zhang, L., Li, Y., 2015. Diagenetic uptake of rare earth elements by bioapatite, with an example from Lower Triassic conodonts of South China. *Earth-Science Reviews* 149, 181-202.

- Condie, K. C., 1991. Another look at rare earth elements in shales. *Geochimica et Cosmochimica Acta* 55, 2527-2531.
- Condie, K. C., 2005. High field strength element ratios in Archean basalts: a window to evolving sources of mantle plumes? *Lithos* 79, 491-504.
- Cooper, R. A., Sadler, P. M., Hammer, O., Gradstein, F. M., 2012. The Ordovician Period. In Gradstein, F. M., Ogg, J. G., Schmitz, M. D., Ogg, G.M. (Eds.). *The Geologic Time Scale 2012*, Elsevier, Oxford, pp. 489-523.
- Cramer, B. D., Loydell, D. K., Samtleben, C., Munnecke, A., Kaljo, D., Männik, P. et al., 2010. Testing the limits of Paleozoic chronostratigraphic correlation via high-resolution (< 500 ky) integrated conodont, graptolite, and carbon isotope ($\delta^{13}\text{C}_{\text{carb}}$) biochemostratigraphy across the Llandovery–Wenlock (Silurian) boundary: Is a unified Phanerozoic time scale achievable? *Bulletin of the GSA* 122, 1700-1716.
- Doe, B. R., 1997. Geochemistry of Oceanic Igneous Rocks—Ridges, Islands, and Arcs—with Emphasis on Manganese, Scandium, and Vanadium. *International Geology Review* 39, 1053-1112.
- Dörr, W., Belka, Z., Marheine, D., Schastok, J., Valverde-Vaquero, P., Wiszniewska, J., 2002. U–Pb and Ar–Ar geochronology of anorogenic granite magmatism of the Mazury complex, NE Poland. *Precambrian Research* 119, 101-120.
- Dubyna, A. V., Kryvdik, S. G. & Sharygin, V. V., 2014. Geochemistry of alkali and nepheline syenites of the Ukrainian Shield: ICP-MS data. *Geochemistry International* 52, 842-856.
- Duchesne, J. C., Shumlyansky, L., Mytrokhyn, O. V., 2017. The jotunite of the Korosten AMCG complex (Ukrainian shield): Crust-or mantle-derived?. *Precambrian Research* 299, 58-74.
- Emsbo, P., McLaughlin, P. I., Breit, G. N., du Bray, E. A., Koenig, A. E., 2015. Rare earth elements in sedimentary phosphate deposits: solution to the global REE crisis? *Gondwana Research* 27, 776-785.
- Frost, B. R., Barnes, C. G., Collins, W. J., Arculus, R. J., Ellis, D. J., Frost, C. D., 2001. A geochemical classification for granitic rocks. *Journal of Petrology* 42, 2033-2048.
- Frost, B. R., Frost, C. D., 2008. A geochemical classification for feldspathic igneous rocks. *Journal of Petrology* 49, 1955-1969.
- Garcia, D., Fonteilles, M., Moutte, J., 1994. Sedimentary fractionations between Al, Ti, and Zr and the genesis of strongly peraluminous granites. *The Journal of Geology* 102, 411-422.
- Gorry, P.A., 1990. General least squares smoothing and differentiation by the Convolution (Savitsky-Golay) method. *Analytical Chemistry* 62, 570-573.
- Gurov, E. P., Koeberl, C., Reimold, W. U., 1998. Petrography and geochemistry of target rocks and impactites from the Ilyinets Crater, Ukraine. *Meteoritics & Planetary Science* 33, 1317-1333.
- Haley, B. A., Klinkhammer, G. P., McManus, J., 2004. Rare earth elements in pore waters of marine sediments. *Geochimica et Cosmochimica Acta* 68, 1265-1279.

- Haslett, J., Parnell, A., 2008. A simple monotone process with application to radiocarbon-dated depth chronologies. *Journal of the Royal Statistical Society: Series C (Applied Statistics)* 57, 399-418.
- Hill, I. G., Worden, R. H., Meighan, I. G., 2000. Yttrium: the immobility-mobility transition during basaltic weathering. *Geology* 28, 923-926.
- Krzemińska, E., Williams, I., Wiszniewska, J., 2005. A Late Paleoproterozoic (1.80 Ga) subduction-related mafic igneous suite from Lomza, NE Poland. *Terra Nova* 17, 442-449.
- Liivamägi, S., Šrodoň, J., Bojanowski, M. J., Gerdes, A., Stanek, J. J., Williams, L., Szczerba, M., 2018. Paleosols on the Ediacaran basalts of the East European Craton: A unique record of paleoweathering with minimum diagenetic overprint. *Precambrian Research* 316, 66-82.
- Ling, H. F., Chen, X., Li, D. A., Wang, D., Shields-Zhou, G. A., Zhu, M., 2013. Cerium anomaly variations in Ediacaran–earliest Cambrian carbonates from the Yangtze Gorges area, South China: implications for oxygenation of coeval shallow seawater. *Precambrian Research*, 225, 110-127.
- Loader, C., 1999 *Local regression and likelihood*. Springer, Berlin.
- Lobach-Zhuchenko, S. B., Balagansky, V. V., Baltybaev, S. K., Bibikova, E. V., Chekulaev, V. P., Yurchenko, A. V., et al., 2014a. The Orekhov–Pavlograd Zone, Ukrainian Shield: Milestones of its evolutionary history and constraints for tectonic models. *Precambrian Research* 252, 71-87.
- Lobach-Zhuchenko, S. B., Balagansky, V. V., Baltybaev, S. K., Artemenko, G. V., Bogomolov, E. S., Yurchenko, A. V. et al., 2014b. Metasedimentary rocks of the Paleoproterozoic Dniester-Bug Group, Ukrainian Shield: Composition, age, and sources. *Lithology and Mineral Resources* 49, 381-397.
- Lobach-Zhuchenko, S. B., Kaulina, T. V., Baltybaev, S. K., Balagansky, V. V., Egorova, Y. S., Lokhov, K. I., et al., 2017. The long (3.7–2.1 Ga) and multistage evolution of the Bug Granulite–Gneiss Complex, Ukrainian Shield, based on the SIMS U–Pb ages and geochemistry of zircons from a single sample. In: Halla, J., Whitehouse, M. J., Ahmad, T. & Bagai, Z. (eds) *Crust–Mantle Interactions and Granitoid. Diversification: Insights from Archaean Cratons*. Geological Society, London, Special Publications, 449, 175–206.
- Mansfeld, J., 1996. Geological, geochemical and geochronological evidence for a new Palaeoproterozoic terrane in southeastern Sweden. *Precambrian Research* 77, 91-103.
- McLennan, S. M., 2001. Relationships between the trace element composition of sedimentary rocks and upper continental crust. *Geochemistry, Geophysics, Geosystems*, 2, 2000GC000109.
- Melchin, M. J., Sadler, P. M., Cramer, B. D., Cooper, R. A., Gradstein, F. M., Hammer, O., 2012. The Silurian Period. In: Gradstein, F. M., Ogg, J. G., Schmitz, M. D., Ogg, G.M. (Eds.). *The Geologic Time Scale 2012*, Elsevier, Oxford, pp. 525-558.
- Meschede, M., 1986. A method of discriminating between different types of mid-ocean ridge basalts and continental tholeiites with the Nb-Zr-Y diagram. *Chemical Geology* 56, 207-218.

- Ortiz, E., Roser, B. P., 2006. Major and trace element provenance signatures in stream sediments from the Kando River, San'in district, southwest Japan. *Island Arc* 15, 223-238.
- Parnell, A. C., Haslett, J., Allen, J. R., Buck, C. E., Huntley, B., 2008. A flexible approach to assessing synchronicity of past events using Bayesian reconstructions of sedimentation history. *Quaternary Science Reviews* 27, 1872-1885.
- Pearce, J. A., Norry, M. J., 1979. Petrogenetic implications of Ti, Zr, Y, and Nb variations in volcanic rocks. *Contributions to Mineralogy and Petrology* 69, 33-47.
- Pearce, J. A., Harris, N. B., Tindle, A. G., 1984. Trace element discrimination diagrams for the tectonic interpretation of granitic rocks. *Journal of Petrology* 25, 956-983.
- Ray, D. C., 2007. The correlation of Lower Wenlock Series (Silurian) bentonites from the Lower Hill Farm and Eastnor Park boreholes, Midland Platform, England. *Proceedings of the Geologists' Association* 118, 175-185
- Ray, D. C., Collings, A. V., Worton, G. J., Jones, G., 2011. Upper Wenlock bentonites from Wren's Nest Hill, Dudley: comparisons with prominent bentonites along Wenlock Edge, Shropshire, England. *Geological Magazine* 148, 670-681.
- Ray, D. C., Richards, T. D., Brett, C. E., Morton, A., Brown, A. M., 2013. Late Wenlock sequence and bentonite stratigraphy in the Malvern, Suckley and Abberley Hills, England. *Palaeogeography, Palaeoclimatology, Palaeoecology* 389, 115-127.
- Rosen, O. M., Abbyasov, A. A., Tipper, J. C., 2004. MINLITH—an experience-based algorithm for estimating the likely mineralogical compositions of sedimentary rocks from bulk chemical analyses. *Computers & Geosciences* 30, 647-661.
- Rudnick, R. L., Gao, S., 2003. Composition of the continental crust. *Treatise on Geochemistry* 2nd Edition. In: Holland, H.D & Turekian, K.K. *The Crust*, Vol. 4, Elsevier.
- Savko, K. A., Samsonov, A. V., Kholina, N. V., Larionov, A. N., Zaitseva, M. V., Korish, E. H., Bazikov, N.S., Terentiev, R. A., 2019. 2.6 Ga high-Si rhyolites and granites in the Kursk Domain, Eastern Sarmatia: Petrology and application for the Archaean palaeocontinental correlations. *Precambrian Research* 322, 170-192.
- Schoepfer, S.D., Algeo, T.J., Ward, P.D., Williford, K.H., Haggart, J.W. 2016. Testing the limits in a greenhouse ocean: Did low nitrogen availability limit marine productivity during the end-Triassic mass extinction? *Earth and Planetary Science Letters* 451, 138–148.
- Shields, G., Stille, P., 2001. Diagenetic constraints on the use of cerium anomalies as palaeoseawater redox proxies: an isotopic and REE study of Cambrian phosphorites. *Chemical Geology* 175, 29-48.
- Shields, G., Webb, G., 2004. Has the REE composition of seawater changed over geological time?. *Chemical Geology* 204, 103-107.
- Shnyukov, S., Lazareva, I., Zinchenko, O., Khlon, E., Gavryliv, L., Aleksieienko, A., 2018. Geochemical model of Precambrian granitoid magmatic evolution in the Korosten pluton (Ukrainian Shield): petrogenetic aspects and genesis of complex ore mineralization in

- metasomatic zones. *Visnyk of Taras Shevchenko, National University of Kyiv: Geology*, 2, 12-22.
- Shumlyanskyy, L. V., 2014. Geochemistry of the Osnitsk-Mikashevichy volcanoplutonic complex of the Ukrainian shield. *Geochemistry International* 52, 912-924.
- Shumlyanskyy, L., Mitrokhin, O., Billström, K., Ernst, R., Vishnevskaya, E., Tsymbal, S., Cuney, M., Soesoo, A., 2016. The ca. 1.8 Ga mantle plume related magmatism of the central part of the Ukrainian shield. *GFF* 138, 86-101.
- Skridlaitė, G., Wiszniewska, J., Duchesne, J. C., 2003. Ferro-potassic A-type granites and related rocks in NE Poland and S Lithuania: west of the East European Craton. *Precambrian Research* 124, 305-326.
- Skridlaitė, G., Whitehouse, M., Rimša, A., 2007. Evidence for a pulse of 1.45 Ga anorthosite–mangerite–charnockite–granite (AMCG) plutonism in Lithuania: implications for the Mesoproterozoic evolution of the East European Craton. *Terra Nova* 19, 294-301.
- Skridlaitė, G., Baginski, B., Whitehouse, M., 2008. Significance of ~ 1.5 Ga zircon and monazite ages from charnockites in southern Lithuania and NE Poland. *Gondwana Research* 14, 663-674.
- Snow, C. A., 2006. A re-evaluation of tectonic discrimination diagrams and a new probabilistic approach using large geochemical databases: Moving beyond binary and ternary plots. *Journal of Geophysical Research: Solid Earth*, 111. doi.org/10.1029/2005JB003799.
- Soesoo, A., Košler, J., Kuldkepp, R., 2006. Age and geochemical constraints for partial melting of granulites in Estonia. *Mineralogy and Petrology* 86, 277-300.
- Sundblad, K., Mansfeld, J., Motuza, G., Ahl, M., Claesson, S., 1994. Geology, geochemistry and age of a Cu-Mo-bearing granite at Kabeliai, Southern Lithuania. *Mineralogy and Petrology* 50, 43-57.
- Sullivan, N. B., Loydell, D. K., Montgomery, P., Molyneux, S. G., Zalasiewicz, J., Ratcliffe, K. T., Campbell, E., Griffiths, J.D., Lewis, G., 2018. A record of Late Ordovician to Silurian oceanographic events on the margin of Baltica based on new carbon isotope data, elemental geochemistry, and biostratigraphy from two boreholes in central Poland. *Palaeogeography, Palaeoclimatology, Palaeoecology* 490, 95-106.
- Terentiev, R. A., Santosh, M., 2016. Detrital zircon geochronology and geochemistry of metasediments from the Vorontsovka terrane: implications for microcontinent tectonics. *International Geology Review* 58, 1108-1126.
- Terentiev, R. A., Savko, K. A., 2016. Paleoproterozoic high-Mg low-Ti gabbro-granite series in Eastern Sarmatia: geochemistry and formation conditions. *Russian Geology and Geophysics* 57, 907-932.
- Terentiev, R. A., Skryabin, V. Y., Santosh, M., 2016a. U–Pb zircon geochronology and geochemistry of Paleoproterozoic magmatic suite from East Sarmatian Orogen: tectonic implications on Columbia supercontinent. *Precambrian Research* 273, 165-184.

- Terentiev, R. A., Savko, K. A., Santosh, M., 2016b. Paleoproterozoic crustal evolution in the East Sarmatian Orogen: Petrology, geochemistry, Sr–Nd isotopes and zircon U–Pb geochronology of andesites from the Voronezh massif, Western Russia. *Lithos* 246, 61-80.
- Terentiev, R. A., Savko, K. A., Santosh, M., 2017. Paleoproterozoic evolution of the arc–back-arc system in the East Sarmatian Orogen (East European Craton): zircon SHRIMP geochronology and geochemistry of the Losevo volcanic suite. *American Journal of Science* 317, 707-753.
- Terentiev, R. A., Savko, K. A., Santosh, M., 2018. Post-collisional two-stage magmatism in the East Sarmatian Orogen, East European Craton: evidence from the Olkhovsky ring complex. *Journal of the Geological Society* 175, 86-99.
- Terentiev, R. A., Savko, K. A., Petrakova, M. E., Santosh, M., Korish, E. H., 2020. Paleoproterozoic granitoids of the Don terrane, East-Sarmatian Orogen: age, magma source and tectonic implications. *Precambrian Research* 345, doi.org/10.1016/j.precamres.2020.105790
- Tostevin, R., Shields, G. A., Tarbuck, G. M., He, T., Clarkson, M. O., Wood, R. A., 2016. Effective use of cerium anomalies as a redox proxy in carbonate-dominated marine settings. *Chemical Geology*, 438, 146-162.
- Tribouillard, N., Algeo, T. J., Lyons, T., Riboulleau, A., 2006. Trace metals as paleoredox and paleoproductivity proxies: an update. *Chemical Geology*, 232, 12-32.
- Winchester, J. A., Floyd, P. A., 1977. Geochemical discrimination of different magma series and their differentiation products using immobile elements. *Chemical Geology* 20, 325-343.
- Williams, I. S., Krzemińska, E., Wiszniewska, J., 2009. An extension of the Svecofennian orogenic province into NE Poland: evidence from geochemistry and detrital zircon from Paleoproterozoic paragneisses. *Precambrian Research* 172, 234-254.
- Wiszniewska, J., Claesson, S., Stein, H., Auwera, J. V., Duchesne, J. C., 2002. The north-eastern Polish anorthosite massifs: petrological, geochemical and isotopic evidence for a crustal derivation. *Terra Nova* 14, 451-460.
- Wiszniewska, J., Krzeminska, E., Dörr, W., 2007. Evidence of arc-related Svecofennian magmatic activity in the southwestern margin of the East European Craton in Poland. *Gondwana Research* 12, 268-278.
- Yang, J., Torres, M., McManus, J., Algeo, T. J., Hakala, J. A., Verba, C., 2017. Controls on rare earth element distributions in ancient organic-rich sedimentary sequences: Role of post-depositional diagenesis of phosphorus phases. *Chemical Geology* 466, 533-544.
- Yang, X. M., 2007. Using the Rittmann Serial Index to define the alkalinity of igneous rocks. *Neues Jahrbuch für Mineralogie-Abhandlungen: Journal of Mineralogy and Geochemistry* 184, 95-103.
- Zhang, L., Algeo, T.J., Cao, L., Zhao, L., Chen, Z-Q., Li Z. 2016. Diagenetic uptake of rare earth elements by conodont apatite. *Palaeogeography, Palaeoclimatology, Palaeoecology* 458, 176–197.